ABSTRACT

SPRINGER, JESSICA COLLINS. *In vitro* Studies of Titanium Alloy Discs Fabricated with Electron Beam Melting for Improving Transdermal Osseointegrated Implant Surfaces. (Under the direction of Dr. Ola Harrysson and Dr. Denis Marcellin-Little).

Custom (patient-specific) transdermal osseointegrated implants generated using direct metal fabrication methods, such as electron beam melting (EBM) may be considered as alternatives to socket prostheses due to the more natural transfer of loads. EBM may be used to make metal implants that usually have polished solid surfaces and unpolished porous surfaces. The resistance to bacterial infection is critically important to the overall success of the procedure and may be improved with skin ingrowth at the skin-implant interface. Human adipose-derived adult stem cells (hASCs), normal human epidermal keratinocytes (NHEK), and neonatal normal human dermal fibroblasts (NHDF-Neo) attach and proliferate when in contact with titanium, but that bond is likely influenced by the surface characteristics of the titanium implants. The *in vitro* biocompatibility of EBM Ti6Al4V structures were assessed by comparing the response of several types of cells to Ti6Al4V discs; solid polished EBM, solid unpolished EBM, porous EBM, and commercially produced. Chemical etching with a hydrofluoric-nitric acid solution was also used as a method for reducing the surface roughness of EBM porous surfaces and the biocompatibility of these surfaces compared with NHDF-Neo and NHEK cells. A transdermal osseointegrated implantable device was designed to enable future *in vivo* research of these surfaces.

EBM and commercially produced Ti6Al4V discs were seeded with hASCs and assessed for cell proliferation, viability, and release of the proinflammatory cytokines interleukin-6 (IL-6) and interleukin-8 (IL-8). Cell proliferation was assessed using alamarBlue® assays at days 0, 1, 2, 3, and 7. Cell viability was assessed with LIVE/DEAD® staining on day 8. Additional discs were seeded with NHDF-Neo or NHEK cells and assessed for cell proliferation at days 2 and 7 using alamarBlue®

assays. Cell viability was analyzed with fluorescence-based LIVE/DEAD® assays at days 7 and 8 for the NHDF-Neo and NHEK, respectively. Porous etched and non-etched discs were seeded with NHDF-Neo or NHEK cells and cell proliferation, viability, and morphology were assessed. Cell proliferation was assessed on days 0, 2, and 7 using alamarBlue® assays. Cell viability was assessed on day 9 using LIVE/DEAD assays. Cell morphology was assessed with scanning electron microscopy (SEM) on day 8.

The hASCs were alive on all discs after 8 days. Cellular proliferation on porous EBM discs was increased when compared to discs made of commercial Ti6Al4V, solid polished, and unpolished EBM discs. IL-6 and IL-8 releases at day 7 were lower for porous EBM discs than for other discs. Solid polished, unpolished, and porous EBM Ti6Al4V discs exhibited an acceptable biocompatibility profile compared to solid Ti6Al4V discs from a commercial source. For both NHDF-Neo and NHEK cells, day 7 proliferation levels were higher for scaffolds with lower surface roughness values. No statistical difference was present between commercial and EBM-fabricated titanium seeded with NHDF-Neo cells. NHDF-Neo cellular proliferation on etched EBM discs was increased compared to non-etched discs. There was no difference in NHEK cellular proliferation between etched and non-etched EBM discs.

EBM is a valid option for the fabrication of custom orthopedic implants.   For transdermal osseointegrated implants, the EBM etched surfaces appear to be an acceptable skin-implant interface option. The EBM as-processed surface may be successful for promoting bone ingrowth. To analyze these results *in vivo,* the transdermal osseointegrated implantable device can be fabricated with EBM and surgically implanted. The ability to efficiently create a porous ingrowth surface on custom implants is possible with EBM and these custom implants may restore mobility to many patients with amputated limbs.

In vitro Studies of Titanium Alloy Discs Fabricated with Electron Beam Melting
for Improving Transdermal Osseointegrated Implant Surfaces

by
Jessica Collins Springer

A dissertation submitted to the Graduate Faculty of
North Carolina State University
in partial fulfillment of the
requirements for the Degree of
Doctor of Philosophy

Industrial Engineering

Raleigh, North Carolina

2010

APPROVED BY:

_____ _____
Dr. Ola Harrysson   Dr. Denis Marcellin-Little
Chair of Advisory Committee   Co-Chair of Advisory Committee

_____ _____
Dr. Harvey West, II   Dr. Denis Cormier

_____
Dr. Elizabeth Loboa

DEDICATION

I dedicate this work to my family; the people that have always believed in me and encouraged me. To my parents who supported and loved me so greatly, thank you. To my sister who is a natural teacher and taught me algebra when I was in elementary school, thank you. To my husband who supports me and loves me everyday, thank you. And to my daughter, who unknowingly encourages me with her loving smile, thank you.

I also want to dedicate this work to the professors that have supported me through my degree; the first, second, and now for the third time. Thank you for your support and guidance.

BIOGRAPHY

Jessica grew up in North Carolina with her wonderful parents and sister. She made a short trek across the state to Raleigh to attend NC State for her undergraduate degree in Industrial Engineering where she was fortunate enough to meet the love of her life. She continued on for her Masters in Industrial Engineering at NC State and then took a full-time job. After working in industry for a few years, she decided to return to NC State to pursue her PhD in Industrial and Systems Engineering. During that pursuit she became a mother to the sweetest and most adorable little girl.

ACKNOWLEDGMENTS

TABLE OF CONTENTS

.

LIST OF TABLES

LIST OF FIGURES

1.0 INTRODUCTION

In 2005, nearly 1.6 million people in the United States had undergone limb removal (Ziegler-Graham et al., 2008). The removal of an arm or a leg, whether surgical or trauma induced, is referred to as an amputation. There has been a steady increase in diagnosis of diabetes and amputations that result from arterial disease due to diabetes represent more than half of all amputations within the United States. Researchers in Québec, Canada conducted a survey to evaluate prosthetic use and found that about 80% of the lower-extremity amputations resulted from vascular disease and diabetes (Gauthier-fiagnon et al., 1998). There are also a large number of military personnel returning from deployment with an injury to one or both lower limbs. Vehicular accidents, sports-related injuries, cancer-related amputations, and congenital defects are additional contributors to the increasing population of patients without two complete and functional lower limbs. In conjunction with the ever-increasing fast pace of societies, there is a growing need to restore mobility to these patients.

Some amputees are fitted with a prosthesis, a mechanical device that restores a degree of functionality of the missing limb and helps patients lead normal, active lives. Although, rudimentary forms of prosthetic devices can be traced back to ancient times, the nineteenth century brought about many changes and improvements and artificial legs with more functionality. Material developments during the twentieth century, such as modern plastics and carbon fiber composites, led to even greater prosthetic devices provided functionality without the weight of earlier materials. While socket prostheses restore mobility to many patients, they require frequent refitting and/or

replacement and can cause skin irritations and infections. Some of these problems lead to disuse of the prosthesis (Meulenbelt et al., 2006). Unnatural stresses and forces from wearing lower limb socket prosthesis can lead to skin problems such as stump edema, blisters, lichenification, verruciform hyperkeratosis, epidermoid cysts, acro-angiodermatitis, and skin carcinoma. Infections of the skin can result from the increased perspiration caused by the close fit and warmth of the socket and the lack of proper ventilation. Additionally, bacterial infections, ulcerations, allergic reactions to the plastic from the socket interface with the skin, and worsening of existing skin disorders can all result from wearing socket prostheses. The above mentioned skin problems are not only uncomfortable and potentially detrimental to the patient's health, but can also impede daily prosthetic use and reduce mobility of the amputee. These skin problems often require the discontinued use of the prosthetic until healing has occurred. The socket of the prosthesis can also become loose as the plastic liner becomes stretched through movement of the stump.   The stump size may also increase and decrease with body temperature changes. This loosening of the prosthesis socket can cause altered pressure locations than initially intended and can lead to localized pain. This loosening of the prosthesis also requires that the patient is refitted for a socket periodically. Gauthier-fiagnon et al. found that although many improvements to prosthetic devices have been developed, nearly 46% of the people with lower-extremity amputations require a prosthetic refitting every year (1998).

Since most issues associated with socket prostheses are related to the attachment points on the epidermis, research is being done to eliminate these issues by attaching the prosthetic directly to the bone. Approximately 100 years after the first socket prosthesis was created, Per-Ingvar Brånemark discovered the concept of osseointegration; the direct anchorage of an implant to the

bone, when he found that a titanium chamber inserted into the bone of a rabbit had become part of the bone at the conclusion of his experiment. The key to practical use of osseointegrated prostheses is that the prostheses acts as a natural part of the body, meaning that there is no relative motion between the prosthesis and the host bone. This connection should also be able to remain rigid and intact under normal loading, such as walking and running, for lower limb prostheses. Direct anchorage to the bone allows the forces to transmit more naturally via the bone instead of the soft tissue, which helps to eliminate problems like chaffing, sores, and irritations. While the Brånemarks and their collaborators have created osseointegrated implants, their design lacks customization and does not contain an ingrowth surface. Porous-coated implants, including hip and knee implants, have been proven to provide greater surface area for ingrowth and lead to improved stability (Engh et al., 1987). This porous layer promoted osseointegration and improved stability for weight-bearing joints without using cement which has proven to have many disadvantages.

The osseointegrated screw-shaped device that Brånemark and his collaborators have developed lacks a soft tissue ingrowth surface. Their initial osseointegrated implants were dental implants, but since then they have developed orthopedic implants as well (Brånemark et al., 1977). Attachment at the skin/implant surface has been shown to be an important barrier to infection at the implantation site and as Tillander et al. reports, most metal transcutaneous implants have failed due to infection (2010). Vast amounts of research has been completed to understand the most appropriate surface and pore size to induce cell growth, but can vary with the types of cells. Additionally, various surface modifications, both coatings and etchings, have been analyzed to determine whether they promote or hinder cell viability and proliferation. Osseointegration, and

therefore implant fixation, has been proven to improve with some surface modifications and porous surfaces. As new metals are discovered to be biocompatible they are also tested to understand if they are superior to the biometals currently used for implants. The biological environment is a very harsh environment for an implant to reside in permanently and a superior biocompatible metal is critical to advances in permanent, orthopedic implant success. Recent advances in medical imaging and additive manufacturing methods have also helped to improve the ability to design and build custom implants directly from biocompatible metal powder.

To create a structurally stable implant that is affixed to the bone, an optimal implant surface must be developed. Electron beam melting (EBM) is an additive manufacturing method that allows direct fabrication of custom designed implants from biocompatible metal powders. This research analyzes porous and solid surfaces fabricated with EBM with various textures; as-processed, polished, and etched Titanium alloy (Ti6Al4V) to determine the best surface for cell viability and proliferation. While EBM has been used to fabricate many structures, the research of testing the cellular response of implants built by this method has not been completed thus far. *In vitro* analysis is the first step to ensure that this material is able to host cells and promote ingrowth of bone and soft tissues. Additionally, initial testing helps to determine if the porous design can withstand forces that will be present upon implantation of the *in vivo* device in future research.

From the research of osseointegration, emerged the related area of osseoperception, which is the awareness that an amputee with an osseointegrated prosthesis experiences when stimuli is applied to the prosthesis. This research was initially related to the dental osseointegrated prostheses; however, there has also been an orthopedic study to understand the extent of this

awareness of stimuli (Brånemark et al., 2001). The study consisted of two groups of patients with the first group having a patient from the same gender, age range, and type of amputation as the second group for comparison. The first group of patients had osseointegrated prostheses while the second group was made up of patients fitted with conventional socket prostheses. The vibratory stimulus was applied to both the healthy limb and the amputated limb. The results showed that the group with osseointegrated prostheses was able to perceive the stimuli much better than the conventional socket prosthesis, due to the direct attachment to the bone. This finding may be helpful in restoring an amputee's lifestyle back to a more normal way of life. With an enhanced ability to sense the surroundings it could make it easier to perform natural movements, such as walking and running.

2.0 STEM CELL RESPONSE TO EBM TITANIUM

The research in this chapter has been previously published by the authors listed below in the following article and journal.

In vitro biocompatibility of titanium alloy discs made using direct metal fabrication

Carla Maria Haslauer[a,1], Jessica Collins Springer[b,1], Ola L.A. Harrysson[a,b], Elizabeth G. Loboa[a], Nancy A. Monteiro-Riviere[a,c,d], Denis J. Marcellin-Little [a,d,*]

[a] Joint Department of Biomedical Engineering, University of North Carolina at Chapel Hill and North Carolina State University, Raleigh, NC 27695, USA
[b] Fitts Department of Industrial and Systems Engineering, North Carolina State University, Raleigh, NC 27695, USA
[c] Center for Chemical Toxicology Research and Pharmacokinetics, North Carolina State University, Raleigh, NC 27606, USA
[d] Department of Clinical Sciences, College of Veterinary Medicine, North Carolina State University, Raleigh, NC 27606, USA

2.1 Introduction

For more than four decades knee and hip replacements have been performed and other joints, such as shoulders and elbows have also had similar procedures performed. In the U.S. alone, over 200,000 primary total hip arthroplasties and over 400,000 primary total knee arthroplasties were performed in 2003 (Kurtz et al., 2007). Due to the load at the hip, the body's largest weight-bearing joint, it is critical that there is a proper connection between the implant and the bone. Fixation at the bone-implant interface can either occur through bone ingrowth into a porous-coated surface, growth onto a solid surface, or with the addition of bone cement or polymethyl-methacrylate (PMMA).   Many factors can influence osseointegration including implant characteristics, mechanical loading, and bone quality (Albrektsson et al., 1983; Puleo et al., 1999; Sumner et al., 2001). Osseointegration also requires close proximity between the bone and implant (Asaoka et al., 1985; Simmons et al., 1999; Thomas et al., 1987). The interfacial motion between implant and bone should be less than 150 μm to allow bone ingrowth. Motion greater than 150 μm has been shown to lead to fibrous tissue ingrowth (Szmukler-Moncler et al., 1988). Fibrous ingrowth impedes future bone ingrowth and causes inefficient stress transfer from implant to bone, typically resulting in implant failure (Albrektsson et al., 1983; El-Warrak et al., 2004; Thelen et al., 2004). Custom-designed, patient-specific implants have the potential to reduce micromotion and maintain bone integrity.

The fabrication of custom implants using conventional methods (machining, casting) is very challenging given the complex geometry of bone. Further, it is technically difficult to prepare implants having both solid and porous portions (Sotereanos et al., 2006). To avoid the challenge of

creating patient-specific implants with porous ingrowth surfaces, custom implants may be fixed using acrylic bone cement (Lewis, 1997; Saha et al., 1984). The use of bone cement, however, has been associated with soft tissue injury from monomer leakage, infection, bone resorption, and aseptic loosening. These negative side effects have led to the increased use of cementless implants with a porous surface to promote bone ingrowth. Cementless hip implants are primarily used for relatively young and active patients with good bone quality (Chiba et al., 1994). As the surface of the implant becomes encompassed by bone growth the implant becomes stronger, critical for withstanding the loads on the hip implant and other weight-bearing implants. Engh et al. implanted porous-coated cobalt-chromium femoral implants and from eleven implants that were removed, nine showed bone ingrowth and two had fibrous tissue fixation (1987). The results of their study indicate that implants with porous surfaces are more successful when a press fit is achieved. In order to better understand the osseointegration of knee arthroplasty components, Bellemans conducted *in vivo* research with sheep (1999). The research showed that fibrous tissue ingrowth on porous-coated knee implants can function as well as osseointegrated implants during the early years of implantation, but long-term mechanical stability and fixation is much stronger for osseointegrated implants. These results are consistent with other research that found that fibrous tissue formation may lead to loosening of the implant after long-term implantation (Bellemans, 1999).

Many studies have been performed to investigate the migration and proliferation of cells in contact with various surfaces to better understand the ability for bone to attach to implant surfaces. Cellular response to polished and abraded surfaces, beaded surfaces, and coatings have all been

investigated and compared. Most studies have similarly concluded that the rough surfaces and porous surfaces enhance osseointegration. Porous metals can be classified into two categories, open-cell and closed-cell and can be manufactured by numerous methods, such as additive manufacturing (Ryan et al., 2006). Closed-cell foams are identified with a thin wall of metal surrounding the pores, whereas the open-cell structures have interconnected pores. A majority of the industrial engineering applications of porous structures are fabricated with closed-cell techniques in order to reduce impurities and therefore improve the mechanical properties. However, functional porous structures, for example those that facilitate bone ingrowth require open-cell structures where osteoblasts and mesenchymal cells are able to migrate into the voids and anchor to the structure. Kuboki et al. conducted a study that showed the interconnected porous structure allowed vasculature that lead to osteogenesis while there was no bone formation on the smooth structures (1998).

Direct metal fabrication (DMF) allows the creation of custom titanium implants designed from a patient's computed tomography (CT) scans (Cormier et al., 2004). Implants can be designed to fit a patient's bone using computer aided design (CAD) software and fabricated directly from the CAD files by selectively melting thin layers of Ti6Al4V powder placed successively on a build platform (Gaytan et al., 2009; Li et al., 2009; Murr et al., 2009). DMF methods include laser engineering net shaping (LENS), selective laser sintering, and electron beam melting (EBM), (Balla et al., 2009). While the biocompatibility of implants made using LENS has been reported (Bandyopadhyay et al., 2009; Vamsi et al., 2008; Xue et al., 2007), little is known about the biocompatibility of EBM Ti6Al4V implants. The bone healing response to machined bulk and rough solid EBM Ti6Al4V implants was

recently evaluated in rabbits (Thomsen et al., 2009).

The purpose of the research presented here was to assess the *in vitro* response of human cells to solid and porous EBM Ti6Al4V structures and to compare it to commercial Ti6Al4V structures. It was hypothesized that unpolished solid, polished solid, and porous EBM Ti6Al4V structures would be as biocompatible as commercial polished Ti6Al4V structures, that the increased surface area of unpolished and porous EBM structures would enhance cellular proliferation without increasing the release of the pro-inflammatory cytokines interleukin 6 (IL-6) and 8 (IL-8). To test this hypothesis, the cell viability and proliferation and the release of IL-6 and IL-8 was assessed after exposing human adipose-derived adult stem cells (hASC) to a range of Ti6Al4V discs.

2.2 Materials and Methods

2.2.1 Disc Preparation

Four groups of three Ti6Al4V discs (10 mm diameter and 6 mm height) were produced and used in all analyses: (A) polished solid discs from a commercial source (grade 5 titanium, McMaster-Carr Supply Company, Santa Fe Springs, CA) used as controls, (B) polished solid EBM discs, (C) unpolished solid EBM discs, and (D) unpolished, porous EBM discs with 76% porosity (Figure 1). The porous EBM discs had an open mesh structure with hexagonal unit cells with a final fabricated diameter of 650 μm (Figure 2).

The commercial and polished solid EBM discs were machined on a computer numerically-controlled (CNC) lathe (Hawk 150, MAG Cincinnati, Hebron, KY). The polished discs were abraded

with silicon carbide paper in successive grades from 240 to 2000 grit and subsequently polished with a slurry containing 6µm diamond, 1µm Al_2O_3, and 0.3µm Al_2O_3 powder (Mark V Laboratory, East Granby, CT). The unpolished and porous discs were blasted with titanium powder to remove any loose or lightly sintered powder. The surface roughness of the discs was measured by taking four surface roughness measurements from two randomly chosen discs within each group. The rough and porous discs were evaluated with a Hirox KH-7700 microscope (Hirox-USA, Inc., River Edge, NJ) and the solid discs were evaluated with a surface profilometer (Mitutoyo Surftest 212, Mitutoyo U.S.A., Aurora, IL). To assess the rough surfaces, three dimensional (3D) renderings of the surfaces were created, a measurement plane was placed perpendicular to the surface, and surface roughness was measured along that plane (Figure 3). The surface roughness of porous EBM discs was measured along the strut surface. The disc surfaces (Figure 4) were assessed using a scanning electron microscope (JSM-6400D, JEOL USA, Peabody, MA).

The discs were ultrasonically cleaned with isopropyl alcohol for ten minutes, rinsed with distilled water for ten minutes, treated with an enzymatic foam spray (Prepzyme® X.F. eXtreme Foam, Ruhof Corporation, Mineola, NY), ultrasonically washed, rinsed with distilled water, dried with pressurized air, and steam sterilized in sealed pouches.
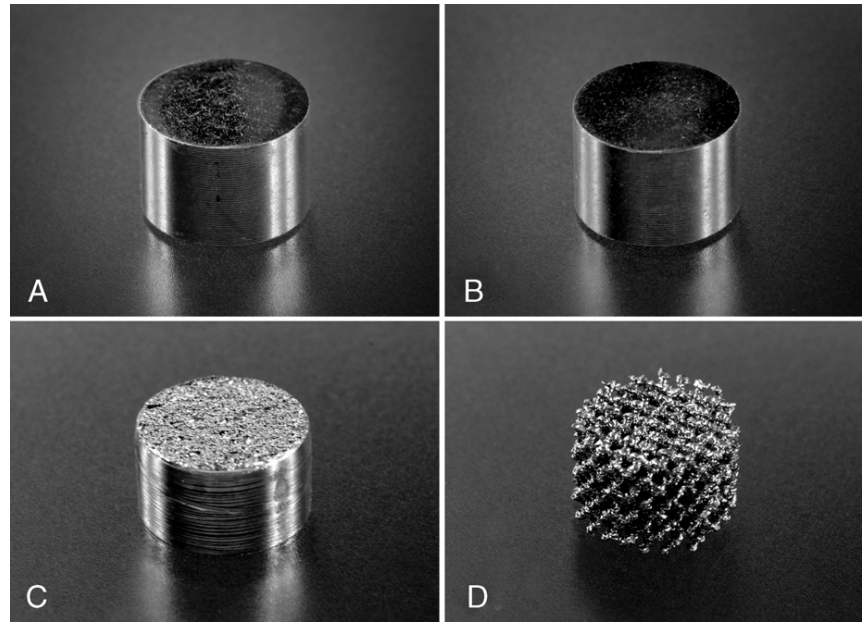
Figure 1: Photographs of the Ti6Al4V discs used in this study. They include a) solid polished discs from a commercial source used as a control, b) solid polished discs fabricated with EBM additive manufacturing, c) solid unpolished EBM discs, and d) porous EBM discs, with 76% porosity and approximately 650μm pores. The discs measure 10 mm in diameter and 6 mm in height.
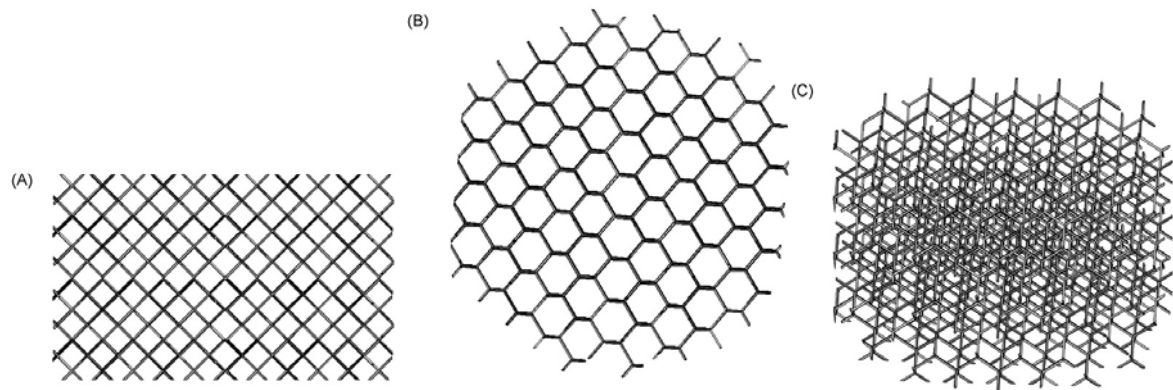
Figure 2: Top (A) and oblique views (B and C) of a CAD rendering of the 10-mm diameter porous EBM scaffolds. The fabricated scaffolds have 70 μm wide struts that form 650 μm diameter hexagonal pores, visible in (B).
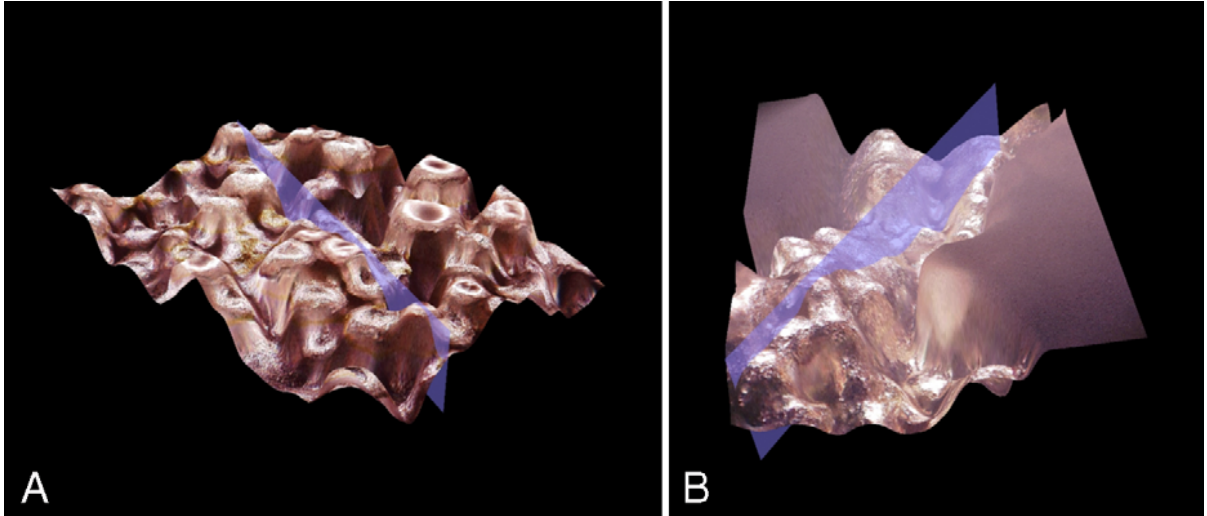
Figure 3: Surface roughness of solid unpolished EBM disc (A) and porous EBM disc (B). The roughness is assessed using a 3D microscope. The microscope captures several 2D images at various depths and reconstructs 3D rendering of these irregular surfaces. A marker (vertical plane) is then placed on the 3D rendering and the surface roughness is measured within that plane. For the porous EBM disc, the plane is placed along the surface of a strut.
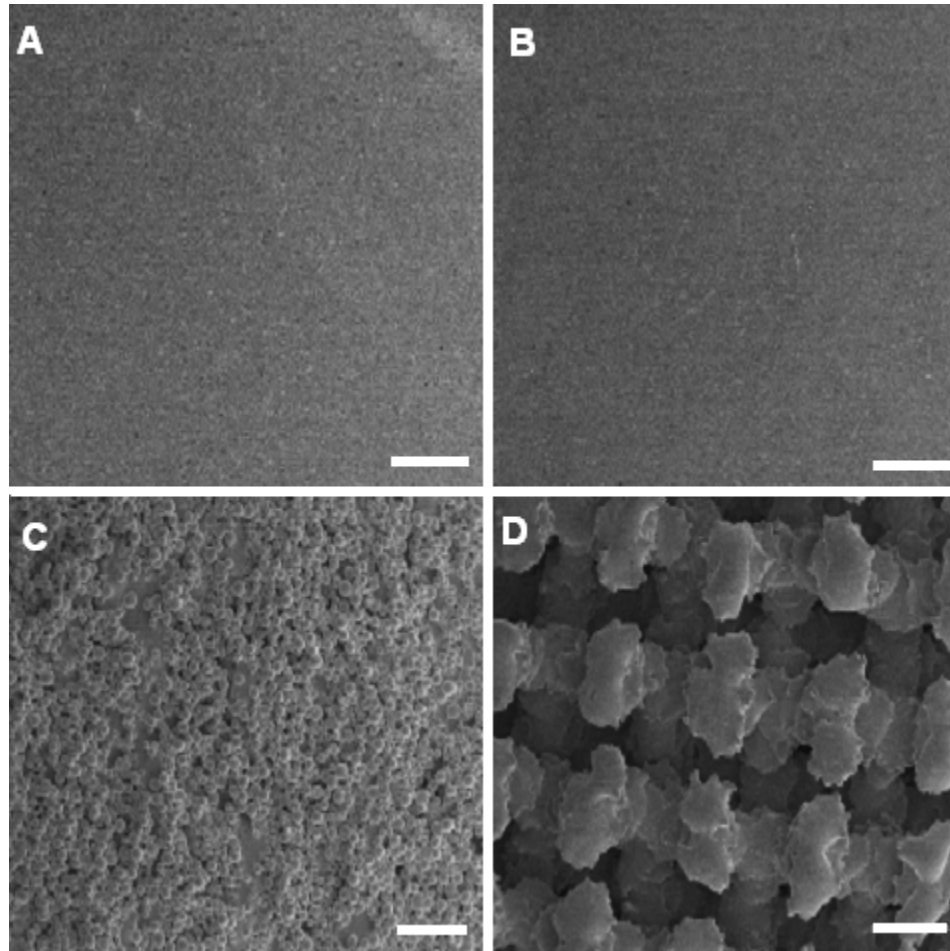
Figure 4: Surface microphotographs made by use of scanning electron microscopy representative of four types of Ti6Al4V discs. The discs include (A) a solid commercial disc, (B) a solid polished disc made using EBM additive manufacturing, (C) a solid unpolished EBM disc, and (D) a porous EBM disc. Sintered TI6Al4V beads are visible on the surface of the solid unpolished EBM disc. Struts of melted Ti6Al4V are visible for the porous EBM disc. Original magnification: 20x, bar = 1mm.
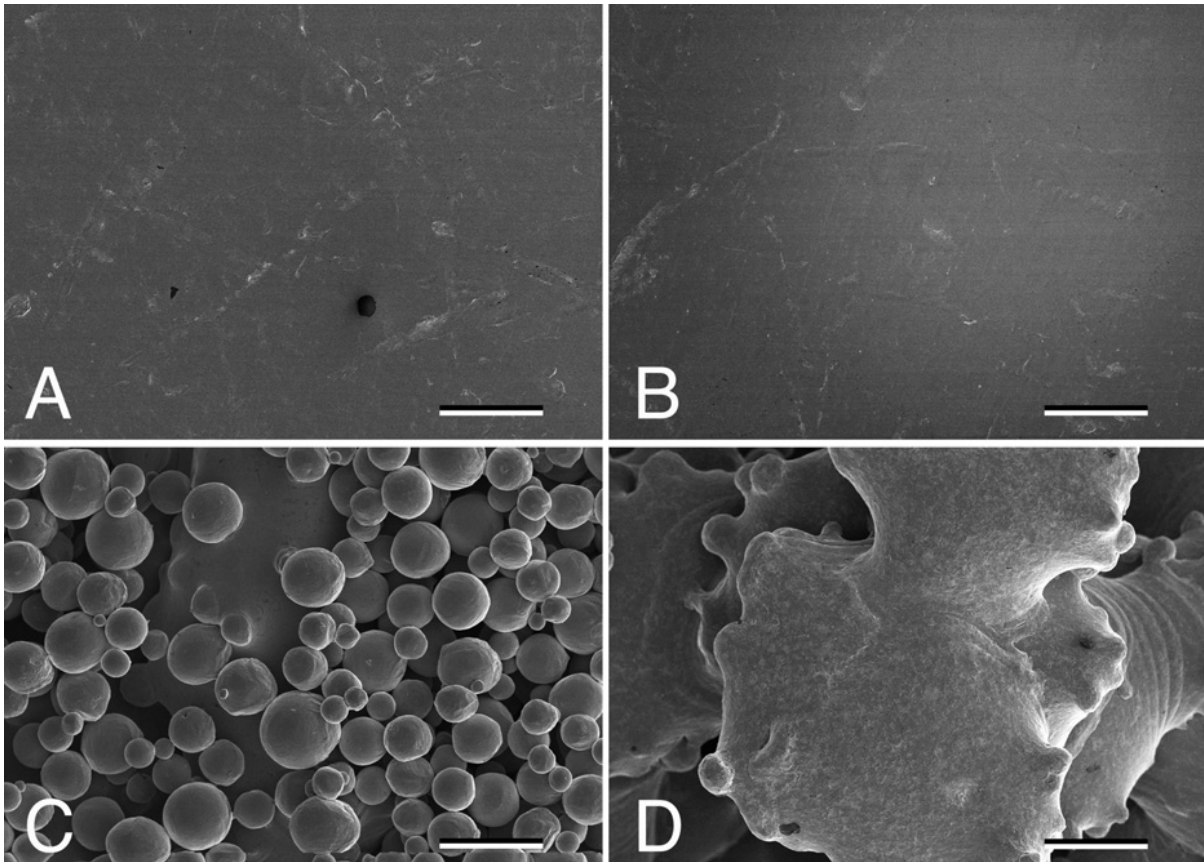
Figure 5: Surface microphotographs made by use of scanning electron microscopy representative of four types of Ti6Al4V discs. The discs include (A) a solid commercial disc, (B) a solid polished disc made using EBM additive manufacturing, (C) a solid unpolished EBM disc, and (D) a porous EBM disc. Sintered TI6Al4V beads are visible on the surface of the solid unpolished EBM disc. Struts of melted Ti6Al4V are visible for the porous EBM disc. Original magnification: 100x, bar = 200μm.

2.2.2 Isolation of human Adipose-Derived Adult Stem Cells

Excess human adipose tissue was obtained from an elective abdominoplasty surgery with

donor consent from a 50-year-old Caucasian female in accordance with a protocol approved by the

Institutional Review Board of the University of North Carolina at Chapel Hill (04-1622). The hASCs were isolated from the adipose tissue using a density and differential adhesion based assay (Bernacki et al., 2008; McCullen et al., 2007; Wall et al., 2007a; Wall et al., 2007b; Nakayama et al., 1997). The isolated cells were cultured in 25 mL complete growth medium (α-MEM) with l-glutamine, 10% fetal bovine serum (Premium Select, Atlanta Biologicals, Lawrenceville, GA), 10,000 I.U. penicillin/10,000 µg/mL streptomycin, 200 mM lglutamine (Mediatech, Inc., Herndon, VA) in tissue culture flasks (one 75cm^2 flask per 5 g initial tissue). The culture flasks were washed with phosphate buffered saline (PBS) to remove non-adherent cells after 24 hours, and fresh growth medium was added. Isolated hASCs were then characterized by their ability to differentiate down osteogenic and adipogenic pathways following chemical stimulation. Human ASC cultures were passaged and cryopreserved at 70–80% confluency, then thawed and re-seeded at a density of 100,000 cells per 75cm^2 flask. The cells used in this study were third passage cells following isolation.

2.2.3 Human Adipose-Derived Stem Cell Seeding on Scaffolds

Three of each of the four scaffold types were placed in individual wells of a 24-well, non-tissue culture treated plate for suspension cells (Sarstedt, Inc., Newton, NC). A seeding density of 20,000 hASCs/20 µL was used for each scaffold, and cells were allowed to adhere for 30 minutes before 2.0 mL growth medium was added to each well.

2.2.4 Cell Proliferation

Human ASC viability and proliferation was determined with a cell viability assay (alamarBlue®, AbD Serotec, Raleigh, NC) at days zero, one, two, three, and seven post-seeding. AlamarBlue® was added to each well five hours before the sampling time point at a volume of 10% of the culture medium. After incubation of the alamarBlue®, 200 μL samples were taken in triplicate and the absorbance read at 570 and 600 nm using a microplate reader (Tecan GENios, Tecan, Switzerland). The percent reduction of alamarBlue® for cells growing on the EBM porous, EBM polished, and EBM unpolished scaffolds were compared to the commercial samples. Greater alamarBlue® reduction was indicative of greater hASC proliferation (Nakayama, 1997). Mixed model analysis of variance was performed using statistical analysis software (JMP 8.0, SAS Institute, Cary, NC). Significance was set at $P < 0.05$.

2.2.5 Cell Viability

Cell viability was assessed eight days after seeding using a Live/Dead viability cytotoxicity kit (Molecular Probes, Eugene, OR). The discs were washed twice in phosphate buffered solution (PBS) and incubated in a calcein AM/ethidium homodimer-1 solution for fifteen minutes in the dark. A fluorescence microscope (Leica Microsystems Inc., Bannockburn, IL) was used to image the cells on the scaffolds with a 10× objective. The samples were photographed using image analysis software (SimplePCI, Compix Inc. Imaging Systems, Cranberry Township, PA). For the porous EBM discs, cell viability was judged based on the surface layer of the scaffold.

2.2.6 Cytokine Analysis

Culture media were extracted from the wells at days zero, one, two, three, and seven post-seeding to analyze cytokine production. Extracted media were frozen at −20 °C and stored before analysis. IL-6 and IL-8 concentrations in the pooled media were measured using a fluorescent microplate reader (Bio-Plex suspension array system, Bio-Rad Laboratories, Hercules, CA). The system simultaneously assayed the two cytokines using 50 µL of the cell culture medium. Beads (5.6 µm diameter) conjugated to capture antibody specific to IL-6 and IL-8 were incubated in a 96-well filter plate with each sample (three replicates per sample). The beads were then incubated with a fluorescent-labeled reporter molecule that specifically bound the analyte. The contents of each well were then analyzed in the Bio-Plex array with IL-6 and IL-8 quantitated relative to cytokine-specific standard curves (Luminex xMAPTM Technology, Luminex Corporation, Austin, TX). The limit of detection was 1.1 and 0.5 pg/mL for IL-6 and IL-8, respectively. Cytokine concentrations (pg/mL) were normalized to cell numbers using cell viability measurements (alamarBlue® reduction) and were compared among groups using a least significant difference ANOVA (SAS 9.1 for Windows, SAS Institute, Cary, NC). Multiple comparisons among different scaffolds were conducted using Student's t-tests. Significance was set at $P < 0.05$.

2.3 Results

2.3.1 Surface Analysis of Discs

The mean ± standard deviation (SD) surface roughness (Ra) was 34 ± 10µm, 40 ± 10µm, 0.38

± 0.18μm, and 0.39 ± 0.08μm for the porous EBM, unpolished EBM, polished EBM, and commercial discs, respectively.

2.3.2 Cell Proliferation

Mean alamarBlue® reduction for porous EBM, unpolished EBM, polished EBM, and commercial discs at day seven was 43.3%, 36.7%, 34.4%, and 33.7%, respectively (Figure 6). Mean alamarBlue® reduction was greater for cells exposed to EBM porous discs than exposed to commercial discs on days two, three, and seven (P = 0.036, 0.049, and 0.002, respectively), indicating greater cell proliferation. Mean alamarBlue® reduction was also greater for cells seeded on EBM porous discs than seeded on EBM polished and EBM unpolished discs at day seven (P = 0.003 and <0.001, respectively).
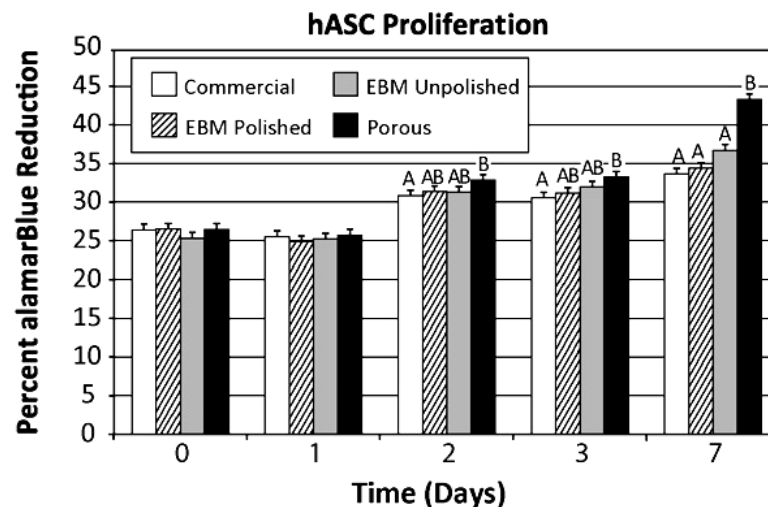
Figure 6: alamarBlue® reduction by hASC seeded on four types of Ti6Al4V discs. The discs include solid commercial discs, solid polished discs fabricated with EBM, solid unpolished EBM discs, and porous EBM discs. Within time periods, different letters indicate statistically significant differences between responses (P < 0.05).

2.3.3 Cell Viability

Differences in cell viability among commercial, EBM polished, EBM unpolished, and EBM porous scaffolds were not detected after eight days in culture (Figure 7). Live cells were visible on images collected at various depths of the porous EBM scaffolds. Changes in surface topography for unpolished and porous EBM discs somewhat obscured the view of hASCs in the two-dimensional (2D) images; however, the number of live cells observed on unpolished discs appeared comparable to the number of cells observed on the smooth discs. Live cells also appeared attached and spread along the struts of the porous discs at varying depths (data not shown).
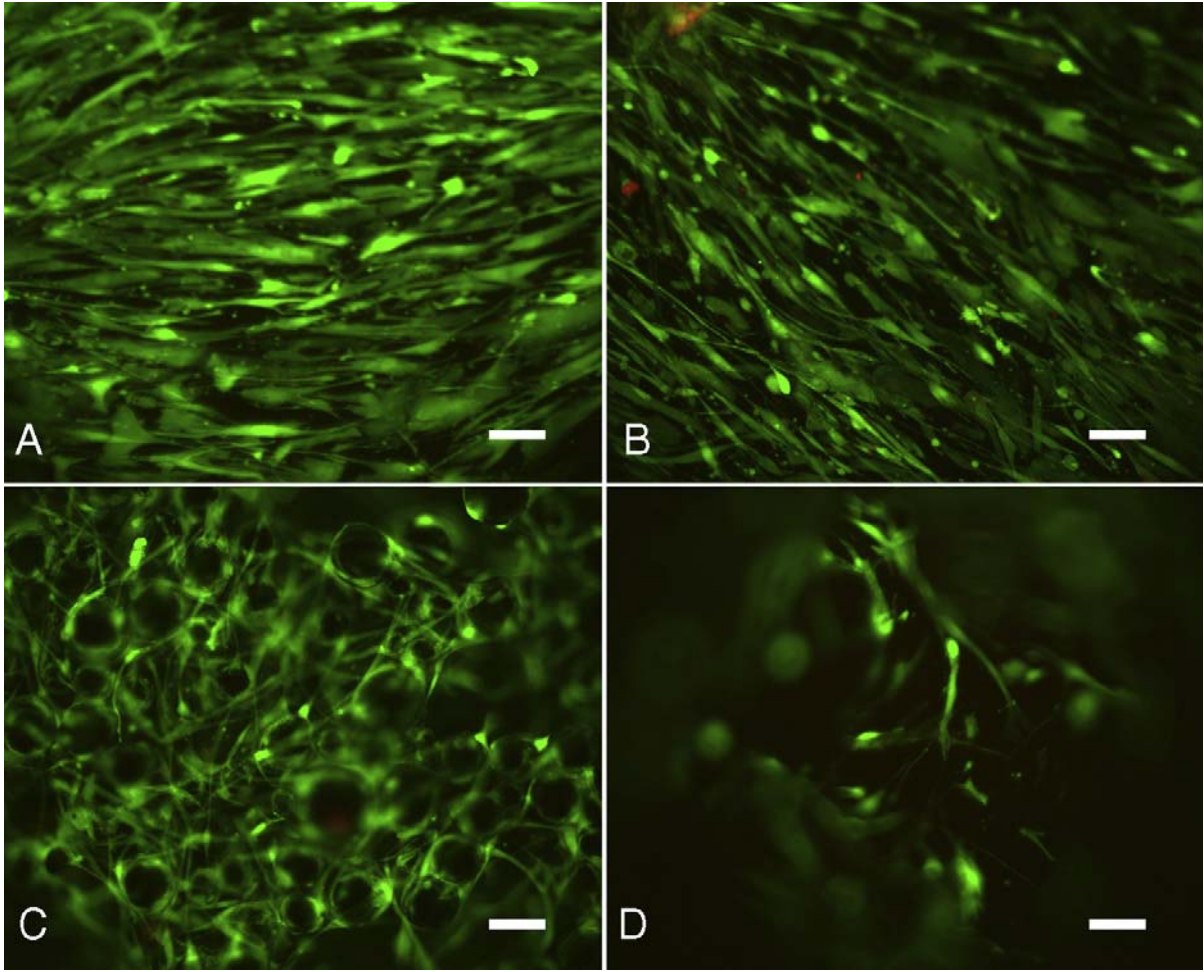
Figure 7: LIVE/DEAD® fluorescence microphotographs of hASCs seeded on Ti6Al4V discs. The discs include (A) solid commercial discs, (B) solid polished discs made using electron beam melting additive manufacturing, (C) solid unpolished EBM discs, and (D) porous EBM discs. Live cells are stained green and dead cells are stained red. Two dead cells are visible in B and one in C. For images from unpolished EBM discs, dark areas correspond to peaks of the Ti6Al4V surfaces. Original magnification: 10x, bar=100μm.

2.3.4 Release of Cytokines IL-6 and IL-8

The mean (± SEM) IL-6 concentration after seven days in culture was higher in wells with polished EBM discs (10,210 ± 238 pg/mL) than in wells with commercial (4339 ± 503 pg/mL, $P <$

0.001), EBM unpolished (3622 ± 538 pg/mL, P < 0.001), and porous EBM discs (2767 ± 288 pg/mL, *P* < 0.001, Figure 8). Also, the mean IL-6 concentration was higher in wells with commercial discs than in wells with porous EBM discs (*P* = 0.019). The mean (± SEM) IL-8 concentration after seven days in culture was higher in wells with commercial (1294 ± 177 pg/mL) and polished EBM discs (1143 ± 140 pg/mL) than in wells with EBM unpolished (283 ± 22 pg/mL, *P* < 0.001 and 0.001, respectively) and porous EBM discs (136 ± 6 pg/mL, *P* < 0.001 and 0.001, respectively, Figure 9). Also, the mean IL-8 concentration was higher in wells with EBM polished discs than in wells with porous EBM discs (*P* < 0.001).
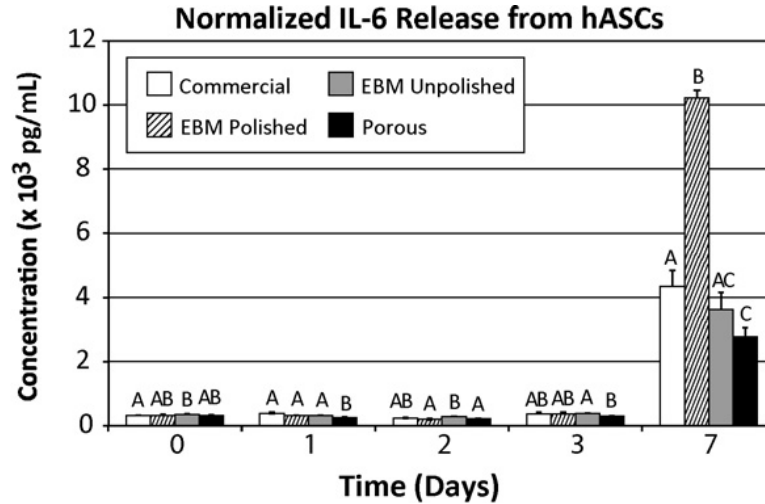
Figure 8: Mean (±SEM) concentration of interleukin 6 (IL-6) released by hASCs seeded on Ti6Al4V discs. The results were normalized to cell counts, determined using alamarBlue® reduction. The discs include solid commercial discs, solid polished discs fabricated with EBM, solid unpolished EBM discs, and porous EBM discs. Within time periods, different letters indicate statistically significant differences between responses (*P* < 0.05).
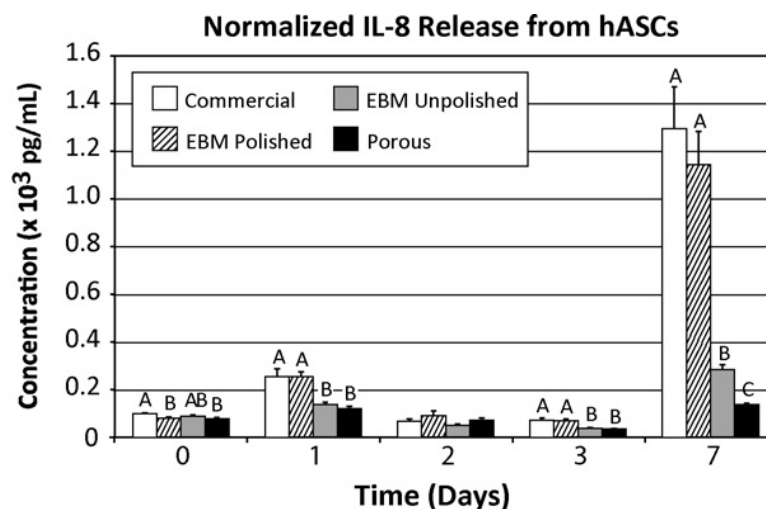
Figure 9: Mean (±SEM) concentration of interleukin 8 (IL-8) released by hASCs seeded on Ti6Al4V discs. The results were normalized to cell counts, determined using alamarBlue® reduction. The discs include solid commercial discs, solid polished discs fabricated with EBM, solid unpolished EBM discs, and porous EBM discs. Within time periods, different letters indicate statistically significant differences between responses ($P < 0.05$).

2.4 Discussion

Custom titanium implants may be fabricated using a variety of methods, including machining, additive manufacturing (AM), and porous coatings applied by post-processing methods such as plasma-spraying, shot-blasting, and acid etching (Karageorgiou et al., 2005; Lopez-Heredia et al., 2008). Direct metal fabrication (DMF) offers advantages over other fabrication methods because it may be used to build patient-specific implants with solid and porous portions directly from computer aided design (CAD) files. Several DMF methods relying on electron beams or laser beams have been used to make orthopedic implants (Murr et al., 2009). Laser-based DMF methods include laser engineered net shaping (LENS; also known as direct metal deposition and laser additive manufacturing) and selective laser sintering (also known as selective laser melting and direct metal

23

laser sintering). A wide variety of metal and ceramics used in orthopedic implants have been processed using LENS, including Ti, Ti6Al4V, Ti–CoCrMo, TiNi, Ti–Ta, and TCP-Ti (Bandyopadhyay et al., 2009; Krishna et al., 2009; Roy et al., 2008; Vamsi et al., 2008). Laser-based systems often use finer powder than EBM-based systems, leading to smoother surfaces and finer details. Biocompatible metals processed using EBM have included Ti6Al4V, and commercially pure Titanium (Harrysson et al., 2008; Marcellin-Little et al., 2008). EBM-based DMF is more energy efficient than laser based DMF because of higher power efficiency (90% for EBM, 40% for laser) and because reflectance losses present in laser-based DMF leads to further loss of efficiency (Taminger et al., 2006). EBM-based systems usually use a coarser powder and a higher power density, resulting in faster fabrication than laser-based systems. The porous EBM scaffold evaluated in this research could be used as bone ingrowth surface coating on a solid implant or as the core of a porous implant designed to reduce stress shielding in bone.

Little is known about the biological response to EBM-processed titanium structures (Thomsen et al., 2009). Therefore, in this study human stem cell viability, proliferation, and cytokine expression to EBM-processed solid and porous structures were assessed. Because all structures tested in this study were made of Ti6Al4V, a material that is considered highly biocompatible (Van, 1987), it was anticipated that EBM structures would successfully host cells. This study confirms that unpolished and polished solid Ti6Al4V EBM structures and porous Ti6Al4V EBM structures have biocompatibility profiles with hACS that are no more cytotoxic than polished structures made of commercial Ti6Al4V. The proliferation at day seven and survival at day eight of cells seeded on porous EBM scaffolds shows that these structures support the ongrowth and ingrowth of native

tissue and cells. This suggests that various forms of EBM implants will have an acceptable *in vivo* biocompatibility profile. This is in agreement with the findings of a six week biocompatibility study of polished and unpolished solid EBM implants placed in rabbit femora and tibiae (Thomsen et al., 2009).

Human ASCs were used in this study because of their relative abundance and ease of harvest. Cell proliferation, viability, and cytotoxic response were analyzed, but osteodifferentiation was not stimulated or evaluated. Future studies could address differences in differentiation of hASCs seeded on EBM structures with varying geometry and roughness. The biological response to textured (sandblasted, acid etched) titanium surfaces is enhanced compared to smooth surfaces (Daugaard et al., 2008; Shim et al., 2009). While the surface roughness of the unpolished surfaces tested in this study (Ra of 30–40µm) was larger than the classic surface roughness of sandblasted acid-etched implants (Ra of 3–4µm), (Zhao et al., 2007), unpolished EBM surfaces could possibly lead to an enhanced biological response, compared to smooth surfaces. In a study comparing smooth and rough EBM-processed Ti6Al4V implant surfaces; no differences were identified between osteoblast differentiation over fourteen days of induction (Ponader et al., 2008). Textured surfaces also have the mechanical advantage of increased mechanical interlocking of the bone and implant, compared to smooth surfaces (Story et al., 1998). The increased proliferation of hASCs on EBM porous implants compared to polished implants suggests that porous EBM scaffolds may enhance bone growth compared to smooth polished implants.

Cell viability and proliferation was assessed using the alamarBlue® assay. Significantly larger alamarBlue® reduction was present on days two, three, and seven for the EBM porous scaffolds compared to the commercial samples. Reduction of the alamarBlue® dye is performed by living cells,

indicating a significantly greater cell number on porous scaffolds than commercial discs at these time points. The significant increase in cell number at these time points may have resulted from the increased surface area in EBM porous discs compared to solid discs. The porous design allowed for cell growth into the sample along the struts, and the presence of large pores likely allowed for better nutrient delivery and waste removal for cells that had migrated into the scaffold. The increased surface roughness of the porous samples compared to polished samples may also have influenced hASC proliferation. It has previously been shown that bone ongrowth onto microtextured acid-etched Ti6Al4V surfaces is increased compared to non-textured Ti6Al4V surfaces (Daugaard et al., 2008). It has also been shown that surface roughness enhances the attachment and proliferation of anchorage-dependent bone forming cells on hydroxyapatite ceramic rods (Yuan et al., 1999). LIVE/DEAD® staining images supported the proliferation results, confirming that viable cells were present on all scaffold types throughout the experimental period and that few dead cells were present. Further, images obtained from the porous EBM scaffolds also showed viable cells throughout the three-dimensional (3D) pores of the scaffold, something difficult to convey in two-dimensional (2D) images.

The concentrations of the proinflammatory cytokines IL-6 and IL-8 in response to contact with the Ti6Al4V surfaces were assessed. IL-6 and IL-8 were selected because they are involved in local and systemic inflammatory responses (Min et al., 2001). IL-6 is produced in response to stimulation by almost all human cells including adipocytes (Imamura et al., 1994; Min et al., 2001; Schwaighofer et al., 1994). High serum levels of IL-6 may be an indicator of early transplant-related complications (Min et al., 2001). The primary activity of IL-6 lies in the acute phase response, and is often correlated with an elevated body temperature. Higher tissue temperature may create an

unsuitable living environment for some pathogens, but it is not a desirable response when human cells are exposed to biomaterials. IL-8, also known as CXCL8, is a chemokine. *In vivo*, chemokines act on leukocytes rolling along blood vessel walls, causing them to bind, travel through vessel walls, and migrate towards infection sites following the concentration gradients of the chemokine (Janeway, 2005). The amount of IL-6 and IL-8 released by hASCs on unpolished and porous Ti6Al4V EBM discs was equal to, or significantly lower than, the amount released by hASCs on commercial Ti6Al4V discs, suggesting that EBM processing does not adversely affect the properties of the Ti6Al4V as it does not elicit an increased immunogenic response. The higher amount of IL-6 and IL-8 released from hASCs on polished EBM discs compared to unpolished and porous EBM discs could be linked to the fact that cells were more confluent on the smooth surfaces than on the textured surfaces. To our knowledge, however, the effect of cell confluence on cytokine secretion has not been reported. Changes in cytokine secretion could be linked to cell adhesion and hASCs adhesion might have been more rapid on textured EBM surfaces than on smooth EBM surfaces. Osteoblast attachment to rough surfaces has been shown to be more rapid than attachment to smooth surfaces (Bowers et al., 1992; Sammons et al., 2005). Rapid attachment of hASCs suggests improved compatibility with scaffold surface properties and could account for the reduced cytokine expression. The *in vivo* cytokine response to Ti6Al4V EBM structures has not been described nor correlated with the *in vitro* response to these implants. In one study involving biopsies from 29 patients, the *in vitro* cytokine response (including the IL-6 response) to polymethylmethacrylate was positively correlated to the *in vivo* cytokine response to cemented hip prostheses (Stea et al., 2000). In a cutaneous toxicity study, the *in vitro* cytokine expression of porcine keratinocytes was similar to their cytokine expression *in vivo* (Allen et al., 2001). The findings from this *in vitro* study indicate that EBM structures can

successfully host living cells. Furthermore, we have shown that EBM-fabricated porous titanium structures generally resulted in reduced cytokine production and greater cell proliferation than commercially produced titanium structures, suggesting that solid and porous EBM structures are suitable for the fabrication of orthopedic implants.

2.5 Conclusions for hASCs Response to EBM Titanium

Viability, proliferation, and cytokine production of hASCs on EBM titanium discs was assessed *in vitro*. EBM was used to produce titanium structures with several surface topographies that were compared to commercially available titanium alloy discs. The results of these studies indicated that a porous EBM structure supported increased hASC proliferation and did not lead to an increase in the release of the cytokines IL-6 and IL-8, compared to titanium alloy discs from a commercial source. These results suggest that EBM-processed porous and unpolished solid structures are acceptable orthopedic implants that would potentially promote cell ongrowth and ingrowth.

3.0 NHDF-NEO AND NHEK RESPONSE TO EBM TITANIUM

3.1 Introduction

Amputees often rely on socket prostheses but these prostheses have suboptimal load transfers via the soft tissues, which can lead to painful skin irritations and infections (Albrektsson et al., 1983). The load transfers to transdermal osseointegrated implants are enhanced, compared to socket prostheses because of stable fixation to the bone (Asaoka et al., 1985; Clemow et al., 1981; Thomas et al., 1987). Patient-specific osseointegrated implants fit securely on the residual bone, reducing micromotion and promoting bone ingrowth (Asaoka et al., 1985; Okumura et al., 2001; Simmons et al., 1999; Thomas et al., 1987). The stability of bone-implant interfaces may be enhanced by use of custom metal implants that are in close contact with bone (Albrektsson et al., 1983; Asaoka et al., 1985; Puleo et al., 1999; Simmons et al., 1999; Thomas et al., 1987). The complex geometry of bone makes implant fabrication using conventional material removal processes (machining) very challenging. The potential addition of porous portions on the implants surface presents further fabrication challenges that increase the cost and complexity of these implants. Electron beam melting (EBM) is an additive manufacturing method using layer-based technology to produce custom designed implants from patient computed tomography (CT) scans using metal powder (Cormier et al., 2004). EBM enables the fabrication of freeform implants using titanium alloys or cobalt-chromium alloys that may have solid and porous portions.

In addition to stable bone-implant interfaces, the optimal transdermal osseointegrated

implants would ideally have surfaces that promote skin and subcutaneous tissue ongrowth leading to skin-implant interfaces resistant to bacterial infections. Little is known, however, about the *in vivo* and *in vitro* responses of skin cells to metal implants with variable surface textures (Groessner-Schreiber et al., 2002; Größner-Schreiber et al., 2006; Könönen et al., 1992; Meredith et al., 2007; Rompen et al., 2006).

Osseointegrated, transcutaneous implants require both bone and soft tissue ingrowth for success.   The bone ingrowth is required for implant stability, while skin ingrowth is necessary to provide an infection barrier. This research has shown in the previous chapter that human adipose-derived adult stem cells (hASCs) can thrive on EBM surfaces, both polished and as-processed. However, the ability for EBM surfaces to host skin cells need to be analyzed. That response has been evaluated by assessing the survival and proliferation of keratinocytes and dermal fibroblasts after exposure to metal implants (Groessner-Schreiber et al., 2002; Größner-Schreiber et al., 2006; Könönen et al., 1992; Meredith et al., 2007; Rompen et al., 2006). The purpose of this project was to assess the response of dermal fibroblasts and keratinocytes to EBM-processed titanium alloy implants with varying surfaces roughness. We hypothesized that the survival and proliferation of keratinocytes and fibroblasts after exposure to EBM-processed titanium alloy discs were equal to survival and proliferation after exposure to discs made of commercial titanium alloy.

3.2 Materials and Methods

3.2.1 Fabrication and Preparation of Scaffolds for NHDF-Neo and NHEK Cell Seeding

In total 64 titanium alloy (Ti6Al4V) discs, 10 mm in diameter and 4 mm in height (Figure 10)

and sixteen 12 mm diameter glass coverslips were prepared for seeding Neonatal Normal Human Dermal Fibroblasts (NHDF-Neo) and Normal Human Epidermal Keratinocytes (NHEK) in separate culture experiments. Polished commercially-purchased Ti6Al4V (Group A) was used as a control. The three other groups were all fabricated with EBM using Ti6Al4V powder with different surface topographies: polished (Group B), unpolished (Group C), and unpolished porous (Group D). A second control was included to compare to the Ti6Al4V, glass coverslips (Group E). The commercially-purchased discs were machined to the final dimensions from a Ti6Al4V, Grade 5 rod meeting ASTM B348 standards (McMaster-Carr Supply Company) using a computer numerically controlled (CNC) lathe (Hawk 150, MAG Cincinnati, Hebron, KY). The polished EBM-fabricated discs were machined in the same manner to the same dimensions as the titanium control group. Both polished groups were abraded using successive grits from 240 to 2000 silicon carbide papers, followed by polishing with 6 µm diamond, 1.0 µm Al_2O_3, and 0.3 µm Al_2O_3. The unpolished groups were blasted with titanium powder from the build process to remove any loose particles from the surface.

Surface roughness of the porous and unpolished titanium scaffolds were determined from height versus distance data acquired from 3D surface topography images using a 3D microscope (KH-7700, Hirox, Hackensack, NJ). Four measurements at randomly selected points were collected from four porous and unpolished scaffolds. Surface profilometry (Mitutoyo Surftest 212, Mitutoyo U.S.A., Aurora, IL) was used to assess the surface roughness of the polished Ti6Al4V discs and glass discs. Four measurements were collected at random locations from four of each type of disc.

All discs were cleaned per the surgical implant sterilization protocol at the North Carolina

State University College of Veterinary Medicine (Raleigh, NC). Scaffolds were sprayed with a multi-tiered enzymatic foam, specifically Prepzyme® X.F. eXtreme Foam (Ruhof Corporation, Mineola, NY), washed with an ultrasonic bath, rinsed with distilled water, dried with pressurized air, and steam sterilized in sealed packages.
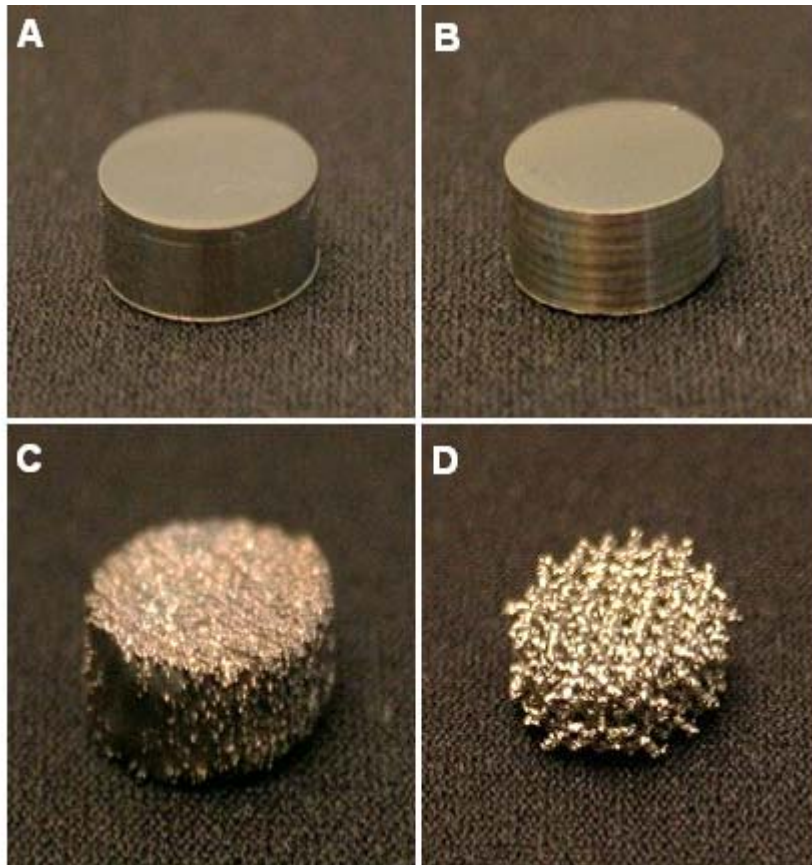
Figure 10: Ti6Al4V disc-shaped scaffolds for seeding with normal neonatal human dermal fibroblasts and normal human epidermal keratinocytes; A) polished discs from a commercial source, B) polished discs fabricated with electron beam melting, C) unpolished EBM fabricated discs, D) unpolished, porous EBM fabricated discs. The discs measure 10 mm in diameter and 4 mm in height.

3.2.2 Preparing and Seeding NHDF-Neo and NHEK Cells for Culture

NHDF-Neo cells enzymatically derived from a single male newborn of an unknown race were

purchased from Lonza (Walkersville, MD) and passaged twice prior to being cryogenically preserved at 200,000 cells per cryogenic tube. Cells were thawed and entire tube was harvested and cultured into a 75 mL flask (Nunc, Thermo Fisher Scientific, Rochester, NY) with 20 mL of warmed Fibroblast Growth Medium (FGM®-2, Lonza) and incubated at 37°C in 5% CO_2. Cells were grown for four days with a medium change at day two. Cells were microscopically analyzed at day four and appeared healthy and approximately 25% confluent. Cells were washed twice with 10.0 mL of phosphate buffered saline (PBS), 3.0 mL of trypsin was added to detach cells from flask, 6.0 mL of trypsin neutralizing solution (TNS) was added, and cell suspension was transferred into 15.0 mL conical tube. Cells were pelleted by centrifugation at 70 x g for five minutes, supernatant was aspirated, and cells were resuspended in 1.0 mL of FGM®-2 medium. Using a hemacytometer cells were counted to determine proper dilution. Approximately 500,000 cells were harvested.

The scaffolds were placed into two Falcon® 24-well non-tissue culture treated flat bottom plates (Becton Dickinson and Company, Franklin Lakes, NJ). Five scaffolds of each type were seeded with 1×10^4 cells at a volume of 50 µL, while the remaining three scaffolds were used as negative controls for the proliferation analysis. After the cell solution was added to the top surface of the scaffolds they were incubated at 37°C in 5% CO_2 for one hour to allow the cells to adhere. Then 1.0 mL of pre-warmed FGM-2 medium was slowly added to all wells. The culture plates were then incubated at 37°C in 5% CO_2. At day two cells were microscopically observed and randomly selected wells contained healthy cells with few cells visible on the plate. Growth medium was observed as non-cloudy and light orange/pink in color for all cultured wells with no evidence of contamination and minimal cells on culture plate.

Preparation of the NHEK cells was identical to the NHDF-Neo cells with only a few exceptions; growth medium and seeding density. NHEK cells were cultured in Keratinocyte Growth Medium (KGM®-2, Lonza). Cells were seeded on each scaffold at a density of 1.5×10^4 cells per 50 μL.

3.2.3 Analyzing NHDF-Neo and NHEK Cell Proliferation on Titanium Scaffolds

Eight of each scaffold type was used to evaluate HDF viability and proliferation at two time points, two and seven days. Forceps were cleaned in 70% ethanol and then used to aseptically transfer scaffolds to new 24-well non-tissue culture treated flat bottom plate in order to insure non-adherent cells would not be analyzed. Cell-free control scaffolds/coverslips were transferred first followed by the seeded scaffolds to avoid any cells being transferred to cell free wells. A 1.0 mL solution of growth medium containing 10% (v/v) alamarBlue® reagent was added to each well. NHDF-Neo cells with alamarBlue® were incubated at 37°C in 5% CO_2 for 6.5 and 4 hours for the two and seven day experiments, respectively. NHEK cells were incubated at 37°C in 5% CO_2 for 6 and 10 hours for the two and seven day experiments, respectively. At each time point each well was aspirated and the alamarBlue® solution was collected into labeled snap cap tubes. From these tubes, 200 μL was transferred in triplicate into 96-well plates (Fisher Brand, Deerfield, IL). Centrifugation at 400 x g for three minutes was used to remove air bubbles. The plates were subsequently analyzed with a microplate reader (GENios, Tecan Group, Maennedorf, Switzerland) and Magellan5 software using the alamarBlue® absorbance method for both 570 nm and 600 nm measurements.

No-cell control samples (n = 3) were treated identically. Average percent reduction values were normalized for the hours of incubation for comparison purposes. Statistical analysis was completed with statistical software (JMP 8.0, SAS Institute, Cary, NC) using two-tailed Student's t-tests and significance set at $P < 0.05$.

3.2.4 Analyzing NHDF-Neo and NHEK Cell Viability on Titanium Scaffolds

Cell viability was assessed using a fluorescence-based LIVE/DEAD® assay for the NHDF-Neo and NHEK, at seven and eight days respectively. Cells were washed twice with phosphate buffered solution (PBS, Fisher Scientific, Fair Lawn, NJ) before staining. The staining solution was a mixture of 1.0 µL calcein AM, 4.0 µL EthD-1, and 2.0 mL PBS. For each scaffold, 50 µL of staining solution was added to the top of a 24-well culture plate lid, where the circles met tangentially, and scaffolds were placed with the cell surface inverted. Scaffolds were incubated for ten minutes and imaged at 10x magnification using a microscope (Leica DMIL, Deerfield, IL) and imaging software (QCapture, Qimaging Micropublisher Imaging System, Canada).

3.3 Results

3.3.1 Surface Roughness

The mean ± standard deviation surface roughness (Ra) values for the scaffolds were 0.27 ± 0.12, 0.32 ± 0.12, 34.84 ± 12.03, 22.01 ± 10.17, and 0.06 ± 0.01 µm, for the commercial polished, polished EBM, unpolished EBM, porous EBM, and glass scaffolds, respectively.

3.3.2 NHEK and NHDF-Neo Proliferation

On day seven, NHDF-Neo cells reduced the alamarBlue® by 7.7, 7.9, 5.7, 5.4, and 11.6% per hour of incubation on commercial polished, polished EBM, unpolished EBM, porous EBM, and glass coverslips, respectively (Figure 11). AlamarBlue® reduction was higher for NHDF-Neo cells cultured on glass coverslips than on all metal discs (P < 0.001 for all metal discs types) and was higher for cells seeded on polished EBM discs than on unpolished (P < 0.001) and porous EBM discs (P < 0.001). All NHDF-Neo P-values from the student's t-test statistical analysis are listed in Table 1.

On day seven, NHEK cells reduced the alamarBlue® by 2.4, 1.9, 1.3, 1.2, and 2.5% per hour of incubation for commercial polished, polished EBM, unpolished EBM, porous EBM, and glass coverslips, respectively (Figure 12). AlamarBlue® reduction was higher for NHEK cells cultured on glass coverslips than for cells cultured on all metal discs (P < 0.001 for all metal discs types) and was higher for polished EBM discs than unpolished (P < 0.001) and porous EBM discs (P < 0.001). A complete tabulation of the P-values from the student's t-test statistical analysis for NHEK proliferation results are listed in Table 2.
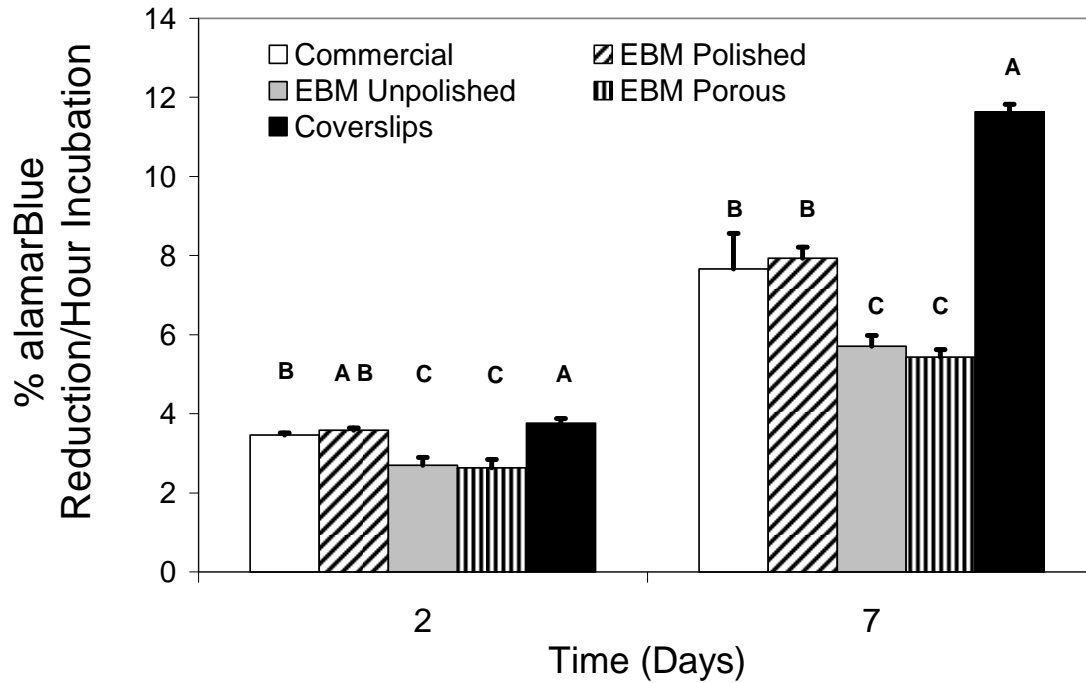
Figure 11: Mean (± SEM) alamarBlue® reduction (in %, per hour of incubation) by NHDF-Neo seeded on four types of Ti6Al4V discs and on glass coverslips. The discs include polished commercial Ti6Al4V discs, polished EBM discs, unpolished EBM discs, porous EBM discs, and glass coverslips. Within time periods, different letters indicate statistically significant differences between responses ($P < 0.05$).

Table 1: Statistical p-values for NHDF-Neo cells seeded onto scaffolds, commercial polished, EBM polished, EBM unpolished, EBM porous, and glass coverslips.

Group	Comparison Group	p-Value	
		2 Day	7 Day
Commercial Polished	EBM Unpolished	<0.001	< 0.001
Commercial Polished	EBM Porous	< 0.001	< 0.001
EBM Polished	Commercial Polished	0.326	0.627
EBM Polished	EBM Porous	< 0.001	< 0.001
EBM Polished	EBM Unpolished	< 0.001	< 0.001
EBM Unpolished	EBM Porous	0.542	0.631
Glass Coverslip	Commercial Polished	0.017	< 0.001
Glass Coverslip	EBM Polished	0.148	< 0.001
Glass Coverslip	EBM Unpolished	< 0.001	< 0.001
Glass Coverslip	EBM Porous	< 0.001	< 0.001
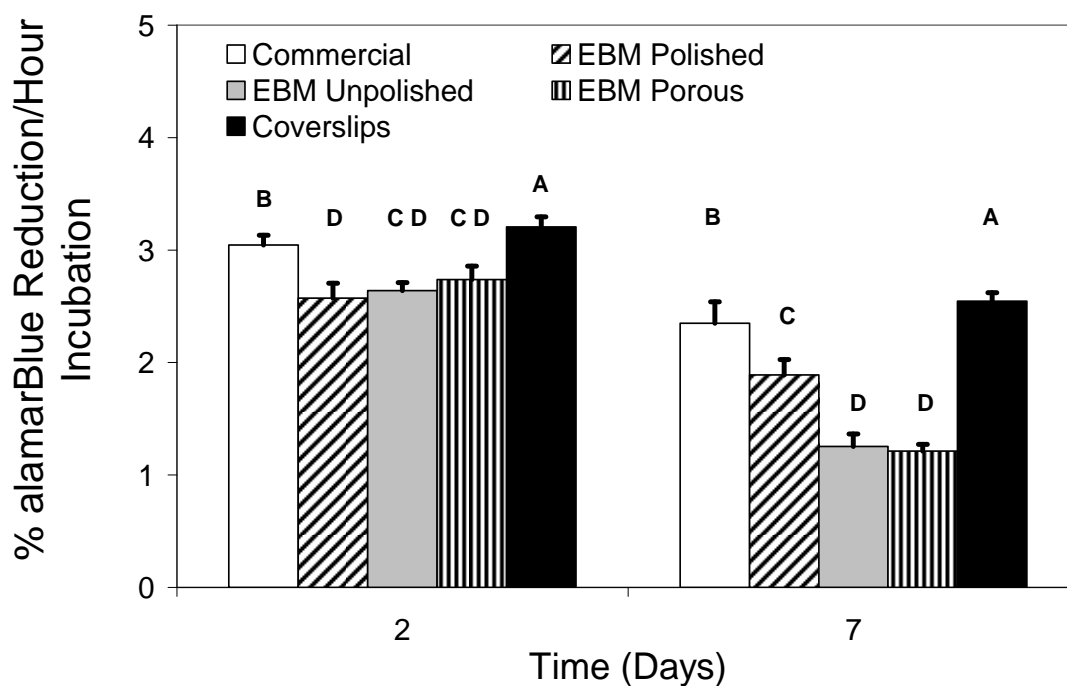
Figure 12: Mean (± SEM) alamarBlue® reduction (in % per hour of incubation) by NHEK seeded on four types of Ti6Al4V discs and on glass coverslips. The discs include polished commercial Ti6Al4V discs, polished EBM discs, unpolished EBM discs, porous EBM discs, and glass coverslips. Within time periods, different letters indicate statistically significant differences between responses ($P < 0.05$).

Table 2: Statistical p-values for NHEK cells seeded onto scaffolds, commercial polished, EBM polished, EBM unpolished, EBM porous, and glass coverslips.

		p-Value	
Group	**Comparison Group**	**2 Day**	**7 Day**
Commercial Polished	EBM Unpolished	< 0.001	< 0.001
Commercial Polished	EBM Porous	< 0.001	< 0.001
EBM Polished	Commercial Polished	< 0.001	< 0.001
EBM Polished	EBM Porous	0.0439	< 0.001
EBM Polished	EBM Unpolished	0.4126	< 0.001
EBM Unpolished	EBM Porous	0.224	0.656
Glass Coverslip	Commercial Polished	0.044	0.0402
Glass Coverslip	EBM Polished	< 0.001	< 0.001
Glass Coverslip	EBM Unpolished	< 0.001	< 0.001
Glass Coverslip	EBM Porous	< 0.001	< 0.001

3.3.3 NHDF-Neo and NHEK Viability

Live NHDF-Neo cells were visible on all scaffold types (Figure 13). The cell status for the top surface of each scaffold was analyzed. For polished discs and glass coverslips, living cells were highly confluent in the center of the discs, where cells were initially seeded, and less confluent at the edge. Cells on all discs were long, spindle-shaped growing on parallel arrays, but appeared to be more closely oriented on the discs with smooth surfaces. More dead cells were present on the unpolished and porous titanium discs than on the polished discs and glass coverslips.

Discs seeded with NHEK cells had many dead cells and either none or few live cells present. One of the commercial polished discs had visible living cells (Figure 14A), while the remaining four discs had only dead cells present (data not shown). Cells appeared to be spindle-shaped, fibroblastic-like cells and had visibly differentiated. Live and dead cells were visible on all EBM polished discs. Live cells were irregular in shape and had many spindles protruding from a center body (Figure 14C). EBM unpolished discs had few visible living cells which were rounded in shape (Figure 14E) and some areas containing many dead cells. EBM porous discs had very few cells visible; both living and dead. Cell shape was difficult to determine on the porous discs due to the three-dimensional (3D) structure of the discs. Glass coverslips had visible living and dead cells, with the dead cells more numerous than live cells. Some living cells were spindle-shaped while others were rounded.
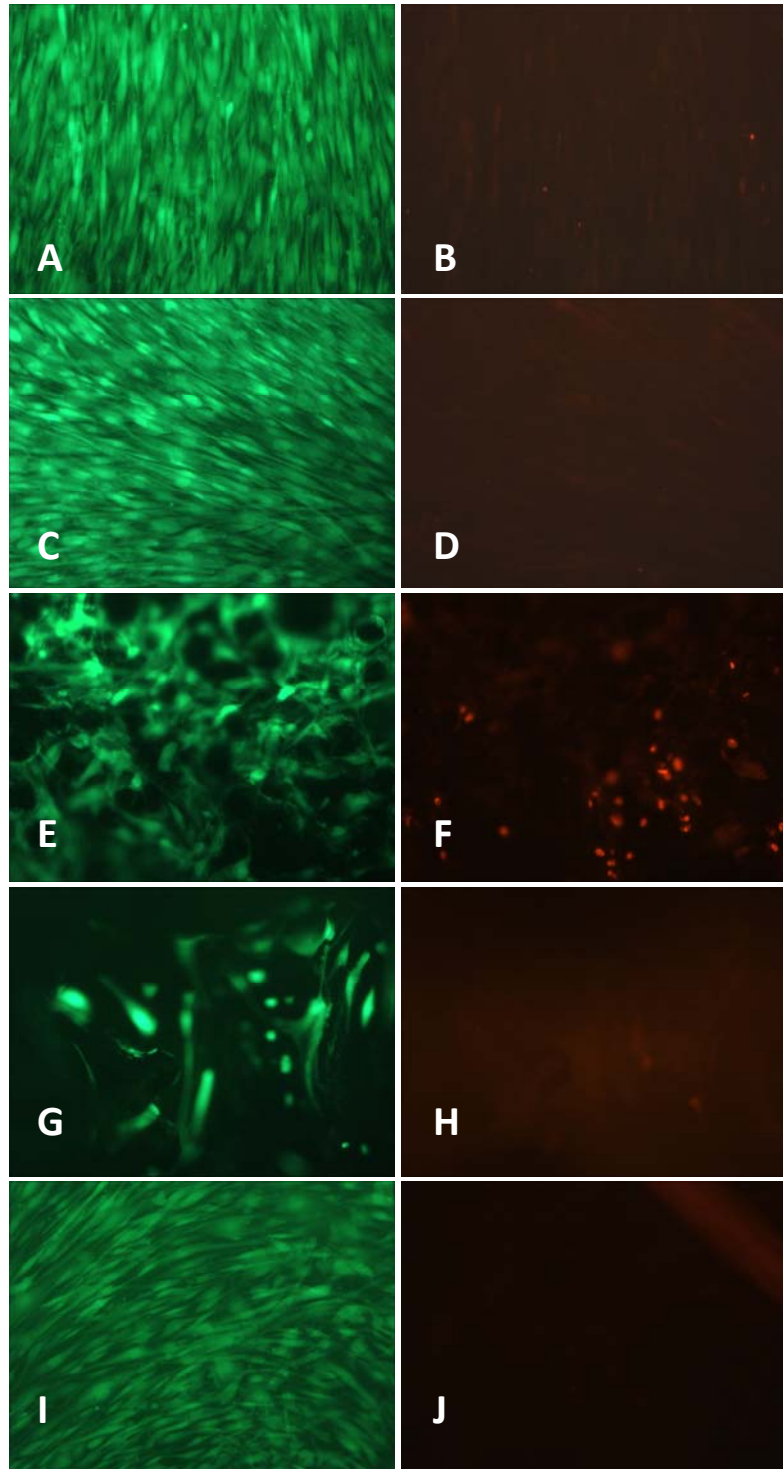
Figure 13: LIVE/DEAD® staining images of NHDF-Neo cells on the top layer of seeded scaffolds; commercial polished: A) living cells, B) dead cells; EBM polished: C) living cells, D) dead cells; EBM unpolished: E) living cells, F) dead cells; EBM porous: G) living cells, H) dead cells; coverslips: I) living cells, J) dead cells.
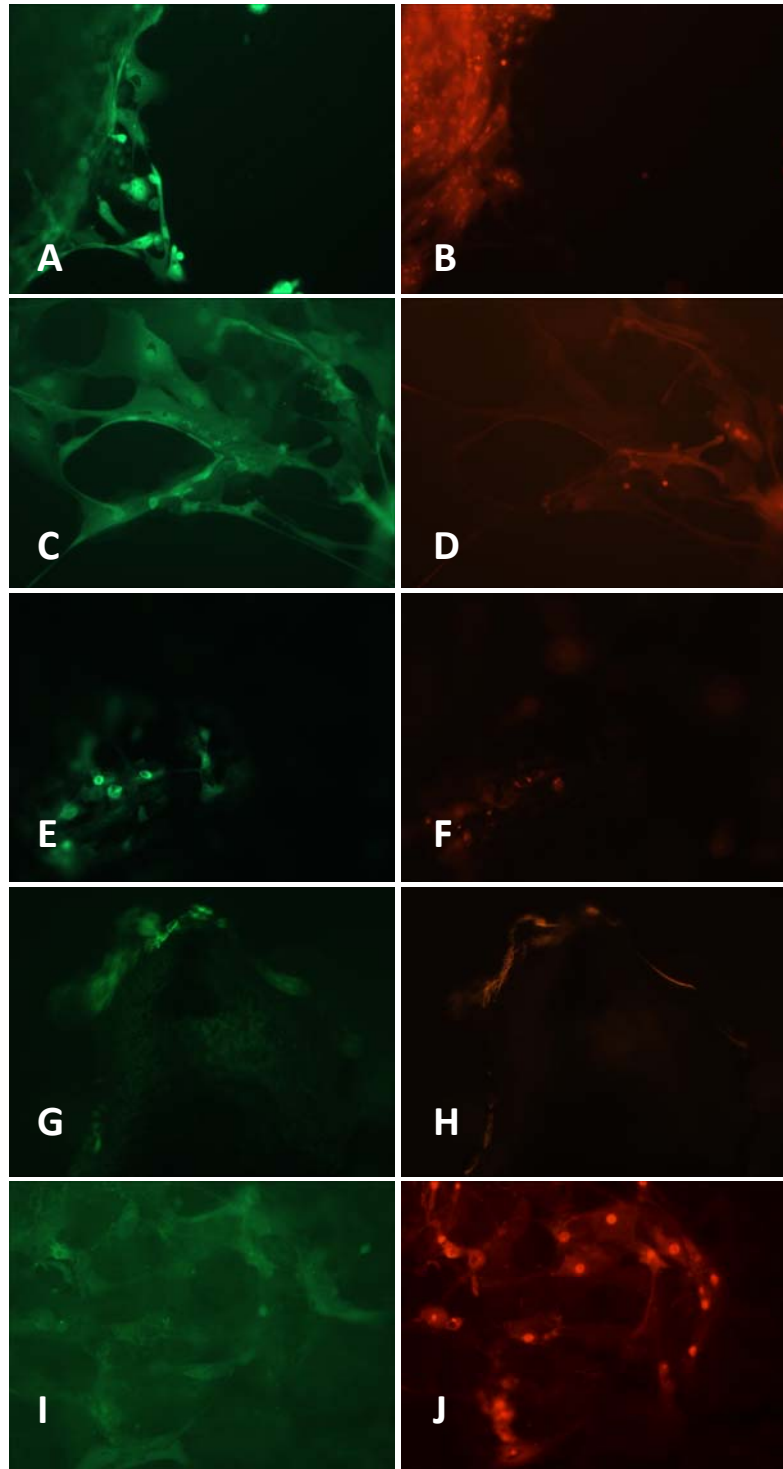
Figure 14: LIVE/DEAD® staining images of NHEK cells on the top layer of seeded scaffolds; commercial polished: A) living cells, B) dead cells; EBM polished: C) living cells, D) dead cells; EBM unpolished: E) living cells, F) dead cells; EBM porous: G) living cells, H) dead cells; coverslips: I) living cells, J) dead cells.

3.4 Discussion

Transdermal, osseointegrated implants breach the skin and create an environment susceptible to bacterial infection. Such infections could negatively impact the outcome of the surgical procedure and you place the patient at risk (Pendegrass et al., 2006a). Skin and subcutaneous ongrowth onto a metal implant could decrease the host susceptibility to these bacterial infections.

In this study, the cellular response of skin and subcutaneous cells to several Ti6Al4V surfaces were compared. These surfaces are similar to those that may be part of freeform transdermal osseointegrated implants. We compared polished, unpolished, and porous EBM surfaces to two control groups: polished glass and polished commercial Ti6Al4V surfaces. Cell survival and proliferation was better for all polished surfaces than for the unpolished and porous EBM surfaces, but living cells were visible on all surface types. The results of this study are in agreement with previous reports where skin proliferation was enhanced on smooth surfaces compared to rough surfaces (Kunzler et al., 2007). The polished commercial and EBM surfaces had similar surface roughness and no difference in cellular proliferation between these surfaces was identified, confirming that EBM-processing does not decrease the biocompatibility of Ti6Al4V implants.

Both dermal and epidermal skin cells play important roles in skin physiology. The epidermal skin layer functions as an effective barrier to microorganisms that could lead to infection (Fuchs et al., 2002). The dermal layer is responsible for the mechanical stability of skin (Boyce et al., 2002). Together, these two cell types prevent contaminants from entering the body. Epidermal cells consist mainly of keratinocytes and dermal cells include fibroblasts. We therefore investigated the

viability and proliferation of both keratinocytes and fibroblasts.

Optimization of the skin/implant surface is not a novel dilemma; however, many of the possible solutions have come with their own downfalls. Natural polymers, including small intestinal submucosa, acellular dermis, cadaveric fascia, bladder acellular matrix graft, and amniotic membrane, have been investigated for their ability to successfully host both dermal and epidermal cells (Hodde, 2002). While all of these polymers have exhibited rapid cell response with the ability to restore functional soft tissue their shortcomings include inappropriate or incomplete tissue remodeling, risk of disease transfer, failure due to poor quality of the tissue source, and interference with tissue healing due to antiangiogenic agents and antiinflammatory properties (Prasertsung et al., 2008; Seo et al., 2007; Xie et al., 2007). Some of these scaffold types also require extensive processing methods in order to harvest the material for use.

Keratinocytes were shown to proliferate when in contact with titanium alloy Ti6Al4V (Pendegrass et al., 2008a), and fibroblasts on NiTi (Ponsonnet et al., 2003), steel (Richards, 1996), commercially pure Ti (Ponsonnet et al., 2003; Richards, 1996), and Ti6Al4V (Pendegrass et al., 2008a; Ponsonnet et al., 2003). Dermal cells survived exposure to glass (Puck et al., 1957; Bitar et al., 2004), titanium (An et al., 2009; Meredith et al., 2007), biodegradable meshes (Cooper et al., 1991), hyaluronan-based biomaterials (Tonello et al., 2003), polyetheretherketone ([PEEK], Morrison et al., 1995), cell culture plastic ([TCPS], Beumer et al., 1993), and a composite soft poly (ethylene oxide-terephthalate (PEO)) and hard poly (butylene terephthalate (PBT)) with 70% porosity (Xiao et al., 1999). Natural protrusions through the skin such as teeth and deer antlers have been described and it was suggested that they could serve and a template for the design of transdermal implants

(Boyce et al., 2002). The inherent properties of the gum and the skin at the site of antler protrusion, however, may differ from the properties of the skin at limb-implant interfaces. Dermal and epidermal cells at the skin/implant interface have also shown acceptable survival after daily topical administration of pexiganan acetate (MSI-78) antimicrobial (Chou et al., 2010) and topical cationic steroid antimicrobial-13 [CSA-13], (Williams et al., 2010). A sealed skin/implant interface would likely be a preferable method for protection against infection compared to the sustained administration of antimicrobial medications.

Cell proliferation was assessed at two and seven days with alamarBlue® and compared to negative control wells. The alamarBlue® reagent was collected after a discernable change in hue was visible in one or more wells with cells present. The NHEK seven-day alamarBlue® reagent collection time was extended due to the slow reduction of cells, which was likely due to cell transformation into squamous cells that were no longer proliferating. This most likely explains why the rate of reduction of alamarBlue® decreased from day two to seven for the NHEK cells on all scaffold types. Dermal cells had an increase in alamarBlue® reduction from day two to seven, indicating an increased number of living cells present on scaffold surfaces. Overall, cells in contact with the commercial polished and EBM polished surfaces had greater proliferation rates compared to the unpolished and porous surfaces. Images of the cells on all surfaces were acquired to confirm the results of the metabolic assay.

The LIVE/DEAD® staining assay provides visibility of cells and distinction between cell status by staining the entire cytoplasm in live cells with calcein and EthD-1 staining the nuclei for dead cells. Using red and green fluorescence microscopes, live cells appear green with a visible

morphology and dead cells appear as small red spots. For dermal cells all scaffolds showed live cells with very few dead cells present. There were less living cells visible and a greater number of dead cells on scaffold surfaces because of the epidermal cell differentiation. Imaging the EBM porous scaffolds was difficult due to their three-dimensional design, and only the cells living on the top surface of the scaffolds were visible, potentially leading to an under estimation of the live cell count. Additional limitations of this study include the use of dermal fibroblasts from a single donor. Previous studies have shown that donor-to-donor variability has been shown to affect cell properties (Schneider et al., 2005).

Similarly to the results presented here, keratinocyte and fibroblast proliferation were influenced by surface roughness and topography (Gordon et al., 2006; Kunzler et al., 2007). Cells grown on polished discs were more confluent and more dividing cells were visible than cells grown on surfaces with greater roughness profiles. Cell morphology indicative of cell proliferation was observed in several studies of titanium surfaces with median surface roughness ranging from 0.030 to 0.935 μm (Pendegrass et al., 2008b) for keratinocytes and 0.030 to 5.9 μm (Kunzler et al., 2007; Pendegrass et al., 2008b; Ponsonnet et al., 2003) for fibroblasts. The average surface roughness of smooth scaffolds seeded in this study were 0.27, 0.32, 0.06 μm, for commercial polished, EBM polished, and glass coverslips, respectively, which is within the range of surface roughness of surfaces in the aforementioned studies. The EBM unpolished and porous scaffolds had average roughness values of 34.84 and 22.01 μm, respectively. These values are larger than the scaffolds used in previous reports.

Based on the results of this study, we concluded that surfaces with lower surface roughness

values should lead to acceptable dermal and epidermal cell survival and proliferation. Pores with diameters less than 40 μm have been shown as unable to successfully host dermal cells (von Recum, 1984). Further *in vitro* research is needed, but success has been seen with fibroblast migration into implanted flanges with pores 0.7 mm in diameter (Pendegrass et al., 2006a) as well as pylon surfaces with pores ranging from 30 to 250 μm in diameter (Pitkin et al., 2006). However, in the latter experiment, the attachment of dermal fibroblasts occurred randomly and was attributed to the variation in pore sizes. The flanged implants in the study contained 1000 μm pores and had better dermal ingrowth. These results indicate that there is likely an optimal range of pore diameters for successful dermal and epidermal cell migration and growth that still remains to be determined.

3.5 Conclusion

Titanium alloy discs were fabricated with various surface topographies and seeded with human keratinocytes and dermal fibroblasts. The proliferation rate and viability of the cells were assessed and compared to commercially produced titanium alloy discs and glass coverslips. There was no statistical difference in proliferation rates of cells on commercial and the EBM produced discs. The proliferation rates of the discs with lower surface roughness values were greater which is indicative of the preference of these cell types to smooth surfaces. The result of this study shows that EBM is an acceptable option for fabricating transdermal osseointegrated implants. It is also shown from this study that a surface with lower roughness may be more successful at promoting dermal fibroblast and keratinocyte cellular proliferation.

4.0 NHDF-NEO AND NHEK RESPONSE TO ETCHED EBM TITANIUM

4.1 Introduction

The surface characteristics of implanted devices may influence the biological response. Surface modifications can improve mechanical, chemical, and physical properties. When implanting a device within the biological environment it is critical to ensure that the device will not be rejected by the body and furthermore will be accepted. To enhance this acceptance, a coating can be applied to the implant or the surface can be altered with texturing. The surface modification can promote osseointegration for both dental and orthopedic implants. Surface modifications can be categorized into two areas; convex and concave (Oshida, 2007). Surface convex texturing is when particles are added to the surface with a depositing technique, such as chemical vapor deposition (CVD), physical vapor deposition (PVD), and plasma spraying. Surface concave texturing is when material is removed by techniques such as chemical or electrochemical action, or mechanical indentations, such as sand-blasting, shot peening, and laser peening.

There are several coatings that have been used for implants, including hydroxyapatite (HA), calcium-phosphate (Ca-P), and titanium nitride. Coatings have been shown to improve initial ingrowth over scaffolds without coatings; however, problems with coated implants include degradation or wear of the coating and the cost to coat the implant (Weast et al., 2000). HA is the primary mineral component of bone and is stable, inert, and biocompatible. It is often used as a coating and has been shown, in some instances, to improve integration at the bone/implant surface

resulting in more rapid osseointegration, which may lead to earlier and increased implant stability (Blalock, et al, 2007). Achieving a HA coating is possible with several methods including plasma-spray, electrophoretic deposition, sputter coating, and sol-gel (Habibovic et al., 2002). The plasma-spraying method for applying a HA coating is the most popular method, but an even coating cannot be achieved on a porous material due a line-of-sight application technique.

The processing method and heat treatment determine the crystallinity of the HA coating and can also lead to the time frame in which the coating will break down within the biological environment (Blalock et al., 2007). There are two forms of HA; amorphous and crystalline. Amorphous HA promotes cell growth and is quickly dissolved by the body. In contrast, crystalline HA is more stable *in vivo* and stimulates bone ingrowth. Plasma-sprayed HA has been shown to be approximately 65% crystalline. Crystalline structures can be formed by post-deposition heat treatments of amorphous coatings. The level of crystallinity from these treatments is determined by the amount of water vapor present, heat treatment temperature, and duration of treatment. The degree of crystallinity should be monitored so as to have the appropriate dissolution rate for the implant application. If the structure dissolves more quickly than the bone growth rate, then the bone will not have adequate time for ingrowth. This may cause the implant to loosen and may lead to implant failure.

Several studies have been conducted to test cell growth on HA surfaces. Most studies have found that coating the implant surface with HA has increased bone growth and interface attachment strength initially when compared to uncoated surfaces (Cook et al., 1991; Dalton et al., 1995; Oonishi et al., 1989; Stephenson et al., 1991). Stephenson et al. found that HA coated implants

would close larger gaps than non-coated implants, but that the un-coated implants resulted in denser bone on the surface of grooved implants after four weeks. Oonishi et al. used scanning electron microscopy (SEM) to show that the HA coated surfaces reduce the formation of connective tissue membranes between the beaded surface and bone to allow for strong bone fixation during the first few weeks after implantation (1989). In the early stage of implantation, fixation is an important focus in order to avoid implant loosening.

The spacing between the implant and the bone has been studied to determine if it affects the level of ingrowth that will occur. Some studies have been completed to determine the effect of this gap and the interaction effects with and without a HA coating. Dalton et al. tested interference gaps of 0.0, 0.5, 1.0, and 2.0 mm, for HA coated and uncoated implants with an *in vivo* study using dogs (1995). The results from push-out tests and histological analysis showed that mechanical attachment strength and bone ingrowth increased as time after implantation increased and interference gap decreased. In all but a few cases, the HA coating increased the interface attachment strength and the amount of bone ingrowth. This improvement was significant at interfacial gaps of 1.0 mm or less and at the shorter *in vivo* periods. The results of this study also indicate that the 2.0 mm interfacial gap may be the upper limit of the distance that bone is able to span in order to create strong fixation with an implant at early time periods. Another study, conducted by Kusakabe et al. showed that mesh implants coated with HA showed significantly greater bone ingrowth and push-out strength when compared to implants with beaded surfaces (2004). These surfaces were tested with canine hip stems with *in vivo* studies at six and twelve months implantation durations. Within three weeks of implantation, new bone had formed in the

bottom of the porous area, but the conventional beaded surface did not possess bone formation at the bottom. Growth of the trabecular bone creates a strong anchor for weight-bearing loads and at six and twelve months the smaller pores of the beaded surface inhibited the thickening of the trabecular bone. Nakashima et al. used a titanium arc spray technique for implant stability and then coated implants with HA in order to compare surface roughness and interfacial shear strength, along with the effects of HA coatings (1997). Histological results showed that HA coating enhanced bone ingrowth, but that the shear strength of the coating on smooth Titanium was the lowest of all the groups tested at a value of 5.38 MPa for twelve weeks of ingrowth. This indicates that it may be preferred to coat a rough surface with HA to get adequate shear strength.   A separate study found a shear strength of 64 MPa when apatite-coated plugs were tested *in vivo* (Geesink et al., 1987).

A Ca-P coating has been shown in research to accelerate bone formation around the implant (Rivero et al., 1988; Shirkhanzadeh, 1991). Rivero et al. implanted porous titanium implants with Ca-P coatings in dogs and tested them at one, two, four, and six weeks (1988). At four weeks, but no other time span, the mean shear strength was 24% greater for the Ca-P coated implant in comparison to the control. However, there was no significant ingrowth volume difference seen at any time period for the treated implants.

Concave surface modifications of implants, include chemical etching, which removes the top surface of the implant, may improve the biocompatibility and ingrowth surface characteristics of the implant.   Klokkevold et al. showed that chemical etching on titanium surfaces may promote osseointegration (1996). When the titanium implant is cast, which is a popular method of producing some orthopedic and dental implants, an alpha-case is formed on approximately the top 200 µm of

the part. This alpha case is formed from the reactivity of the Ti6Al4V with the investment materials.

This layer is a hard, brittle, reactive and thick oxide layer, which is not an ideal material form for

implants (Say et al., 2004). Chemical etching, sometimes referred to as pickling, is a method used to

remove this outer layer in order to produce a better surface for medical applications. Only a few

acids and alkaline solutions are able to be used on titanium implants because of the chemical

stability of titanium oxides. Hydrofluoric nitric acid (HF/HNO_3) is a commonly used etching chemical,

but the ratio of nitric acid to hydrofluoric acid must remain at 10:1 to reduce the absorption of

hydrogen which causes surface embrittlement (Brunette et al., 2001).   A mixture of HCl and H_2SO_4,

in equal volumes, has also been successfully used to chemically etch titanium and titanium alloys.

Martin et al. demonstrated that surface roughness and topography are both important in biological

performance of implanted materials (1995).

Surface preparations of titanium prior to biological implantation may transform the

chemical surface composition and increase the ability for cells to adhere and proliferate. Deligianni

et al. cultured human bone marrow cells on polished titanium discs with three mean (Ra) ± standard

deviation surface roughness values; 0.320 ± 0.065, 0.490 ± 0.095 and 0.874 ± 0.185 µm (2001). They

found that the number of cells increased as the surface roughness increased, which is consistent

with the results of *in vivo* studies (Buser et al., 1991; Goldberg et al., 1999). However, some *in vitro*

studies showed the opposite results; with human and mouse osteoblastic cells proliferating less

when in contact with rougher Ti6Al4V surfaces (Anselme et al., 2000; Martin et al., 1995). While

there are many studies that have analyzed bone response to various types of titanium surfaces;

both *in vitro* and *in vivo*, there are fewer studies analyzing skin response (Pendegrass et al., 2008b;

Ponsonnet et al., 2003).

From the results in our previous studies it was found that skin cells showed proliferation on EBM produced surfaces and levels were greater for smooth surface textures when compared to a rough surface textures. This is confirmed by other studies of skin cell response on titanium (Gordon et al., 2006; Kunzler et al., 2007). The custom transcutaneous osseointegrated titanium implants fabricated with EBM have a rough as-processed surface. In order to promote skin attachment at the skin/implant interface a method to smooth these surfaces was investigated. Since the implants have complex geometries with small pores, traditional finishing techniques cannot be used. For this research, chemical etching was used to reduce the surface roughness by remove the titanium powder sintered to the outer layer of the discs, which can be seen in Figure 5C. Porous scaffolds were fabricated using EBM, chemically etched with HF/HNO_3 for either one or two minutes, and compared to non-etched scaffolds. Dermal fibroblasts and epidermal cell were seeded onto the scaffold surfaces and cultured for seven days. Cell morphology was assessed with scanning electron microscopy (SEM) imaging, proliferation was assessed with alamarBlue®, and viability was assessed with LIVE/DEAD® staining.

4.2 Materials and Methods

4.2.1 Scaffold Preparation

Nine Ti6Al4V disc-shaped scaffolds (10 mm diameter, 4 mm height) were fabricated with EBM for an initial pilot study of the etching time determination. Each disc was blasted for twenty seconds with titanium powder from the build chamber to remove loose and lightly sintered powder.

The scaffolds were porous, open mesh structures with a hexagonal unit cell design, with an average pore size of approximately 560 μm. Each scaffold was etched in 150 mL hydrofluoric-nitric acid solution (2% HF/ 30% HNO$_3$) for either 30 (n=1), 60 (n=3), 90 (n=2), or 120 (n=3) seconds.

For cell analysis, Ti6Al4V porous scaffolds (10 mm diameter, 4 mm height) were designed, fabricated, and blasted using the same procedure as the scaffolds in the etching pilot study. For each of two experiments there were three groups of seven scaffolds; non-etched with the as-processed surface (NE), etched for one minute (E1), and etched for two minutes (E2). The etching solution (2700 mL) consisted of 60 mL HF and 600 mL HNO$_3$. Scaffolds were etched (n=2) in 300 mL etching solution for their specified duration, washed six times with de-ionized water, and dried with nitrogen. Scaffolds were then treated with an enzymatic foam spray (Prepzyme® X.F. eXtreme Foam, Ruhof Corporation, Mineola, NY), ultrasonically washed, rinsed with distilled water, dried with pressurized air, and steam sterilized in sealed pouches. Tissue culture treated polystyrene plates (24-well, Nunclon™ Δ Surface, Thermo Fisher Scientific Inc., Rochester, NY) were used as control surfaces (TCP).

4.2.2 Cell preparation

Neonatal normal human dermal fibroblasts (NHDF-Neo) from a single donor (race unknown), (Lot #: 7F3367), were purchased from Lonza (Walkersville, MD) and cryogenically preserved. Prior to this experiment, 200,000 cells were thawed and seeded in a T-75 flask with FGM®-2 culture medium (Nunc, Thermo Fisher Scientific, Rochester, NY) and incubated within a

37°C, 5% CO_2 environment. After four days of culture, cells were approximately 80% confluent. The growth medium was aspirated and the cells were washed twice with 10 mL of PBS and then aspirated. Cells were released from the flask surface using 3 mL trypsin-EDTA for two minutes, 6 mL trypsin neutralizing solution (TNS) was added, and cells were transferred to a 15 mL conical tube. Cells were pelleted by centrifugation at 70 x *g* for five minutes, supernatant was aspirated, and cells were resuspended in 1.0 mL of FGM®-2 medium. The cell solution was mixed with a pipette to ensure a consistent mixture prior to adding 12 mL to each side of the hemacytometer. Using a Leica microscope (Leica DMIL, Deerfield, IL) cells were counted. This cell count was used to estimate the total number of cells within the mixture.

Normal human epidermal keratinocytes (NHEK) pooled from three Caucasian donors, (Lot #: 1F1651) were purchased from Lonza. For this experiment, the cells were thawed from cryogenic preservation and 500,000 cells were cultured in KGM®-2 medium (Lonza, Walkersville, MD), in a T-75 flask for one week in a 37°C, 5% CO_2 environment. NHEK cell were trypsinized and counted using the same procedure as the NHDF-Neo cells.

4.2.3 Seeding the Chemically Etched Scaffolds

All scaffolds were placed into a 24-well, non-tissue culture treated plate (Becton Dickinson & Company, Franklin Lakes, NJ). For the first experiment, NHDF-Neo (passage 3), were seeded at a density of 1×10^4 cells / 50 μL on five scaffolds for each unique type with two "no-cell" negative controls. Treated culture plates served as a positive control (24-well, Nunclon™ Δ, Thermo Fisher Scientific Inc., Rochester, NY). Cell solution (50 μL) was slowly added to the top surface of scaffolds

and the center of the well-plate surface and incubated for one hour to allow the cells to adhere to the surface before alamarBlue® (Invitrogen, Eugene, Oregon) solution was added to all wells.

The procedure for the second experiment was identical, except that scaffolds and well-plate surfaces were seeded with NHEK cells (passage two) at a density of 1.5 x 10^4 cells / 50 μL.

4.2.4 Cell Proliferation

Proliferation was analyzed with alamarBlue® (% reduction) at three time points: zero, two, and seven days. Pre-warmed growth medium containing alamarBlue® at 10% (v/v) was added to each well at 1 mL volume. The solution was incubated until a discernable change in hue for one or more wells was observed and aspirated into snap cap tubes. For the NHDF-Neo cells the incubation period was five hours for all time points. For the NHEK cells the incubation period was 5.5, 5.5, and 7 hours for the zero, two, and seven day time points, respectively. Each sample was collected in triplicate (200 μL) into a 96-well plate and centrifugation at 400 x g for three minutes was used to remove air bubbles. Absorbance was measured at 570 nm and 600 nm wavelengths using a microplate reader (GENios; Tecan Group, Maennedorf, Switzerland). Negative controls (no-cell scaffolds) were processed identically to cell wells. Proliferation absorption readings were analyzed in triplicate. Results were analyzed in JMP 8.0 (SAS Institute, Cary, NC) using Student's t-test with P < 0.05 considered significant.

4.2.5 Cell Viability

LIVE/DEAD®, a fluorescence-based assay, was used to analyze cell viability at day nine. Scaffolds were washed twice with PBS (Fisher Scientific, Fair Lawn, NJ) and then staining solution (50 µL) containing 1 µL calcein AM, 4 µL EthD-1, and 2 mL PBS was added to all TCP wells. For the titanium scaffolds, 50 µL staining solution was added to a culture plate lid where the circles meet tangentially. Each of four scaffolds (three with cells and one without cells) per type was carefully inverted onto the solution (Figure 16). Cells were incubated for fifteen minutes and images acquired using a Leica DMIL microscope (10x magnification) and QCapture camera (Qimaging Micropublisher imaging System, Canada).
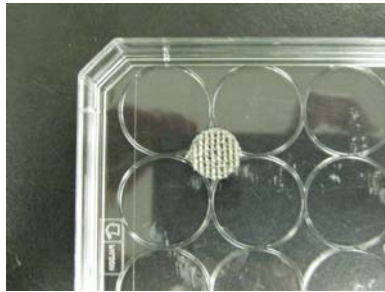
Figure 15: Photograph of a scaffold inverted on a culture plate lid for microscope imaging of cells using a LIVE/DEAD® staining assay.

4.2.6 Scanning electron microscopy

On day eight, two titanium discs containing cells for each type were washed three times in 0.1M Na cacodylate buffer (pH 7.4) at room temperature (RT), followed by flooding with a fixative solution of 3% glutaraldehyde in 0.1M Na cacodylate buffer at RT (pH 7.4). Scaffolds remained under a sterile hood at room temperature for 1.5 hours before placing at 4°C until processed for

SEM. Scaffolds were processed using 10 minute changes in all solutions on ice: three washes with cold 0.1M Na cacodylate, pH 7.4; dehydration in a graded ethanol series of cold 30%, 50%, 70%, 95% and 100% EtOH, warming to room temperature and followed by two additional room temperature changes of 100% ethanol. Scaffolds were immediately prepared with critical point drying in liquid CO_2 (Tousimis Samdri-795, Tousimis Research, Rockville, MD) and mounted on stubs using carbon tape (Figure 16). Samples were held in the desiccator until coated using a Hummer 6.2 sputtering system with approximately 50Å Au/Pd (Anatech U.S.A., Union City, CA). Samples were viewed with an accelerating voltage of 10kV using a JEOL JSM- 5900LV (JEOL U.S.A., Peabody MA). A disc that was not etched, nor part of the experiment, was washed twice for ten minutes each with acetone, sonicated and air dried. It was imaged with SEM for comparison purposes.
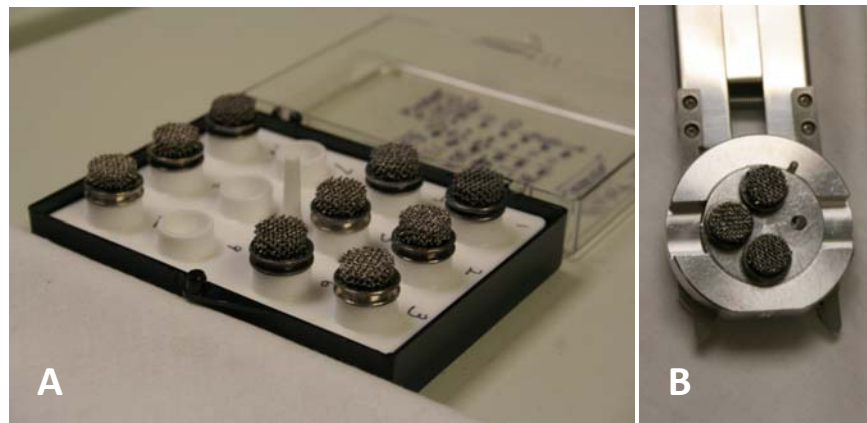
Figure 16: Photographs of A) scaffolds mounted on to stubs in preparation for SEM imaging, B) Mounted scaffolds in the SEM holder.

4.2.7 Scaffold analysis

Initial surface roughness, strut size, and pore size were measured using a Hirox KH-7700 microscope (Hirox-USA, Inc., River Edge, NJ). From a 3D topographical image of the strut surface

(350x magnification), the height versus distance data was used to determine the approximate surface roughness (Figure 17). Four areas of the scaffold (n=4) were analyzed for surface roughness on the strut surface. Pore diameter and strut width were taken at two randomly selected areas of four scaffolds per type using a Hirox KH-7700 microscope (70x magnification). The weight of each scaffold was measured using an Adventurer® precision balance (Ohaus Corp., Pine Brook, NJ). Surface roughness of the tissue culture treated plate surface was measured at eight locations from one well using a surface profilometer (Mitutoyo Surftest 212, Mitutoyo U.S.A., Aurora, IL).
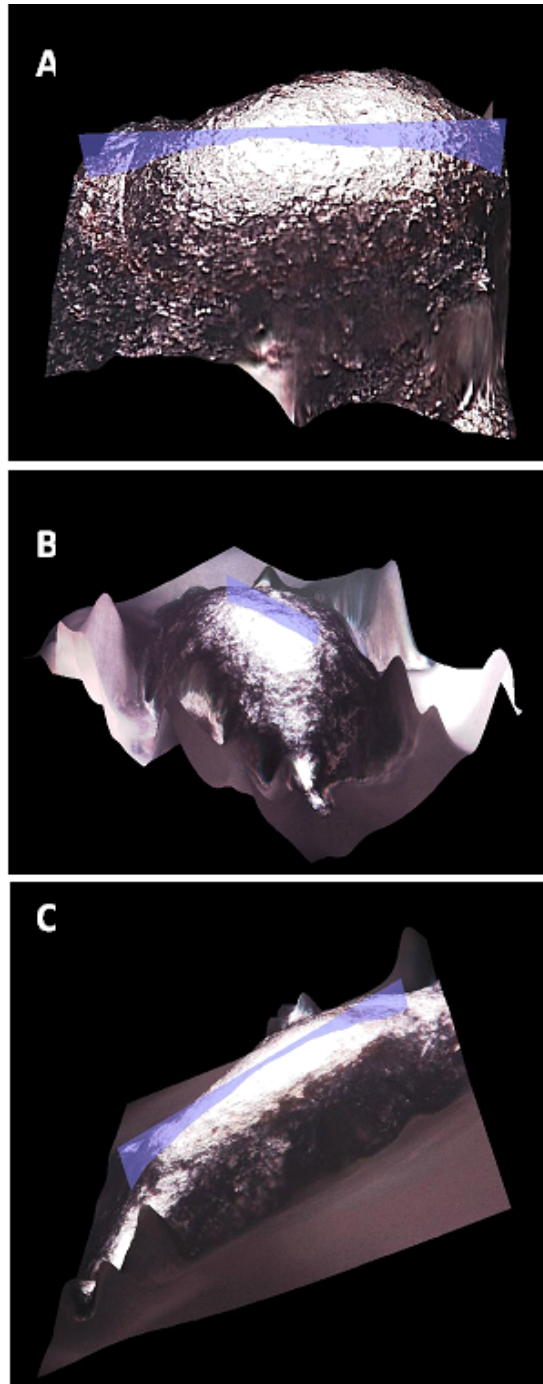
Figure 17: A 3D topographical image of the strut surface (350x magnification), then the height versus distance data was used to determine the approximate surface roughness, A) non-etched disc, B) disc etched for 1 minutes, C) disc etched for 2 minutes.

4.3 Results

4.3.1 Cell Proliferation on Chemically Etched Scaffolds

On day seven, the mean ± SEM percent reduction (per hour of incubation) of alamarBlue® by NHDF-Neo cells was 5.32 ± 1.45, 3.56 ± 1.36, 5.71 ± 0.76, and 12.34 ± 2.76 for NE, E1, E2, and TCP, respectively (Figure 18). All *P*–values for the student's t-test are listed in Table 3. For all time points, the greatest reduction was by cells on TCP surfaces. The reduction for cells, on day seven, on non-etched discs and discs etched for two minutes was not statistically different, but was statistically greater than for the discs etched for one minute.

For all of the time points analyzed, the NHEK reduction of alamarBlue® (per hour of incubation) was greatest for the TCP surfaces. On day two, both etched surface experimental groups had statistically equivalent average reductions and were statistically greater than the non-etched surfaces. The mean ± SEM percent reduction (per hour of incubation) of alamarBlue® for NHEK cells on day two was 2.17 ± 0.06, 2.67 ± 0.09, 2.72 ± 0.18, and 3.90 ± 0.26 for NE, E1, E2, and TCP, respectively (Figure 19). All *P*–values for the student's t-test are listed in Table 4.
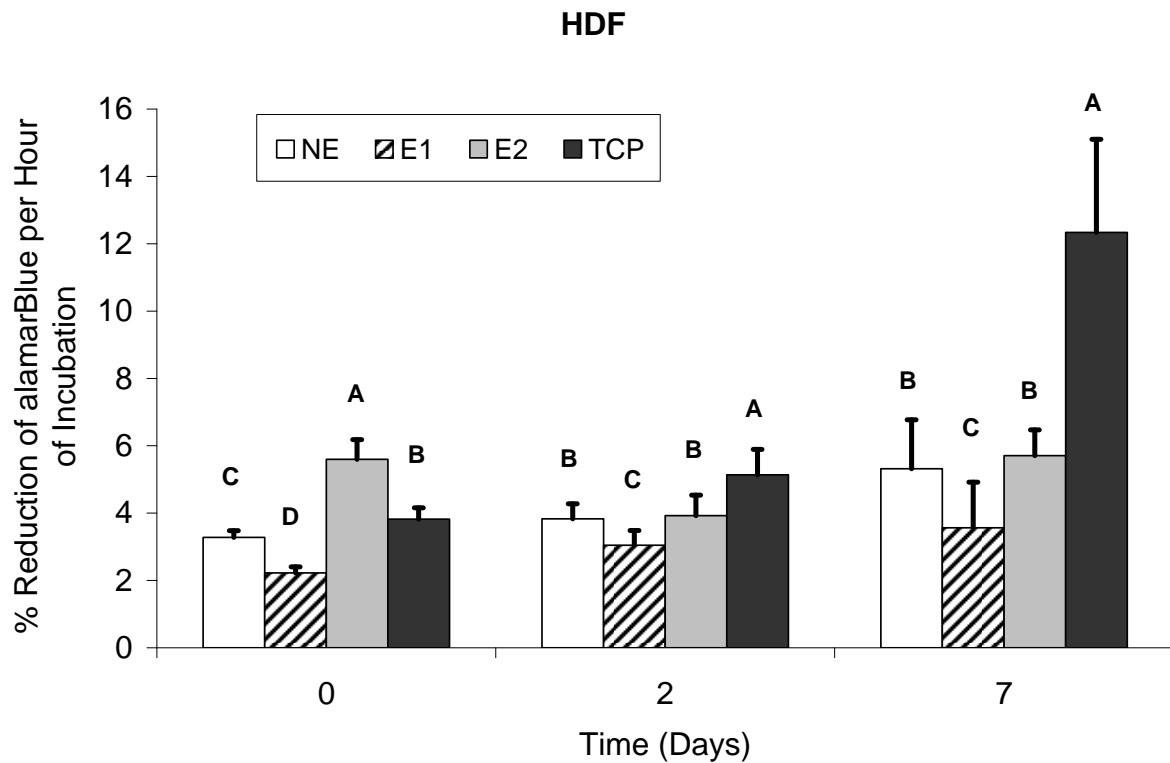
Figure 18: Mean % reduction of alamarBlue® (per hour of incubation) for NHDF-Neo cells on scaffolds; NE= non-etched EBM produced porous discs, E1= EBM porous discs etched for 1 minute in HF+HNO3, E2= EBM porous discs etched for 2 minutes in HF+HNO3, and TCP = tissue culture plate.

Table 3: Statistical p-values for NHDF-Neo cells seeded onto scaffolds, NE= not etched, E1= etched for 1 minute in HF+HNO3, E2= etched for 2 minutes in HF+HNO3, and TCP= tissue culture treated plate (24-well).

		p-Value		
Group	Comparison Group	day 0	day 2	day 7
E2	E1	<.001	<.001	<.001
E2	NE	<.001	0.349	0.157
E2	TCP	<.001	<.001	<.001
TCP	E1	<.001	<.001	<.001
NE	E1	<.001	<.001	<.001
TCP	NE	<.001	<.001	<.001
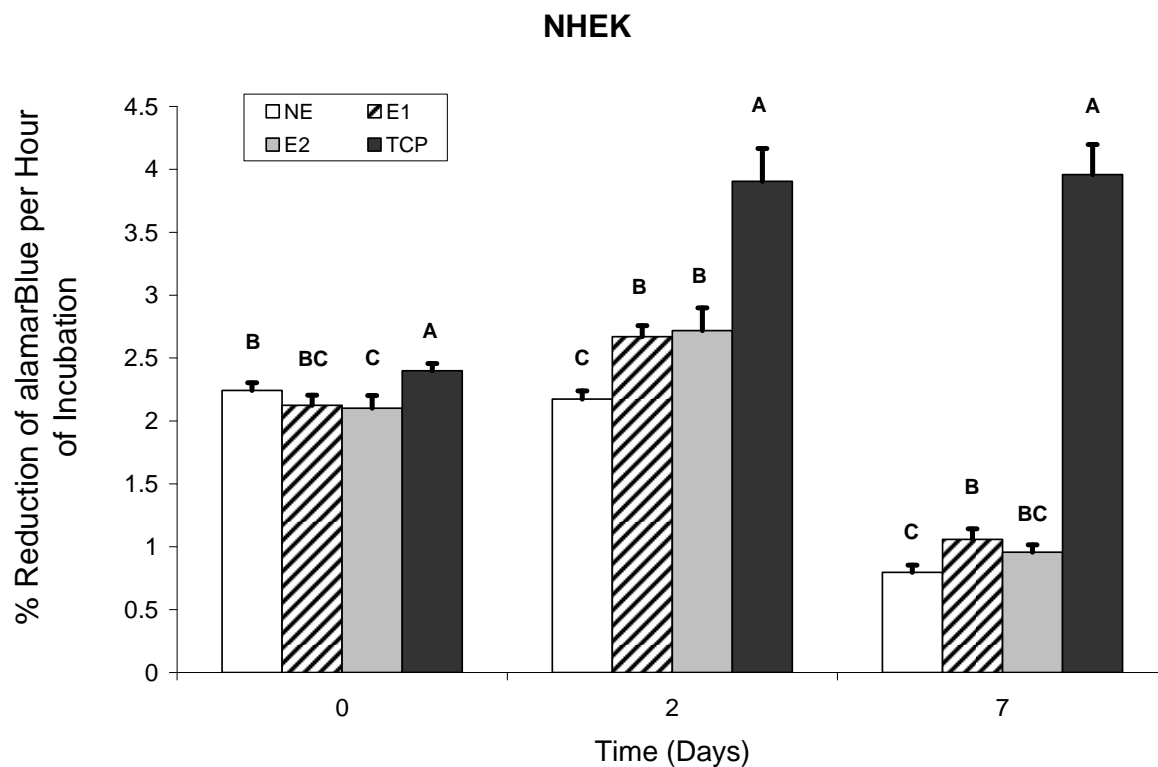
NHEK

Figure 19: Mean % reduction of alamarBlue® (per hour of incubation) for NHEK cells on scaffolds; NE= non-etched EBM produced porous discs, E1= EBM porous discs etched for 1 minute in HF+HNO3, E2= EBM porous discs etched for 2 minutes in HF+HNO3, and TCP = tissue culture plate. Bars represent standard error. Bars within the same time point not connected by the same letter are significantly different.

Table 4: Statistical p-values for NHEK cells seeded onto scaffolds, NE= not etched, E1= etched for 1 minute in HF+HNO3, E2= etched for 2 minutes in HF+HNO3, and TCP= tissue culture treated plate (24-well).

		p-Value		
Group	Comparison Group	day 0	day 2	day 7
TCP	E2	<.001	<.001	<.001
TCP	E1	<.001	<.001	<.001
TCP	NE	0.010	<.001	<.001
NE	E2	0.020	<.001	0.119
NE	E1	0.051	<.001	0.012
E1	E2	0.695	0.706	0.320

4.3.2 Cell Viability on Chemically Etched Scaffolds

Live/Dead imaging of NHDF-Neo seeded surfaces showed visible live cells on all surface types (Figure 20). Titanium discs contained living cells that appeared to be in clusters in a grid-like pattern, consistent with the pattern of the top layer of the mesh struts. For both the NE and E1 discs, two of the three imaged discs contained significant living cells within the visible areas and a few dead cells. All three of the E2 discs imaged contained significant living NHDF-Neo cells. The TCP control surfaces were more easily imaged due to the 2-dimensional (2D) surface. A confluent layer of living cells was visible within the seeded area on all TCP wells.

Living NHEK cells were present on all seeded surfaces (Figure 21), with substantially fewer living NHEK cells present on the titanium discs than the TCP control wells. The number of living cells on NE discs appeared to be fewer than those on E1 and E2 discs. Overall E1 discs appeared to have the most live cells of all the titanium discs, with one disc containing visible cell clusters and another disc showing cells with a long-shaped structure. Four of the five TCP wells seeded contained many live cells and two of these wells contained clusters of cobblestone-like cell areas. All surfaces had visible dead cells present, with TCP wells containing the fewest number and NE containing the most.
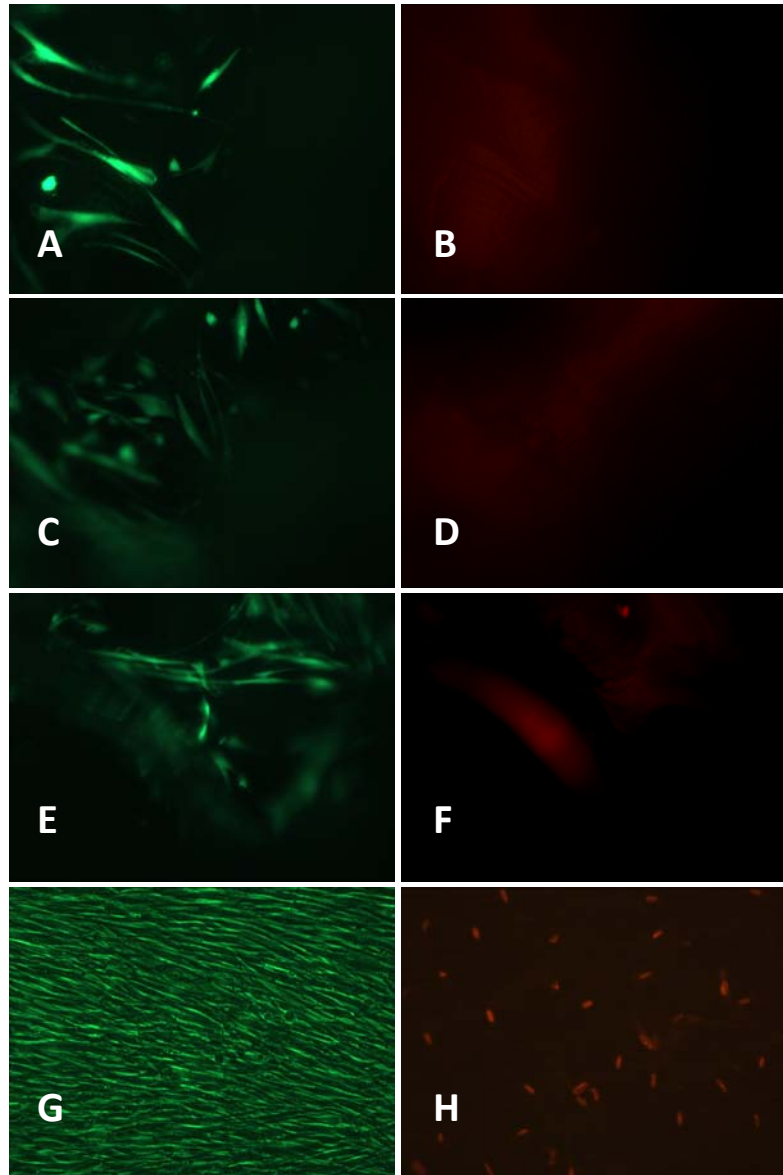
Figure 20: LIVE/DEAD® staining images (10x magnification) of NHDF-Neo cells on the top layer of seeded scaffolds; Non-etched scaffolds: A) living cells, B) dead cells; scaffolds etched for 1 minute in HF/HNO$_3$: C) living cells, D) dead cells; scaffolds etched for 2 minutes in HF/HNO$_3$: E) living cells, F) dead cells; tissue culture treated plate surface: G) living cells, H) dead cells.
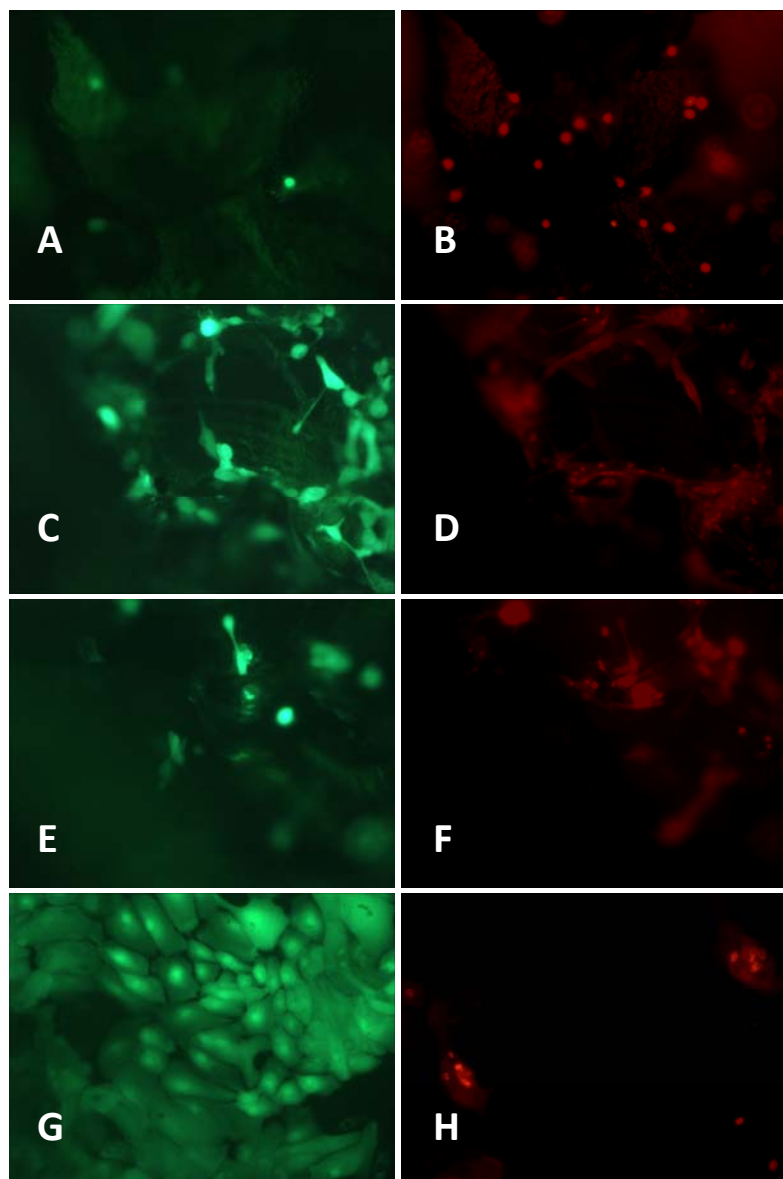
Figure 21: LIVE/DEAD® staining images (10x magnification) of NHEK cells on the top layer of seeded scaffolds; Non-etched scaffolds: A) living cells, B) dead cells; scaffolds etched for 1 minute in HF/HNO$_3$: C) living cells, D) dead cells; scaffolds etched for 2 minutes in HF/HNO$_3$: E) living cells, F) dead cells; tissue culture treated plate surface: G) living cells, H) dead cells.

4.3.3 Cell Morphology

A non-etched scaffold was analyzed with SEM for comparison. It showed only a few areas of flaking (Figure 22) on the surface which can then be excluded from the seeded discs as any form of cellular matrix or cellular debris and rather as part of the scaffold surface. Images of the top surface of the scaffolds were captured to illustrate changes in pore diameter and strut width with the various etching durations (Figure 23).

NHDF-Neo cells were visible on all surfaces (Figure 24). For the NE scaffolds cells were mainly visible on the top surface and were spindle-shaped. The cells stretched from one titanium powder particle to another (Figure 24A&D). E1 scaffolds appeared to have fewer cells at the top and lower levels, but cells were visible on the scaffolds (Figure 24B&E). Cells were visible on E2 scaffolds, but were most prevalent on the lower surfaces and less numerous on the top surface of the discs (Figure 24C&F).

NHEK cells were visible on all scaffolds (Figure 25), but fewer cells were found on the NE and E1 scaffolds than on the E2 scaffolds. The E2 scaffolds appeared to have more cells on the struts below the top surface than on the top surface (Figure 25C&F). NHEK cells were rounded in shape for both NE and E1 scaffold types, but a combination of rounded and spindle-shaped cells were observed on E2 scaffolds.
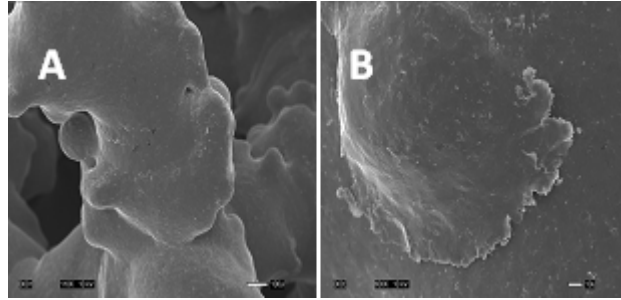
Figure 22: SEM micrographs of a Ti6Al4V disc that was not seeded with cells; A) low magnification, bar = 100μm, B) high magnification, bar = 10μm.
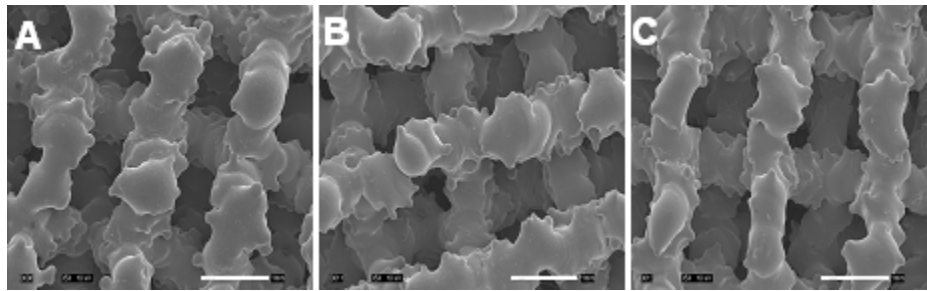
Figure 23: SEM micrographs of Ti6Al4V discs, A) non-etched, B) etched for 1 minute, C) etched for 2 minutes, showing visible differences in pore diameter and strut widths between scaffold types, bar = 1mm.
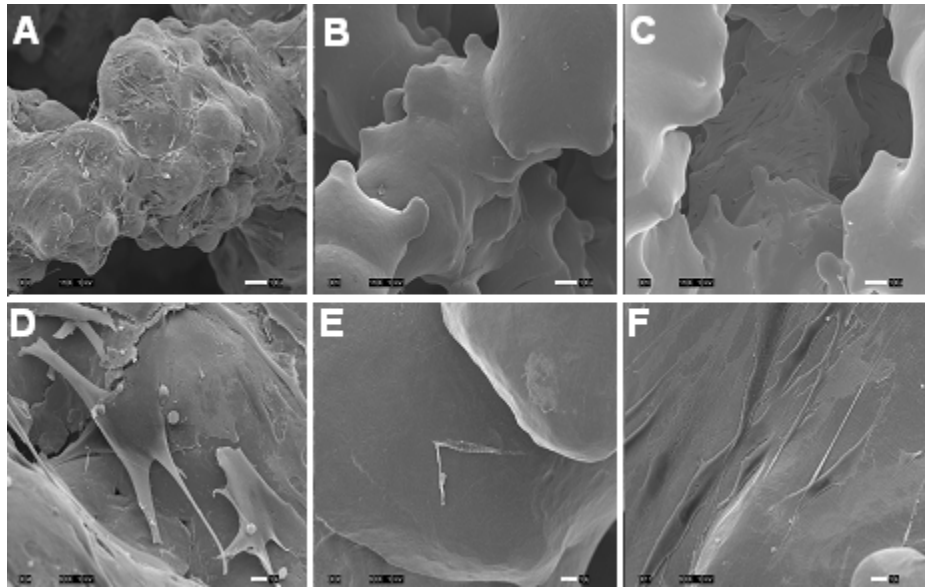
Figure 24: SEM micrographs of Ti6Al4V discs seeded with NHDF-Neo cultured for 8 days: NHDF-Neo on the surface of TI6Al4V scaffolds low magnification, (bar = 100μm): A) non-etched, B) etched 1 minute, C) etched for 2 minutes, high magnification (bar=10μm), showing cells on surfaces, D) non-etched, E) etched for 1 minute, F) etched for 2 minutes.
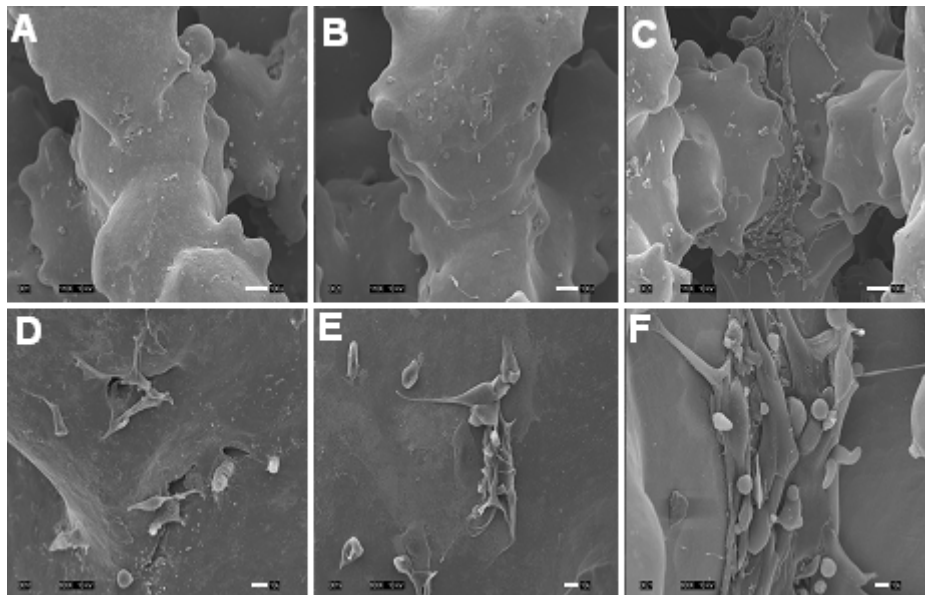
Figure 25: SEM micrographs of Ti6Al4V discs seeded with NHEK cultured for 8 days: NHEK on the surface of TI6Al4V scaffolds low magnification, (bar = 100μm): A) non-etched, B) etched 1 minute, C) etched for 2 minutes and high magnification (bar = 10μm), showing cells on surfaces, D) non-etched, E) etched for 1 minute, F) etched for 2 minutes.

4.3.4 Surface Analysis

For scaffolds used in the etching pilot study the strut width and pore diameter measurements before and after etching are given in Table 5. For the full-scale study, the mean ± standard deviation (SD) surface roughness (Ra) values for the NE, E1, E2, and TCP were approximately 22.01 ± 10.17, 15.06 ± 19.17, 12.46 ± 8.21, and 0.12 ± 0.03 μm, respectively. The average pore size (± SD) for NE, E1, and E2 scaffolds were 562.50 ± 74.40, 662.50 ± 74.40 and 743.75 ± 97.97 μm, respectively and the average strut width (± SD) for NE, E1, and E2 scaffolds were 707.15 ± 29.77, 384.18 ± 36.80 and 357.11 ± 39.26 μm, respectively. The average weight (± SD) for NE, E1, and E2 scaffolds were 0.46 ± 0.07, 0.41 ± 0.06, and 0.36 ± 0.04 grams, respectively, resulting in a 10% weight reduction after etching for one minute and a 22% weight reduction after two minutes of etching.

Table 5: Influence of chemical etching with HF/HNO$_3$ on pore size and strut width measurements for EBM processed Ti alloy scaffolds.

	pre-etched				post-etched			
	pore diameter		strut width		pore diameter		strut width	
HF/HNO$_3$ Etching Duration (seconds)	Mean (μm)	St dev (μm)	Mean (μm)	St dev (μm)	Mean (μm)	St dev (μm)	Mean (μm)	St dev (μm)
30	612.33	10.60	728.10	31.88	735.43	8.06	664.23	27.52
60	653.41	11.87	715.06	17.10	776.47	13.82	606.75	17.66
90	637.50	7.19	696.85	21.82	844.10	13.25	550.59	17.30
120	645.76	8.29	705.22	12.09	822.70	17.49	568.08	20.64

4.4 Discussion

Both dermal and epidermal cells are important in the function of skin (Alberts et al., 2008).

These two cell types have been studied *in vivo* and *in vitro* on various surfaces and surface topographies. Most research, including the previous study in this research, indicates that skin cells exhibit a preference for smooth surface textures.

Many materials are considered biocompatible and some may be able to promote skin growth; however, custom-designed implant fabrication with many of these materials is challenging or impossible. Furthermore, many biocompatible materials are not able to support the loads required in human lower limb prostheses. For these reasons, it is necessary that we investigate methods for improving the surface of metal implants produced with additive manufacturing processes, such as EBM in order to promote skin attachment.

In vivo studies have been performed to determine soft tissue attachment strength to various metal surfaces, such as sintered beaded porous coated and porous tantalum specimens (Bobyn et al., 2004; Hacking et al., 2000). Porous tantalum rectangular implants were implanted into the dorsal subcutaneous tissue of six mongrel dogs and studied at four, eight, and sixteen weeks. Using the peel test method, implants were clamped and the attached flap of tissue was pulled perpendicular to the implant with a tensile tester. The results showed that there was no statistical difference in attachment strength after four weeks; however, an upward trend in attachment strength was recognized as implant time increased. The average tissue attachment strength was 60.7 g/mm at four weeks, 70.9 g/mm at eight weeks, and 89.4 g/mm at sixteen weeks. These attachment strengths are all greater than the study completed by Bobyn et al. which is most likely attributed to higher porosity of the porous tantalum; twice that of the sintered porous coatings.

Depending on the method used to create a porous surface, there is a range of porosities achievable for metallic surfaces. Based on the size of the cells attempting to grow into the surface, some pore sizes are better suited for ingrowth than others. Vast research has been completed to analyze the optimal pore size for ingrowth of various cells, i.e., tissue and bone. Another important aspect to pore size determination is the fixation strength of the fibrous tissue once it has grown into the porous surface. Bobyn et al. used three ranges of pore sizes, 5-20, 20-50, and 50-200 μm and tested the effect of pore size on the fibrous tissue-porous implant interface (2004). The greatest attachment strength was observed for the largest pore range at nearly twice the strength of the middle pore range, and four times that of the smallest pore range tested. Intuitively, the longest time interval tested also had the greatest attachment strength. Therefore the greatest overall strength was seen in the 16-week, large pore size (50-200 μm) specimen with an average attachment strength of 27.5 g/mm. These findings are consistent with the research completed by Hulbert et al. where it was reported that the smaller pore sizes only allowed fibrous tissues to penetrate the pores, but substantial bone ingrowth was seen on the larger pore sizes, (100-150 and 150-200 μm) (1970).

Based on the preliminary results of the etching pilot study, two etching durations were selected for the *in vitro* experiments: one and two minutes. The thirty second etching showed no visible changes and was therefore excluded. From the remaining time points tested, the ninety second and two minute etching durations appeared to have similar results in pore diameters. The one minute and two minute etching durations were used as comparison to non-etched Ti6Al4V surfaces.

The approximate pore sizes used in this study ranged from 560 - 740 µm, which is larger than any of the previously mentioned studies. The etching process increased the size of the pores by removing material from the strut surfaces surrounding the pores. It was hypothesized then that the cells would proliferate more on the etched scaffolds when compared to the non-etched scaffolds. All discs showed living cells present and had good proliferation rates at day two, indicating that the cells were adherent and continuing to multiply when in contact with the EBM titanium discs. Since the percent reduction in alamarBlue® is correlated to the number of living cells present, then it can be extrapolated that there were a significantly greater amount of living NHEK cells present on the etched surfaces at day two than for the non-etched surfaces, which is consistent with the images acquired. While the NHDF-Neo cells on the discs etched for one minute for days two and seven appear to be fewer than on the other titanium surfaces, the day zero reduction indicate that the number of cells that initially adhered to the surfaces may have been fewer. Furthermore, the NHDF-Neo cells appear to be proliferating on the discs etched for two minutes at all time points studied. While this research only investigated the metabolic activity of the cells on the various surfaces and images of cell morphology, it is recognized that other analysis techniques like DNA assays may have provided a more complete analysis of the cellular well-being and surface topography preference. These assays were not available within the research lab that the studies were completed and funding was not available to have the analysis outsourced. The dermal fibroblasts used in this study were from a single donor and donor-to-donor variability has been shown to affect cell properties (Schneider et al., 2005).

The results from this study are promising that parts fabricated with EBM as well as etching the as-processed surface will create a good host for skin cells and may be a good surface and processing method for the transdermal surface coating of implants.

4.5 Conclusions

Previous research has shown that human skin cells have a preference for smoother surfaces. This research sought to find a solution to reducing the surface roughness of EBM as-processed scaffolds through chemical etching with HF/HNO_3. Dermal fibroblasts and epidermal keratinocytes were seeded on non-etched and etched surfaces and cultured for one week. Proliferation was greater for the etched scaffolds when compared to the non-etched surfaces, which may indicate that etching improves cellular growth. These results may indicate that this could be a good method for skin/implant surface modification in order to create a tight seal where the implant breaches the skin. If the skin is successfully attached to the implant, then it may reduce the occurrence of infection.

5.0 IMPLANTABLE DEVICE FOR *IN VIVO* TESTING TRANSDERMAL OSSEOINTEGRATION

5.1 Introduction

Designing custom implants requires a multidisciplinary approach to successfully achieve a proper fitting and mechanically stable implant. A custom implant design requires the knowledge of several areas of expertise including, engineering, orthopedics, and cell biology. The steps involved in creating a custom designed implant can vary from group to group, based on software and technology available, and level of experience and expertise. The basic process for creating a custom designed implant begins with acquisition of the shape of the amputated limb, because the designer must first understand the surface contours of the limb to which the implant will attach. As previously discussed, osseointegrated prostheses attach directly to the amputated bone. To acquire more detail on the shape and surface contour of the bone, medical imaging techniques can be used. Technology developments have led to several types of medical imaging techniques, some more useful than others, to obtain this information. The main radiological imaging techniques include x-ray, ultrasound, computed tomography (CT), magnetic resonance imaging (MRI), single photon emission computed tomography (SPECT), and positron emission tomography (PET) (Hill et al., 2001). Conventional x-rays send a burst of radiation through the body and an image of the area is captured on photographic film. Conventional x-rays and ultrasound are not useful for understanding the overall contour of the bone; however, the data is useful when the desired area is captured in a more comprehensive manner like with a CT scanner. A CT scanner is a donut-shaped device with a table that moves through the interior of the scanner. A rotating source emits x-rays and x-ray

detectors are positioned to measure the amount of radiation that is absorbed throughout the body. While the table moves through the machine the circular portion rotates creating a spiral scan pattern. A computer then converts these scans to two-dimensional cross-sectional images. The images display bones in white, soft tissue in various shades of gray, and air appears black. Although a MRI machine looks similar to a CT scanner, the way that it captures the images is very different. MRI does not use radiation, but works by emitting radio waves toward protons in the area of interest on the patient's body. These radio waves cause the protons to change position and produce signals that can be detected with coils within a high powered magnetic field. Again, a computer is used to interpret these signals and create a series of images showing slices of the body. MRI scans are used to better understand areas of the body that may not have been successfully analyzed with other imaging techniques.

While the images captured with CT scanning or MR imaging are very useful for medical diagnosis and evaluation, they are not useful in creating custom designed implants in their raw form. To utilize this information better the images need to be converted into three-dimensional images that can be imported into Computer-Aided Design (CAD) software. Once the image slices are captured they can then be loaded into specialized software for conversion and manipulation. Mimics, from Materialise, and 3D-Doctor, from Able Software Corporation, are two of these conversion software packages. The capabilities and functionality of each software package can vary, but the overall concept is the same. All of the 2D scans are imported into the software package and a 3D rendition of the area is created (Figure 26). The image contrast can be adjusted to make specific organs and tissues within the scanned area more visible. For bone anchored prostheses, the

exclusion of the amputated bone is important so that the shape and contour of the bone surface can be analyzed. The surrounding muscle and soft tissue is also of importance as the prosthesis should restore function without great detriment to the surviving tissues. These 3D images can then be imported into CAD software packages so that the implant design process can begin.
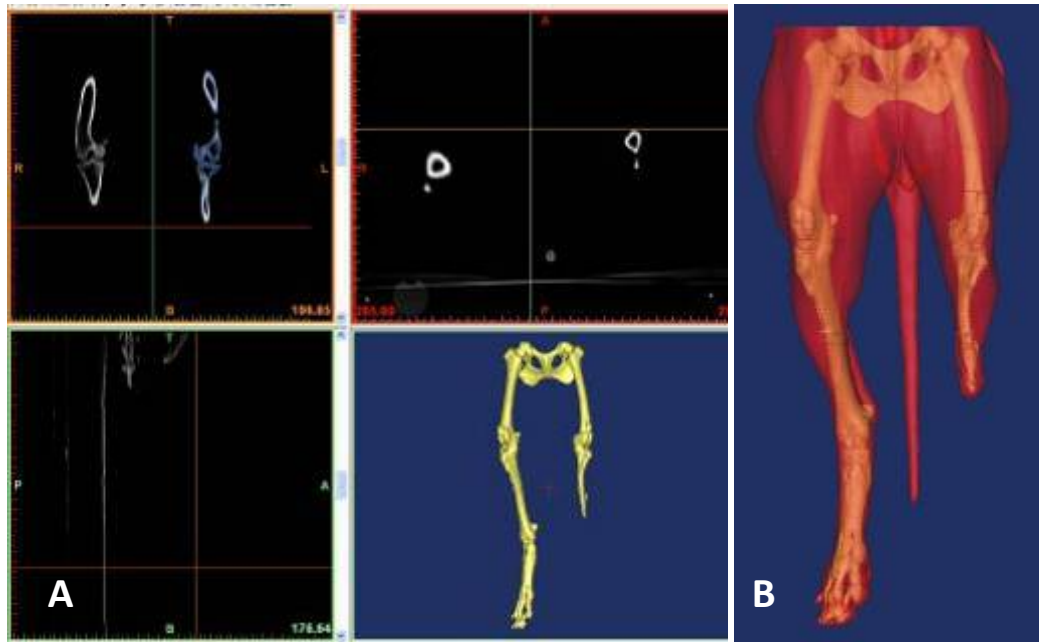
Figure 26: Images of 2D and 3D images of the distal portion of a canine skeletal system using Mimics software. A) Three orientation views and 3D view of area, B) 3D view of skeletal area with soft tissue transparent overlay.

Several CAD software packages exist that will allow the user to create custom geometries. The basic concept is that a desired surface contour can be selected, in a bone-anchored prosthesis this contour may be the outside of the amputated bone. Once this surface has been determined and selected the shape of the implant can be determined and drawn. This may involve offsetting

the surface from the desired contour and giving this offset a specific thickness, based on the material selected. With any design the material and method of fabrication should be considered prior to the final design. The material selected for the final product can determine the fabrication method used and the fabrication method could require certain design aspects or eliminate possible design aspects based on limitations with the selected fabrication process.

The final use and location of an implant should also be considered when selecting the material. With a saline content of approximately 0.9% and the temperature at nearly 100°F (approximately 38°C), the body is a relatively harsh environment for materials that will be implanted permanently or for a prolonged period of time (Davis, 2004). Biomaterials are referred to as synthetic materials, including metals, ceramics, and polymers, that can withstand the saline levels and temperatures of the biological environment and not evoke any adverse reactions while restoring a function to the body. Corrosion resistance is a critical characteristic for prolonged and permanent internal, medical devices. In orthopedics, these materials must also be able to withstand any normal loading. Practically, the material must also lend itself to manufacturing and sterilization. While each material category exhibits specific advantages for medical purposes, each of them is best suited for certain applications and conditions. For this research, the focus will be on the metallic biomaterials, referred to as biometals, due to the significant strength required in human load-bearing prostheses. Biometals that are commonly used as load-bearing implant materials are stainless steel, cobalt-chromium, tantalum, and titanium.

Stainless steels are named such because they are iron-based alloys with at least 10.5% Cr in order to prevent the formation of rust. The formation of an invisible and adherent chromium rich

oxide surface film results in the stainless characteristic. Corrosion resistance can be further improved with the addition of nickel. Other alloying elements can be added to improve mechanical and physical properties. Stainless steels are primarily used in applications outside of biomedical uses. When biomedical devices require only brief encounters with human tissue, commercial-grade stainless steels are utilized. For the devices requiring prolonged contact with human tissue, special production methods are required to ensure the correct material properties. Stainless steels are commonly referred to in one of five families. Martensitic, ferritic, austenitic, and duplex are based on the microstructure. The fifth family is based on the heat treatment used and referred to as precipitation-hardenable alloys. Martensitic stainless steels are Fe-Cr-C alloys with body-centered tetragonal crystal structure in the hardened condition. They have a high hardness and are therefore excellent for dental and surgical instruments. Ferritic stainless steels are iron-chromium alloys with body-centered cubic crystal structures. Ferritic stainless steels cannot be strengthened by heat treatment like the martensitic stainless steels and are also not often strengthened by cold working. Only a few applications are appropriate for the ferritic stainless steels, including solid handles for instruments, guide pins, and fasteners. The Duplex family of stainless steels has not been used in the biomedical field, but do have many advantages that make them ideal for the oil and gas, petrochemical, and other industries. Precipitation-hardenable (PH) stainless steels can be hardened by an aging treatment and are classified as austenitic, semiaustenitic, or martensitic, based on their solution-annealed microstructure. For medical applications, including neurosurgical aneurysm and microvascular clips, and various surgical and dental instruments, semiaustenitic and martensitic PH steels are used. The austenitic stainless steels are the most abundantly used of all the types of stainless steels. This family of stainless steels can only be hardened by cold working.

These materials have excellent cryogenic properties, high-temperature strength, and oxidation resistance. Austenitic stainless steels are utilized as both implantable and nonimplantable medical devices due to their good corrosion resistance and moderate strength. Some of the nonimplantable applications include canulae, guide pins, hypodermic needles, steam sterilizers, and work surfaces. For implantable devices austenitic stainless steels are best used as temporary fixation devices, due to the fact that they are not sufficiently corrosion resistant for long-term use. Some of these devices include, bone screws bone plates, and intramedullary nails and rods. The strength of stainless steel is inferior to that of other biometals and the modulus of elasticity is greater, comparatively. Implant-grade stainless steels are produced by vacuum melting (VM), vacuum arc remelting (VAR), or electroslag refining (ESR) so the material is resistant to pitting and crevice corrosion and to reduce the size and quantity of nonmetallic inclusions. Austenitic stainless steels are easily formed and deformation response can be controlled by adjusting the nickel content, with the increase in nickel content resulting in improved formability. They are also relatively inexpensive which makes them a common choice for medical uses. Stainless steel 316L (18Cr-14Ni-2.5Mo) is produced via vacuum melting and contains less carbon than the standard 316 stainless steel. Vacuum melting improves cleanliness and maximizes pitting corrosion resistance. Type 316L is usually used at the 30% cold worked state to increase yield, ultimate tensile, and fatigue strengths (as compared to the annealed state). However, it also results in decreased ductility. Austenitic stainless steels are not sufficiently corrosion resistant to withstand long-term use within the biological environment. Other stainless steels have been developed recently to combat this issue and increase corrosion resistance and improve mechanical properties. These stainless steels are ESR-processed nitrogen-strengthened stainless steel alloys.

The first uses of cobalt-based alloys date back to the 1930s. They were originally used as a dental alloy, but a decade later began to make its way into orthopedic applications. Initially the alloy was used for cast components, but soon the advantages of the wrought alloys led to their use (Davis, 2004). The selected production method for cobalt-chromium alloy implants can be determined by the required material properties and limits in manufacturing cost. Divine et al. found that the tensile and fatigue strengths of wrought and heat-treated cobalt-chromium more than doubled compared to cast versions of the material (1975). They also noted in the study that the crevice corrosion resistance and mechanical strength of wrought cobalt-chromium was superior to the cast materials, speculatively due in part to the chemical and structural homogeneity. Wrought cobalt-chromium versus the cast version has an improved tensile strength, but only a slight increase (Black, 1992). Unlike stainless steels, cobalt-chromium alloys are not easily machined. Investment casting is the best way to produce cobalt-chromium implants at a low cost. For structural applications, such as hip implants, the alloys can be forged resulting in maximum strength and toughness. Although processing cobalt-chromium alloys is more difficult in comparison to stainless steels the corrosion resistance is much better in cobalt-chromium alloys than in stainless steels (Davis, 2004.) One of the concerns with cobalt-chromium implants is the release of cobalt and chromium ions when used as an orthopedic implant material. Osteolysis and fibrous formation on cobalt-chromium implant surface can lead to aseptic loosening of the implant (Nicholson, 2002). Cobalt-chromium is a commonly used material for hip and knee implants.

Tantalum is categorized as a refractory metal, which has one of the highest melting temperatures at more than 2000°C (3630°F) and lowest vapor pressure. Other refractory metals

include, niobium, molybdenum, tungsten, and rhenium (not currently used for medical devices). Niobium, molybdenum, and tungsten are primarily introduced in biomedical applications through alloys of stainless steels, cobalt, and titanium. While in some cases tantalum is used as an alloying additive for titanium, it is also used in the unalloyed state (commercially pure tantalum) for medical devices. Tantalum is also used to coat carbon foam structures to form a porous tantalum creating a low modulus metal that has an appearance similar to cancellous bone and has been used in clinical applications since 1997 (Davis, 2004). This porous structure is created from commercially pure tantalum and possesses higher volume porosity than conventional porous coatings, such as cobalt-chromium or titanium beads (Bobyn et al., 2004). Tantalum is highly corrosion resistant, which makes it an excellent candidate for biological uses. This material is quite chemically stable and oxidizes in air at 300°C (Black, 1994). The solid tantalum has a modulus of elasticity of approximately 185 GPa, but is reduced to only about 3 GPa when the material is porous, well below that of other orthopedic implant materials (Levine et al., 2006). Tantalum is a highly ductile metal that forms a stable oxide component (Ta_2O_5) layer on the surface. The ductility of the material also lends itself to have much lower yield strength values than other biometals. The resistance to chemical attack and the excellent mechanical properties discussed earlier lead to the use of tantalum as an implant material. There has been evidence shown that when tantalum is implanted into the biological environment it can become osseointegrated (Black, 1994). The ability to achieve a high porosity, 75-85% allows for better bone ingrowth and mechanical attachment. This is much higher than the achievable porosity of cobalt-chromium sintered beads at 30-35% and fiber metal at 40-50% porosity. Tantalum has been successfully utilized as medical devices since the mid-1900's.

Some of the uses include: pacemaker electrodes, foil and mesh for nerve repair, radiopaque markers, sutures, cranioplasty plates, and prostheses. A bone-like apatite layer must form on the surface of tantalum before the material can bond to bone. There have been several successful animal studies that proved that this material can allow bone ingrowth and cell attachment. Many structural types of porous tantalum have been tested with successful bone ingrowth results, including foam cells, porous cylinders, and acetabular components (Levine, 2006). Electron beam (EB), powder metallurgical (P/M) pure tantalum, conventional pure tantalum wire and sheet, and various Ta-W alloys are available commercially (Black, 1994). The inability to cast tantalum, described by Venable and Stuck in 1943, has led to its reduced uses since it was first discovered (Black, 1994). Even though fabrication problems still remain, recently developed methods of fabrication have helped to increase the usage of the material.

Titanium exhibits key material characteristics that led to its popularity for medical implants, such as low density, high corrosion resistance, and superior biocompatibility (Davis, 2004). Titanium is classified as α, near-α, α–β, or β, determined by the material microstructure. The α phase is a hexagonal closed packed (hcp) crystal structure and at 885°C (1625°F) titanium allotropically transforms to the β phase becoming a body centered cubic (bcc) crystal structure. This transformation temperature can be raised and lowered based on the amount of interstitial elements, such as oxygen nitrogen, carbon (to raise the transformation temperature), and hydrogen (to lower the transformation temperature). Medically, the most commonly used forms of titanium are commercially pure titanium (CP-Ti), Ti-6% Al-4% V, and Ti-6% Al-4% V extra-low interstitial (ELI). The use of materials with high stiffness for implants in direct contact with the body can lead to

stress shielding and bone resorption due to the incompatibility between the modulus of the material and bone. For this reason, the use of titanium is thought to be advantageous as it has a modulus that is half of stainless steel and cobalt-chromium. However, with an elastic modulus of 110 GPa it is still much greater than that of bone with a modulus of only 10 – 30 GPa, but much less than other implant materials (Davis, 2004). Commercially pure titanium (CP-Ti) contains approximately 98.9-99.6% titanium, essentially containing all alpha titanium with a hexagonal closed packed (hcp) crystal structure. The yield strength of CP-Ti grades range from 240-550 MPa, based on the variations in oxygen levels (Beal et al., 2006). Increasing the oxygen and iron levels will lead to higher strength and by raising the amount of oxygen greater fatigue strengths can be achieved (Davis, 2004). Where high strength is not critical, but corrosion resistance is, CP-Ti is the ideal material. Titanium is an important alloying element with many other metals. In order to increase the strength of titanium small amounts of aluminum and vanadium can be used to create an alloy. The two predominately utilized alloys of titanium are Ti-6% Al-4% V, and Ti-6% Al-4% V ELI. The ELI was developed for improved ductility and fracture toughness (at cryogenic temperatures) over the standard Ti6Al4V. Ti-6% Al-7% Nb has a reduced elastic modulus of 105 GPA, while retaining an ultimate tensile strength of 860 MPa. With an even lower elastic modulus is the alloy Ti-3% Al- 2.5% V. It exhibits the lowest elastic modulus and ultimate tensile strength of all the α-β alloys, at 100 GPa and 690 MPa, respectively and has tensile properties 20-50% higher than CP-Ti grades. Some of the common biomedical applications for CP-Ti are pacemaker cases, dental implants, maxillofacial and craniofacial implants, and screws and staples for spinal surgery. Ti6AlV and Ti6Al4V ELI alloys have proven useful for total joint replacement arthroplasty, primarily hips and knees. In reference to biocompatibility, vanadium is considered to be a toxic element and therefore titanium alloys

without this element have been created. Ti-6% Al-7% Nb is one of the alloys considered to have increased biocompatibility, due to the addition of niobium (Nb) which is highly biocompatible. It has been used for femoral hip stems, fracture fixation plates, spinal components, fasteners, nails, rods, screws, and wire. It is used for tubing and intramedullary nails. Fluids within the body are highly corrosive which can lead to failures in materials that are not resistant to corrosion. Titanium is one of the most corrosion resistant materials known at this time and its ability to withstand the biological environment makes it a great material for medical implants. The body often responds to a foreign object by encapsulating it with a fibrous tissue layer to isolate it from the surrounding area. For load-bearing implants this coating can lead to instability of the implant and dislocation in joint applications. Titanium has been proven to be highly biocompatible in many different situations and, along with only a few other metals, the body will not respond to a titanium implant with the creation of the fibrous tissue layer and instead will grow in contact with the surface of the material. As in the research that Brånemark conducted in the 1950's, it has been proven that bone will actually grow onto titanium until it becomes part of the body and cannot be removed without fracture, i.e., osseointegration. Osseointegration requires a close fit between the material and the surrounding bone; therefore, custom-designed implants may promote ingrowth.

The introduction of more advanced manufacturing techniques have made it possible to create objects that otherwise would have been difficult or even impossible. Conventional machining techniques consisted of material removal methods that began with a piece of stock material and ended with the desired shape. Interior geometries were not achievable due to limitations of material removal tools. With additive manufacturing techniques, more complex geometries are

easily created from several types of materials. Specifically, Direct Metal Fabrication (DMF) methods have led to the ability to build intricate shapes directly from CAD to metal parts. There are several existing processes and systems that provide this technology, including: 3D printing, 3D fiber-deposition, selective laser sintering (SLS), direct metal laser sintering (DMLS), 3D laser cladding, and electron beam melting (EBM).

Unlike commercially available sintered beads and wire mesh, 3D printing allows the user to produce casting surfaces with complex geometries without requiring post processing. Typical of additive manufacturing systems, the part is built layer-by-layer from a CAD model. As a print head deposits silica binder in the pattern of the design for that layer, it bonds the alumina powder. Another layer of powder is swept onto the powder bed and the process continues until all layers are completed. Heat treatment then consolidates the bonded powder and the loose powder can be removed to expose the mold. Melican et al. successfully produced porous surfaces with a dimensional resolution of 175 μm (2001). A canine transcortical implant model was conducted to test these surfaces and the results showed that the porous surfaces created with 3D printing molds failed at a much greater shear stress than the control group, commercially sintered beaded coatings. Bone ingrowth structures for orthopedic prostheses have also been created with 3D printing. Curodeau et al. used 3D printing to create ceramic molds with built in textures printed directly into the mold surface (2000). Overhangs and undercuts were produced in one step and the molten metal could easily infiltrate the sub-millimeter cavities. Once the mold was removed the functional metal part was revealed. The dimensional limitations to this system are the minimum printed feature size, which is directly related to the binder-powder interaction and the stress limitations of

the features. An experiment by Curodeau et al. indicated that this minimum feature size is on average 350 µm long, 200 µm wide, 175 µm high for withstanding the powder removal stress. However, during casting the pressure of pouring the molten metal to create the positive part requires a larger minimum feature size of approximately 350 µm by 350 µm by 175 µm.

Another method of producing metal parts is to extrude metal slurry. 3D fiber deposition uses air pressure to regulate the flow of slurry through a stainless steel syringe and controls the extrusion path with a positional control unit that receives its commands from a computer with the desired shape of the part. Li et al. produced porous scaffolds with Ti6Al4V slurry creating highly controllable porosity and pore size (2006). The slurry was created with approximately a 2:1 ratio of Ti6Al4V powder in an aqueous solution of methylcellulose and stearic acid and stirred for one hour at room temperature. The scaffolds were designed by laying down 2D layers of continuous fibers of material with an alternating pattern of 0° and 90° orientations of the pattern. The pore size created was approximately 400 µm to promote ingrowth of bone. Upon completion of the deposition process, the parts were dried for 24 hours at room temperature and then another 24 hours at 50°C. After drying the parts were then sintered in a high vacuum furnace at a maximum temperature of 1250°C. This method does not lend itself to the creation of complex contours and therefore may not be a preferred method for custom implant creation.

Selective laser sintering (SLS) is an increasingly popular choice in additive manufacturing techniques, due in part to the ability to use many different types of materials, such as: polymers, metals, ceramics (including foundry sand), and many composites (Kruth et al., 2003). The powder material is solidified by thermal energy in the form of a laser beam. The interaction between the

powder material and the laser beam determines the feasibility and level of quality of the SLS part.

Once the first layer is fused the build platform is lowered and a second layer of powder material is

deposited on top of the previous layer and the laser beam fuses the powder of the second layer to

the first layer. This process continues until all layers have been built leaving a completed part. This

process can yield metallic parts without the use of a polymer binder material; however, to increase

the range of possible metallic powders a sacrificial polymer binder must be used. Upon completion

of the sintering process the binder must be removed by furnace post treatment leaving the metallic

part. The creation of porous parts also requires a post-densification operation by furnace post-

sintering, by pore infiltration, or by hot isostatic pressing.

Direct metal laser sintering (DMLS) is also a form of additive manufacturing and therefore

builds parts layer by layer from a CAD model. The above mentioned processes require a metal mold

part to be produced and then later a metal part can be achieved from that mold, whereas DMLS can

build a metal part without first creating a mold (Khaing et al., 2001). This allows for a much shorter

lead time in creating metal parts, i.e., within a few days. DMLS was created in Munich, Germany by

EOS GmbH and was made commercially available in 1995. It uses a laser to directly expose the

metal powder in liquid phase sintering. Two powder systems are available with this machine. The

bronze-based powder requires no controlled atmosphere, whereas the steel-based powder requires

a nitrogen atmosphere. The EOS machine uses a 200 W CO_2 laser with a wavelength of 10.6 μm and

a spot size of 0.3 mm.

Three dimensional laser cladding is similar to direct metal laser sintering and can produce

3D metal parts directly without the requirement of subsequent steps, unlike selective laser sintering

and 3D printing (Kreutz et al., 1995). For one-step cladding using the blown powder technique a

laser induced melt-pool is scanned and fusion bonded to the clad. There is a second technique used

to produce parts via 3D laser cladding which uses a better controlled powder delivery technique.

The advantage to this delivery method is that it does not require an inert-gas build chamber for

producing parts and therefore larger parts can be produced and a more complex cladding path can

be traced. There are several critical components for this additive manufacturing technique

including, the laser, the focus and beam shaping optics, the nozzle, the powder and gas delivery

system, and the substrate on a moving stage (Hu et al., 2003). The key to controlling powder

delivery is a real-time powder delivery rate sensing and control unit. Another critical element to

successful 3D laser cladding is sensing of the molten pool, which has proven to be a difficult task to

achieve due to the placement of the camera or phototransistor.

   While the laser based systems have superior resolution compared to most other methods of

direct metal fabrication, the laser based systems typically exhibit problems with reflectivity leading

to power efficiency losses. Additionally, most of these fabrication techniques, discussed above,

require multiple steps to achieve a metal part or are crude forms of metal fabrication, requiring

significant post machining to achieve desired shape. Electron beam melting offers the ability to

produce metal parts directly from CAD models with minimal post-processing and energy efficiency

(Figure 27). As the other additive manufacturing techniques, electron beam melting (EBM) uses

specialized computer software to slice the CAD model into layers. Each layer is built upon the last

layer creating a fully dense 3D metal part. The uniqueness of this fabrication technique is the use of

an electron beam to weld the metal powder layers together, with build layers ranging in thickness

from 0.07 - 0.25 mm (Harrysson et al., 2008). The electron beam is produced with a thermionic emission gun with a tungsten filament emitting a maximum power of 4.8 kW. The build process takes place in a vacuum chamber at 10^{-4} mbar while the gun remains at 10^{-6} mbar. Building under vacuum eliminates impurities leading to enhanced material properties. Sintered powder surrounding the part helps to support overhangs and is easily removed upon completion of the build. Unused powder is also free from oxidation while under vacuum and is able to be recovered and reused, which helps to lower material costs. Each layer undergoes preheating prior to sintering to help reduce the thermal gradient between the melted layer and the rest of the part to minimize the residual stresses that can cause the part to warp (Cormier et al., 2004). After preheating, the initial layer is melted by increasing the power of the beam and then the build platform holding the start plate is lowered one layer thickness. A layer of powder is deposited onto the existing layer and that layer is melted. This process continues until all layers are completed. The cost to operate the electron beam is primarily determined by the cost to replace the filament, which is a low cost component. Arcam offers the following powders: Ti6Al4V (ASTM F136), Ti6Al4V ELI (ASTM F136), and CoCr Alloy (ASTM F75), that undergo rigorous testing and evaluation to confirm the correct composition and material properties (Arcam AB, Mölndal, Sweden). Once the parts are built using EBM technology, the parts exhibit material properties that are superior to cast titanium. Another unique characteristic of the EBM machine is that different heating parameters can be applied to various parts and even various sections within a single part. This enables the user to build both solid structures and open pore structures within the same build and/or part. The open pore structures can be built as a standalone structure or with a solid core. The EBM is a unique

technology that enables the production of porous metal implants for skin and bone ingrowth with a

solid core for strength in one single step.

Figure 27: Photograph of an electron beam melting (EBM) machine, model A2 (Arcam AB, Mölndal, Sweden).

The transdermal osseointegrated implantable device has a similar design to the transdermal

osseointegrated implant design and consists of two major components; a porous coating and a solid

structure. The structural component is necessary to withstand the forces realized with normal

movements, and the porous coating is required for bone and soft tissue ingrowth. When a coating

is applied to a solid structure, or in this case a porous layer is built upon a solid structure, it is

important to test that the coating is strong enough to withstand any usually loading. This research

investigates that structural integrity further.   Additionally, infections among transdermal

osseointegrated implants are a concern as they can lead to implant failure. Skin attachment at the implant surface is proposed as a method for reducing infection at the implant site. Some researchers are also exploring antimicrobial surface treatments and antibiotic injections to reduce bacterial levels at the implantation site. The device designed in this research will enable future research in this area *in vivo*. Peel testing of the skin after a specified period of implantation can be used to analyze skin attachment. The device is also designed to allow researchers to test various antimicrobial injections, while maintaining sterile conditions.

5.2 Materials and Methods

5.2.1 Fabrication and Preparation of Shear Test Specimens

The creation of porous surfaces built directly from biocompatible metals, such as titanium and titanium alloys are possible with additive manufacturing processes. Although the part is built in one step using EBM and is removed from the machine as one device, separate files for the porous sections and the solid sections of the implant must be uploaded to the machine. This is one reason why understanding the strength between the porous layer and the solid layer is important. The porous section is necessary for tissue ingrowth; both skin and bone. The solid portion of the implant is needed for strength and load bearing. Adequate shear strength between the two portions is of most concern when analyzing strength of osseointegrated, load-bearing implants and how they will perform *in vivo*. Tensile forces and compression forces are not as critical as the shear strength of these implants due to the way in which the implant is loaded. Tensile forces should be negligible

due to the downward force of the body on the leg and the compressive forces will be more prevalent in the base of the implant. The forces between the bone and the circumferential portion of the implant should be able to withstand any forces from possible micromotion, because this interaction is the main area for bone ingrowth. Following successful bone ingrowth, this shear movement will be decreased as the relative motion of the bone to the implant is reduced.

American Standard for Testing Methods (ASTM) creates standard procedures for testing various materials, such as coatings. No standard testing procedure exists for testing the shear strength of the porous coating to the solid surface of parts produced with EBM. Therefore, ASTM F 1044-05, the testing procedure for testing calcium phosphate and metallic coatings, was used as a reference for specimen design and testing procedures. Based on the ASTM standard, the test pieces were designed in SolidWorks® CAD software package. The method for gripping the test piece in the tensile tester was modified slightly with the addition of "shoulders" to eliminate slippage of the test piece from the tester grips. Figure 28 shows the orientation of the solid and porous portions.
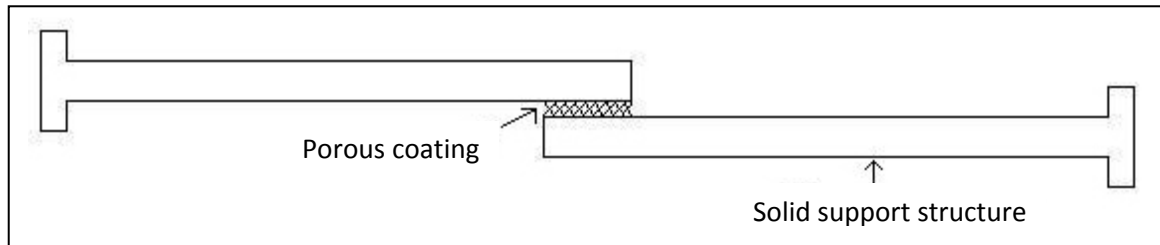
Figure 28: Shear test specimen design (Side view)

In order to create the porous section of the test specimen, a solid was created in the design software package Magics (Materialise, Belgium) with the overall desired dimensions. Then an

oversized open mesh structure with hexagonal unit cells and 1.2 mm spacing between the struts was imported into the Magics software. A Boolean operation was performed resulting in a porous part with the required dimensions. Two porosities were tested to compare the shear strengths. In order to obtain a part with less porosity the open mesh structure was reduced to be 75% of the original. This resulted in spacing between the struts of 0.9 mm with an initial porosity of 76% and a reduced porosity of 36%. The solid portion was designed in SolidWorks® (Dassault Systèmes SolidWorks Corp.; Concord, Massachusetts) and the final dimensions can be seen in Figure 29. Once imported into Magics the porous and solid components were aligned. Approximately 1.0 mm of overlap between the porous and solid parts was allowed to ensure the melting process created one part. In order to compare the shear strengths of various coating thicknesses, the porous sections were created with three different thicknesses prior to alignment with the solid portion. The thicknesses tested were 1.5, 2.0, and 3.0 mm. These values represent two layers of coating; one for each solid portion. Therefore the actual coating thicknesses tested were 0.75, 1.0, and 1.5 mm, which are typical coating thicknesses used for implants of this type.
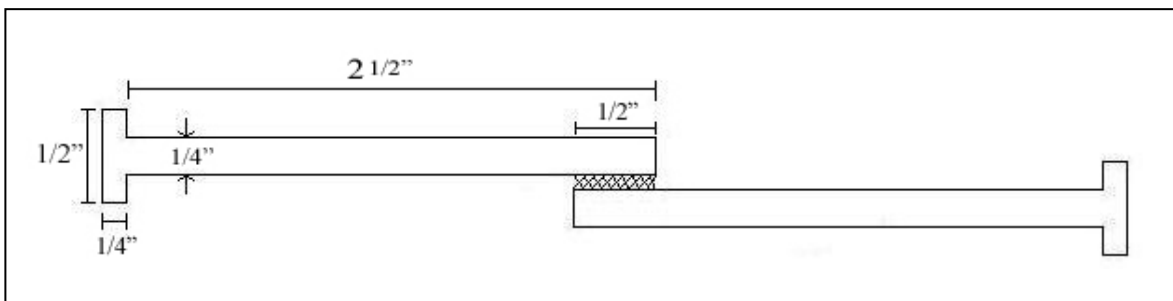
Figure 29: Overall design and dimensions for the shear test specimen (in inches), Side View. The thickness of the porous section is 3 mm.

All test pieces were oriented similarly on the build platform to ensure the same slicing orientation. After creating support structure, the files were uploaded to the EBM machine. Despite the fact that the porous parts and solid parts were imported as separate files, the EBM built both parts simultaneously in each layer. Ti6Al4V powder was used for the creation of these parts because of its superior biocompatibility and excellent material properties.

Upon completion of the build process, the parts were removed from the machine and blasted with titanium powder to remove any loose particles that became trapped in the porous section of the specimen and the support structure was removed. Some of the powder in the porous section was entrapped and was not able to be removed with the blasting technique.

5.2.2 Testing Shear Strength

A universal testing machine (Applied Test Systems 1605C, Butler, PA), with a 5,000 lb load cell and a cross-head speed of 0.05 in/min was used to test the specimens to failure. When testing shear strength, it is important to be attentive to the alignment of the grips holding the test piece to ensure the test is a true shear test and does not introduce any undesired bending moments. The placement of the test piece and alignment are shown in Figure 30.

In order to understand the approximate load in which these test pieces would fail, a few initial test runs were completed. Two samples were created with a cross-sectional area of 1.0 by 1.0 inches and pulled until the machine reached its peak load capability of 5,000 lbs. This did not result in failure of the part and therefore a second test run was required. For the next test the cross-

sectional area was reduced to 0.5 by 0.5 inch which translated to a four times greater applied stress to the porous section during testing. Three thicknesses of porous sections were tested in this trial: 1.0, 2.0, and 3.0 mm, to understand the approximate range of failure loads. Shear stresses at time of failure were 2.7 ksi, 11.4 ksi, and 9.8 ksi, respectively. The overall length of the solid portion of the test specimens is not critical and therefore to reduce unnecessary material usage, the length of the solid bars was reduced by 0.75 inch.
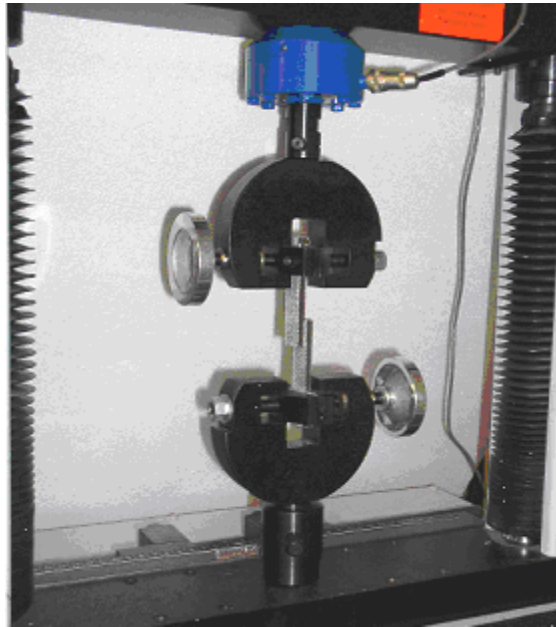
Figure 30: Shear test specimen loaded on the universal testing machine.

For the final experimental testing, two porosities (36% and 76%) and three thicknesses (1.5, 2.0, and 3.0 mm), shown in Figure 31, were tested. Three samples of each type of specimen, eighteen samples total, were fabricated using EBM. Each specimen was numbered and the testing

order was randomized to ensure independence for statistical analysis. Again, the samples were

tested to failure; the point at which the solid portions became two separate structures. Ultimate

shear stress was calculated with the formula:

$$\tau = V/A, \text{ where}$$

τ = ultimate shear stress,
V = maximum applied shear force, and
A = cross-sectional area of the porous section.

Shear strain was calculated with the formula:

$$\varepsilon = \tan q = Dx/t, \text{ where}$$

ε = shear strain,
tan q = angle of displacement,
Dx = displacement in the direction of the applied force, and
t = thickness of porous section.
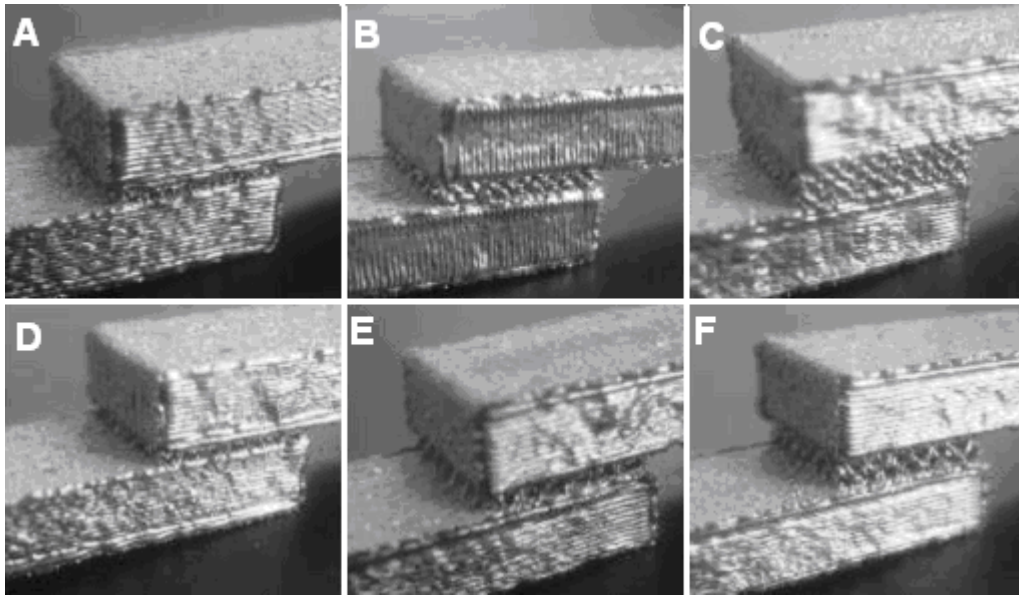
Figure 31: Shear specimens tested with coating dimensions; A) 36% porosity and 1.5mm thickness, B) 36% porosity and 2 mm thickness, C) 36% porosity and 3 mm thickness, D) 76% porosity and 1.5mm thickness, E) 76% porosity and 2 mm thickness, F) 76% porosity and 3 mm thickness.

5.2.3 Implantable Device Design

In order to accommodate any future research that will require *in vivo* testing to reduce bacterial infections at the implantation site, the implantable device was designed with a hollow interior and closeable opening for possible antimicrobial injections and medications. The device was designed as a standard size for future research comparison purposes and ease of implantation. For the purpose of this research it was designed to accommodate the tibia of a medium-size, adult dog. Testing the interstitial shear strength of ingrowth may be an important area for research and therefore the bone and device must be able to be removed *en bloc* without completely compromising the stability of the tibia. Once this portion of bone and the implanted device are surgically removed a standard bone plate may be inserted to restore the strength of the bone during bone healing.

CT scans of a medium-sized canine patient, Mimics® (Materialize; Leuven, Belgium) were used to determine the overall dimensions of the device. The CT scans are a series of two dimensional (2D) sagittal images of both bone and soft tissues within the scanned area. The 2D scans are then imported into Mimics® and converted to a three dimensional (3D) rendering of the scanned area.

This implantable device was designed to be implanted into the bone of a patient and the surrounding skin will be sutured to the top portion of the device. It has four distinct parts to the overall design; the main body (Figure 32), the top cover (Figure 33), the threaded cap (Figure 34), and a silicone injection disc. The main body has several features to secure it to the implantation site. The three wing-like structures are to secure the device to the bone after the base has been

press fit into the bone. They are intentionally thin so they can be shaped to contour the patient's

bone. The flange at the top of the main body is for soft tissue attachment with sutures. The top

cover is designed with threads to secure into the top of the device main body. It has a large dome

shape that extends beyond the area where the skin is sutured to the device main body. Since this

device is designed to be implanted into dogs, it is important that the top cover protect the

implantation site from saliva and scratching that may occur during the healing process.   As

previously stated, this device is designed such that injections can be made into the bone at the

implantation site. To maintain sterility of the area, a self-healing silicone disc (8mm diameter) is

inserted into the lower portion of the device as illustrated in Figure 35. This disc is held in place with

the threaded cap that secures to the end of the device. The threaded cap can be either solid or

have a porous layer attached to a solid shell. This versatility will enable future researchers to modify

the device to conform to their particular study.

A)   B)
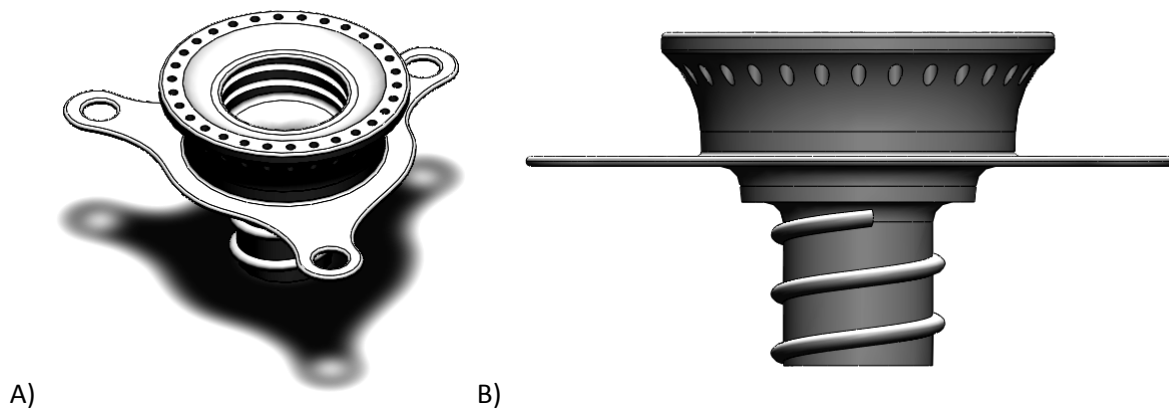
Figure 32: images of the main body of the transdermal osseointegrated implantable device: A) isometric view, B) side view, dimensions: 20 mm diameter (not including wing-like flanges), 37 mm maximum width of part, and 15.8 mm height.
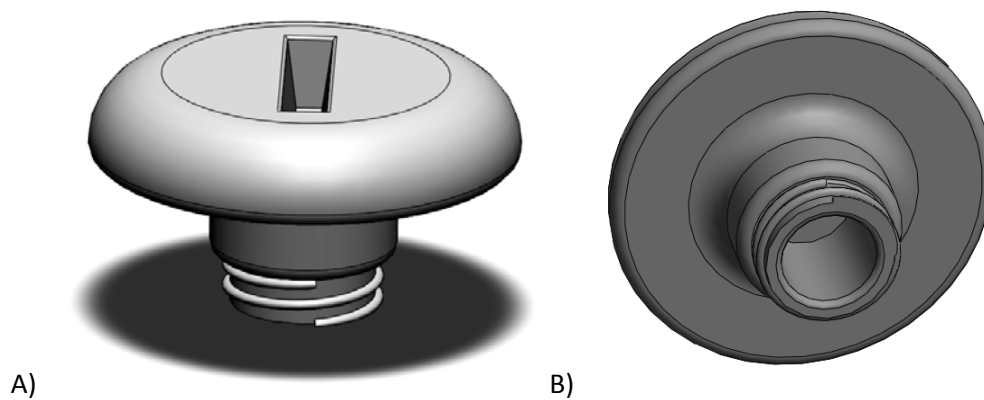
Figure 33: Images of the top cover of transdermal osseointegrated implantable device: A) top/side isometric view, B) side/bottom isometric view, dimensions: 30 mm outer diameter (at the widest point), 16.6 mm height, 7.5 mm internal diameter (within the threaded portion).
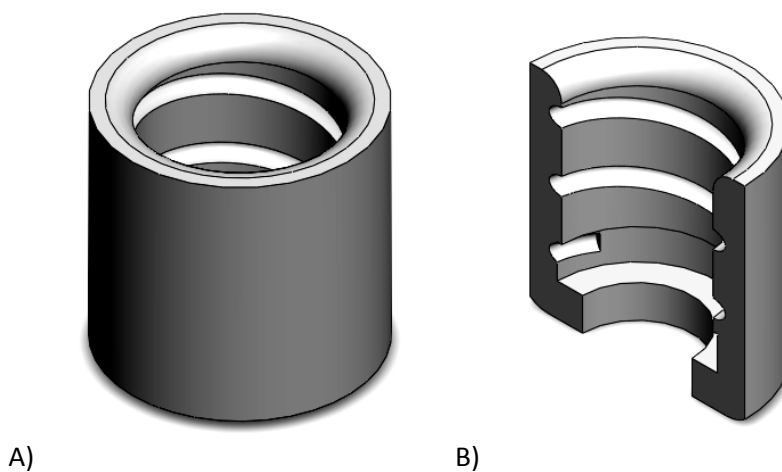
Figure 34: Images of the threaded cap for transdermal osseointegrated implantable device: A) top/side isometric view, B) top/side isometric view – cutaway, dimensions: 12 mm outer diameter and 10.5 mm height.
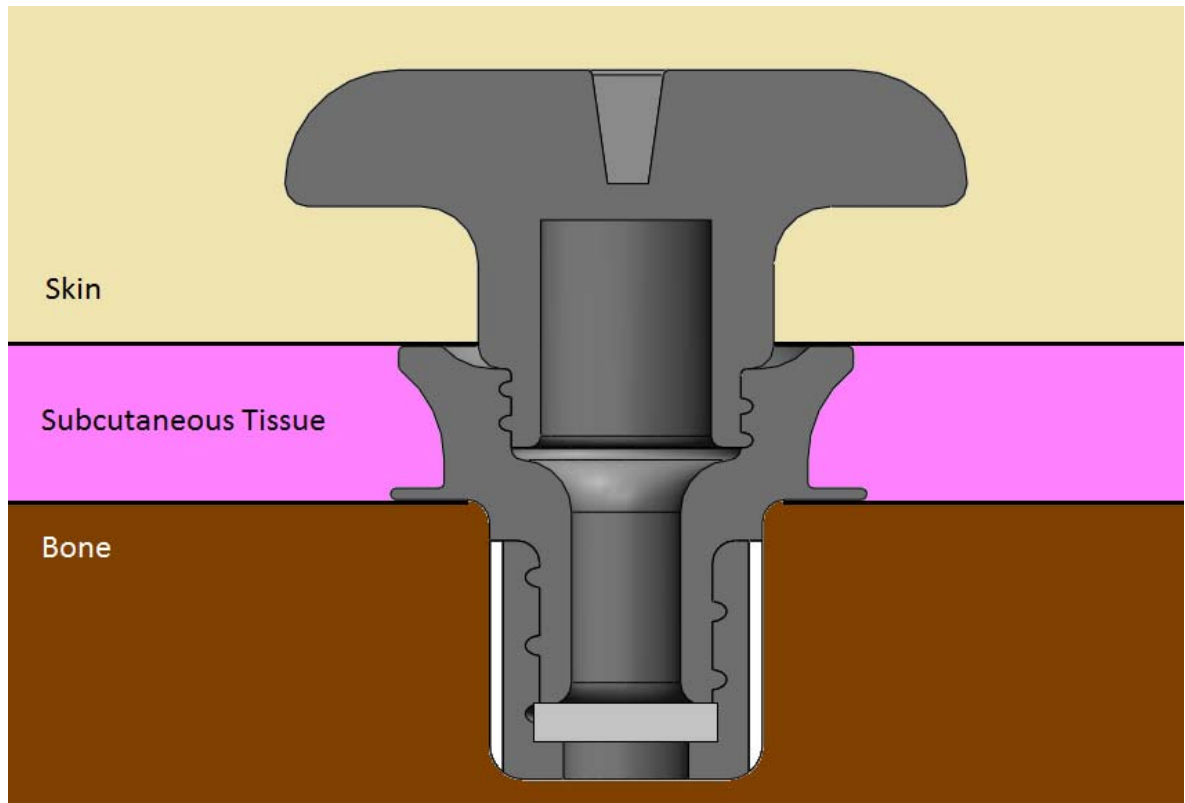
Figure 35: Transdermal osseointegrated implantable device assembly with 8 mm diameter silicone disc (pictured in light gray) for injection port and mesh coating layer of threaded cap (pictured in white).

5.2.4 Implantable Device Prototype Build

Rapid prototyping technologies make prototype fabricates easier and timelier than conventional machining processes. The final device was fabricated out of Ti6Al4V, due to its biocompatibility and excellent material properties (Figure 36). An initial plastic model was developed to test the concept more economically. Additionally, using existing CT scans from a previous canine patient within the desired size range, models of tibias were built using fused deposition modeling (FDM). Molds of the canine's soft tissue were created using FDM, the supports were removed, and the model was sanded and painted to create a smooth surface finish. The soft

tissue model was then used to create a silicone mold. The tibia model was then placed into the soft tissue silicone mold and the mold halves were sprayed with mold release and closed. Ballistics gel was melted and poured into the mold and left to solidify for two days. The model of the bone and soft tissue was then removed and covered in plastic for a future surgical rehearsal.

Figure 36: Transcutaneous osseointegrated implantable device components (from left to right: top cover, main body, porous threaded cap, and solid threaded cap) as fabricated with electron beam melting using Ti6Al4V powder; A) with support structure attached, B) after removal of support structure.

5.3 Results

5.3.1 Results of Shear Testing

From the stress-strain graphs for each specimen tested, the shear modulus was determined as the slope of the linear portion of the graph. The shear moduli are tabulated along with the force at failure and the failure strength in Table 6. The average failure strength for the 76% porosity test piece was 20.62 MPa while the 36% porosity, on average, failed at 39.71 MPa.

Table 6: Shear testing results, average values from three replications.

	Thickness (mm)	Force at Failure (N)	Failure Strain	Failure Strength (MPa)	Shear Modulus (GPa)
76% porosity	1.5	3502	0.93	21.71	0.023
	2	3021	0.73	18.73	0.047
	3	3454	0.47	21.42	0.050
36% porosity	1.5	5958	1.27	36.95	0.035
	2	7219	1.00	44.77	0.050
	3	6034	0.73	37.41	0.053

Statistical software (JMP 8.0, SAS, Cary, NC) was used to analyze the results of the experiment to determine any significant differences in failure strengths among the porosities and thicknesses tested (Table 7). The porous coating porosity resulted in statistically different failure strength values ($P < 0.001$). In contrast, the thickness of the porous coating does not result in a significant change in failure strength of the specimen.

Table 7: Failure strength significance test for specimen thickness 1.5, 2.0, & 3.0 mm and 36% and 76% porosities, *P*<0.05 was considered significantly different. Different letters indicate significant differences among the group tested.

Thickness	Level	Mean Failure Strength (MPa)
1.5 mm	A	29.33
2.0 mm	A	31.75
3.0 mm	A	29.42
Porosity	**Level**	**Mean Failure Strength (MPa)**
36%	A	39.71
76%	B*	20.62
* significantly different with *P*<0.001		

5.3.2 Practice Surgery Planning

A hole, 11.5 mm in diameter, will be drilled proximally into the prototype tibia. The device will be press fit into the opening to ensure a tight fit (Figure 37). The device will be removed and the area surrounding the implantable device will be stabilized with a standard bone plate post-surgery.

A)   B)
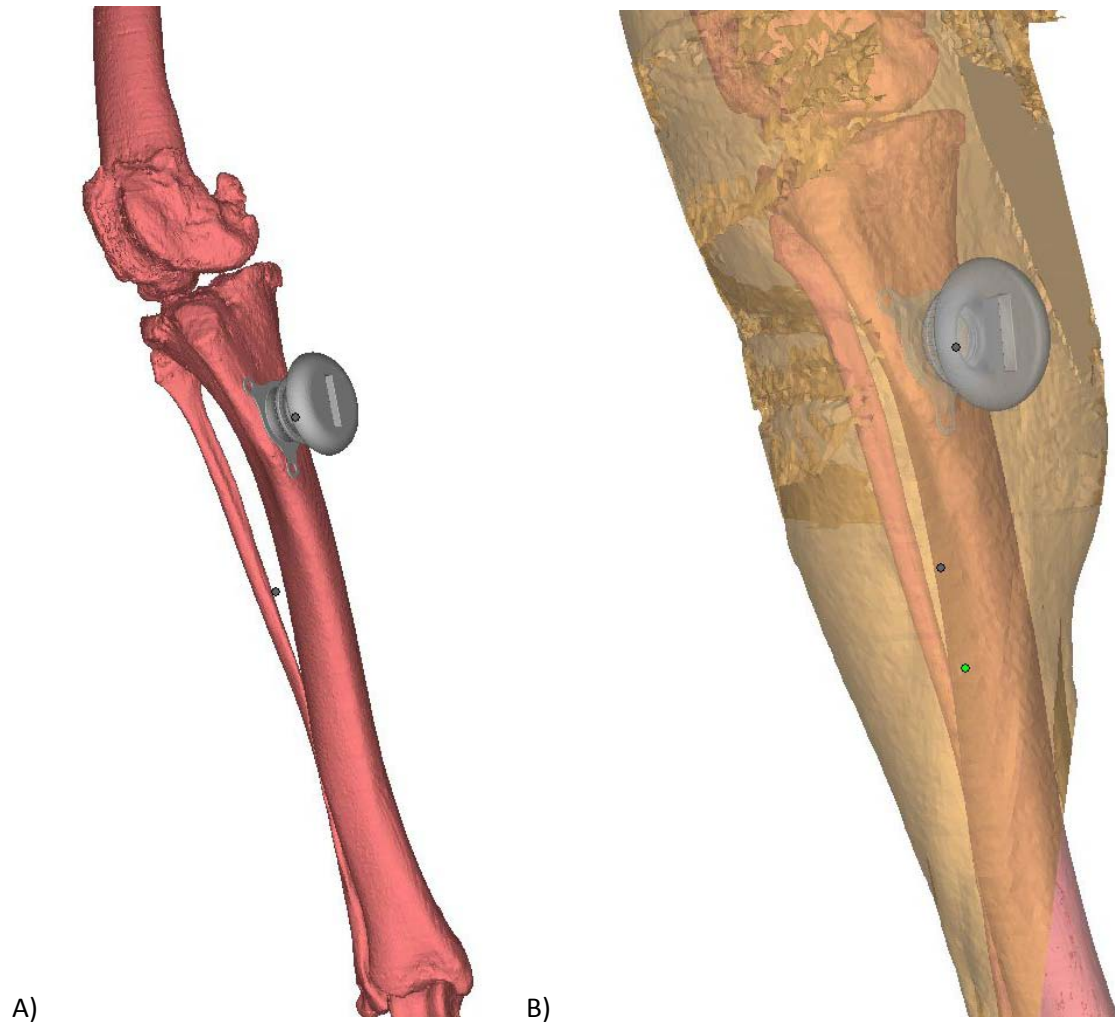
Figure 37: CAD images of transdermal osseointegrated implantable device implanted into a medium-sized canine tibia, A) skeletal view, B) skeletal view with semi-transparent overlay of soft tissue.

5.4 Discussion

Biometals that are commonly used as load-bearing implant materials are stainless steel, cobalt-chromium, tantalum, and titanium. Stainless steel has been used as an implant material for an extensive period of time. As the corrosion resistance of cobalt-chromium was discovered to surpass that of stainless steel within the biological environment it began to gain popularity as a biometal. The advantages that titanium possesses within the harsh environment of the body began to unfold in the early 1940's and, slowly, it challenged both stainless steel and cobalt-chromium as the preferred metal for orthopedic and dental applications. With the ability to create 70-80% porous structures, and again a superior resistance to corrosion, tantalum has also been successfully used in surgical procedures, but its uses are still limited. A comparative overview of the advantages, disadvantages, and primary uses of selected metals and alloys used for implant applications is shown in Table 8.

Table 8: Comparison of some of the characteristics of orthopedic metallic implant materials, (Davis, 2004).

	Stainless Steels	Cobalt-base Alloys	Ti & Ti-based Alloys
Advantages	Cost, processing	Wear resistance, corrosion resistance, fatigue strength	Biocompatibility, corrosion, minimum modulus, fatigue strength
Disadvantages	Long-term behavior, high modulus	High modulus, biocompatibility	Lower wear resistance, low shear strength
Primary Uses	Temporary devices (fracture plates, screw)	Dentistry castings, prostheses stems	Long-term permanent devices (pacemakers, nails)

Implants with a high stiffness, such as those fabricated with titanium, can lead to stress shielding, which leads to a reduction in bone mass due to the absence of normal stresses. However, bone ingrowth into porous titanium surfaces has been shown to reduce the elastic modulus. The mechanical property changes associated with the composite of bone and titanium were investigated by Thelen et al. to ensure properties were conducive to weight-bearing prosthesis (2004). The mechanical behavior of the bone-titanium composite material was simulated and analyzed with finite element modeling, using a porosity of 33%. In the first simulation the pores were completely filled with bone and in the second simulation only 35% of the pores were filled, illustrating both complete and partial bone ingrowth. The effects of the pore shape and roughness was also considered and compared in the simulations. Their findings of the finite element simulations showed that the elastic modulus of the porous titanium can be dramatically reduced as bone grows into the pores.

Research has been completed to determine the shear strength required to push-out bone integrated into porous surfaces. The results of those studies have given this research a baseline for required shear strength of a coated surface. The results of the shear tests showed that the lower porosity specimens, i.e., the more dense specimens exhibited a greater strength. This is to be expected as that implies more surface contact between each solid structure and therefore requires more force to separate. In our research, average failure strength for the 76% porosity test piece was 20.62 MPa while the 36% porosity, on average, failed at 39.71MPa. Three thicknesses were also tested; 1.5, 2.0, and 3.0 mm, representing two layers of coatings, with no correlation for the thickness of the coating relative to shear strength. The shear strength results can be compared to the push-out strength from growth into similar porous surfaces to better understand if it is

adequate. Research shows that the interstitial shear strength from push-out tests have resulted in a range of values. It has also been shown that this shear strength can be increased with implant surface coatings. Inadome et al. tested the push-out strength of hydroxyapatite-coated Ti6Al4V plugs implanted into canine femurs (1995). The results showed an average interfacial shear strength of 7.3 ± 1.4 MPa at 4 weeks and 10.9 ± 3.1 MPa at 12 weeks (n = 12). This value is well below the shear strength of the specimens tested in this study. The EBM scaffolds within this study had shear strength slightly lower than the shear strength of human femora (Turner et al., 2001). The compressive and bending strength of porous EBM scaffolds has been reported elsewhere (Harrysson et al., 2008). In a separate study by Søballe et al. the shear strength was much lower for hydroxyapatite coated titanium cylinders implanted into dogs at 6.57 ± 0.4 MPa and 7.04 ± 0.7 MPa for non-coated titanium (1990). Nishiguchi et al. inserted implants in the femora of six dogs and revealed the mean shear stress at 4 weeks to range from 10.8 ± 3.5 MPa to 15.0 ± 2.7 MPa and at 12 weeks ranged from 16.0 ± 2.5 MPa to 16.7 ± 4.3 MPa (2001). These results indicate that depending on the implant coating the implant shear strength can vary slightly, but shear strength values are well below the values of the porous coated Ti6Al4V produced with EBM. Both 76% and 36% porosities have a shear strength that is adequate for the interstitial shear strengths reported in research and therefore analyzing the cellular response differences between these two porosities should be researched *in vitro* and *in vivo* before an optimal porosity can be determined. The transdermal osseointegrated implantable device will allow further research of the porous coating through *in vivo* testing.

5.5 Conclusions

5.5.1 Shear Testing Conclusions

The results of the failure shear strength testing confirmed that the thickness of the coating, within the tested range, does not significantly affect the shear strength. However, the density of the porous coating does correlate with the shear strength at which the samples will fail. Specifically, the lower porosity specimens, i.e., the more dense specimens exhibited a greater strength. The EBM porous coatings had shear strength slightly lower than the shear strength of human femora. If these coatings are used as implant ingrowth surfaces, it may reduce stress shielding. The results from this study can be extrapolated into a larger study with more porosity variables to determine the optimal configuration for the desired implant surface depending on the patient and the location of the implant.

5.5.2 Implantable Device Conclusions

The implantable device will remain in place for a specified period of time, after which it is removed along with a portion of the surrounding bone. Testing of the device and surrounding bone can then be performed for the desired study. The design of the device allows the patient to return to a normal life after a small bone fixation plate is placed over the area of removed bone. This consideration gives researchers the ability to study ingrowth into the implant surface *in vivo* while avoiding the use of research animals.

6.0 DISCUSSION

While the ability to produce custom metal implants with EBM has been established, the biocompatibility of implants fabricated with this method is not well-known. EBM allows the direct fabrication of porous surfaces that may promote ingrowth for transdermal osseointegrated implants. Porous surfaces have been shown to improve cell migration and soft tissue attachment. Various pore diameters have been studied to determine the range that promotes the greatest cell growth, with most studies showing that pores greater than 40 µm lead to less fibrous tissue formation and pores in the highest range for each study typically showed the best cell growth (Bobyn et al, 2004; Hulbert et al, 1970; Pitkin et al., 2006).

This research aimed to investigate the cellular response of hASCs, NHDF-Neo, and NHEK to EBM produced titanium discs with various surface topographies. The proliferation and cytokine release of hASCs were improved for the EBM porous discs when compared to the solid polished discs, indicating that these cell types likely prefer surfaces with greater surface roughness values. When epidermal keratinocytes and dermal fibroblasts were seeded on discs with identical surface topographies, they exhibited improved proliferation rates on surfaces with lower surface roughness values. In order to create a transdermal osseointegrated implant with both optimal skin and bone ingrowth surfaces a method was required to reduce the surface roughness of the EBM as-processed surface. Chemical etching with hydrofluoric-nitric acid was selected as the method to reduce the surface roughness while also increasing the pore diameter. The etched surfaces were then cultured

with epidermal keratinocytes and dermal fibroblasts. Both cell types had better proliferation rates for the surfaces that were not etched and those that were etched for two minutes, when compared to the surfaces that were etched for one minute. The etching reduced the surface roughness by 32% and 43% for the one minute and two minutes durations, respectively. The etching increased the pore diameter by 18% and 32% for the one minute and two minutes durations, respectively, which resulted in more area for cells to migrate and attach.

To truly understand the biological response to various implant surfaces, *in vitro* results can be confirmed by an *in vivo* study. Data such as attachment strength can also be acquired once an implant is placed in the bone and under the soft tissue. This requires implantation of a device with the desired surface characteristics within the biological environment. After a specific time interval the device can be removed and tested for both ingrowth level and strength. In order to spare unnecessary euthanasia of the animals undergoing the testing, this research designed a transdermal osseointegrated implantable device and a method for device removal that will allow the animal to restore a normal life after providing this invaluable information towards research. This device has a porous coating design like the porous disc used in the *in vitro* studies in this research. The previous studies have shown that the as-processed surface of the device will likely promote bone ingrowth, while etching the skin/implant porous surface may lead to soft tissue attachments that can then be utilized in this design.

7.0 CONCLUSIONS AND FUTURE RESEARCH

This research has investigated the *in vitro* response of various human cell types in response to EBM produced Titanium alloy (Ti6Al4V) discs with various surface topographies, both solid and porous designs, and etched and non-etched surfaces. The results have shown that living cells are present on all surface types after one week in culture indicating that EBM produced Ti6Al4V is a biocompatible surface and may be an acceptable implant material. Furthermore, results have shown that hASCs show a preference for surfaces with a rough texture, while epidermal and dermal fibroblasts exhibited a higher proliferation rate on smoother surfaces. While the discs that were chemically etched had living cells present after one week in culture, it was unclear what the optimal duration of etching is for epidermal and dermal fibroblast proliferation *in vitro*.

Future work in this area should include additional studies using various etching durations and a larger sample size to determine the optimal method for surface treatment of EBM processed Ti6Al4V for epidermal and dermal fibroblast viability and proliferation. Once this optimization has been achieved through *in vitro* studies, the results can then be confirmed using the transdermal osseointegrated implantable device in a series of *in vivo* experiments. Once research has found the best surfaces for bone ingrowth and soft tissue attachment, the design and processing can be translated to the fabrication and preparation of transdermal osseointegrated implants. If the skin/implant surface of these implants can successfully induce bone ingrowth and soft tissue attachment there is great potential to restore the mobility and functionality to patients that have undergone limb removal.

REFERENCES

Alberts B, Johnson A, Lewis J, Raff M, Roberts K, & Walter P. (2008). Specialized Tissues, Stem Cells, and Tissue Renewal. (5th ed.). *Molecular Biology of the cell; Reference Edition* (pp. 1417-1426). Garland Science.

Albrektsson T, Brånemark P-I, Hansson H-A, Kasemo B, Larsson K, Lundström I, McQueen D and Skalak R. (1983). The interface zone of inorganic implants *In vivo*: Titanium implants in bone. *Annals of Biomedical Engineering, 11*(1), 1-27.

Allen DG, Riviere JE, & Monteiro-Riviere NA. (2001). Cytokine induction as a measure of cutaneous toxicity in primary and immortalized porcine keratinocytes exposed to jet fuels, and their relationship to normal human epidermal keratinocytes. *Toxicology Letters, 119*(3),209–217.

An N, Schedle A, Wieland M, Andrukhov O, Matejka M, & Rausch-Fan X. (2009). Proliferation, behavior, and cytokine gene expression of human umbilical vascular endothelial cells in response to different titanium surfaces. *Journal of Biomedical Materials Research Part A, 93A*(1), 364-172.

Anselme K, Linez P, Bigerelle M, Le Maguer D, Le Maguer A, Hardouin P, Hildebrand HF, Lost A, & Leroy JM. (2000). The relative influence of the topography and chemistry of TiAl6V4 surfaces on osteoblastic cell behaviour. *Biomaterials, 21*(15), 1567-1577.

Asaoka K, Kuwayama N, Okuno O, Miura I. (1985). Mechanical-properties and biomechanical compatibility of porous titanium for dental implants. *Journal of Biomedical Materials Research, 19*(6), 699-713.

Balla VK, DeVasConCellos PD, Xue W, Bose S, & Bandyopadhyay A. (2009). Fabrication of compositionally and structurally graded Ti–TiO2 structures using laser engineered net shaping (LENS). *Acta Biomaterialia, 5*(5), 1831–1837.

Bandyopadhyay A, Espana F, Balla VK, Bose S, Ohgami Y, Davies NM. (2010). Influence of porosity on mechanical properties and in vivo response of Ti6Al4V implants. *Acta Biomaterialia, 6*(4), 1640-1648.

Beal J, Boyer R, & Sanders D. (2006). Forming of Titanium and Titanium Alloys. *Metalworking: Sheet Forming*, *14B*, ASM Handbook, ASM International, 656–669.

Bellemans J. (1999). Osseointegration in porous coated knee arthroplasty. The influence of component coating type in sheep. *Acta Orthopaedica Scandinavica. Supplementum, 288,* 1– 35.

Bernacki SH, Wall ME, & Loboa EG. (2008). Isolation of human mesenchymal stem cells from bone and adipose tissue. *Stem Cell Culture, 86*, 257–278.

Beumer GJ, van Blitterswijk CA, Bakker D, Ponec M. (1993). Cell-seeding and in vitro biocompatibility evaluation of polymeric matrices of PEO/PBT copolymers and PLLA, *Biomaterials, 14*(8), 598-604.

Bitar M, Salih V, Mudera V, Knowles JC, Lewis MP. (2004). Soluble phosphate glasses: in vitro studies using human cells of hard and soft tissue origin, *Biomaterials, 25*(12), 2283-2292

Black J. (1992). *Biological Performance of Materials: Fundamentals of Biocompatibility.* New York: M Decker, Inc.

Black J. (1994). Biological performance of tantalum. *Clinical Materials, 16*(3), 167-173.

Blalock, T, Bai X, & Rabiei A. (2007). A study on microstructure and properties of calcium phosphate coatings processed using ion beam assisted deposition on heated substrates. *Surface and Coatings Technology, 201*(12), 5850-5858.

Bobyn JD, Poggie RA, Krygier JJ, Lewallen DG, Hanssen AD, Lewis RJ, Unger AS, O'Keefe TJ, Christie MJ, Nasser S, Wood JE, Stulberg D, & Tanzer M. (2004). Clinical validation of a structural porous tantalum biomaterial for adult reconstruction. *The Journal of Bone and Joint Surgery American, 86*, 123-129.

Bowers KT, Keller JC, Randolph BA, Wick DG, Michaels CM. (1992). Optimization of surface micromorphology for enhanced osteoblast responses in vitro. *The International Journal of Oral and Maxillofacial Implants, 7*(3), 302–310.

Boyce ST & Warden GD. (2002). Principles and practices for treatment of cutaneous wounds with cultured skin substitutes, *The American Journal of Surgery, 183*(4), 445-456.

Brånemark PI, Hansson BO, Adell R, Breine U, Lindström J, Hallén O, & Ohman A. (1977). Osseointegrated implants in the treatment of the edentulous jaw. Experience from a 10-year period. *Scandinavian Journal for Plastic and Reconstructive Surgery Supplementum, 16*, 1–132.

Brånemark R, Brånemark PI, Rydevik B, & Meyers RR. (2001). Osseointegration in skeletal reconstruction and rehabilitation: A review. *Journal of Rehabilitation Research and Development, 38*(2), 175-181.

Brunette D, Tengvall P, Textor M, & Thomsen P. (2001). *Titanium in Medicine: Material Science, Surface Science, Engineering, Biological Responses and Medical Applications*. Göteborg, Sweden: Springer.

Buser D, Schenk RK, Steinemann S, Fiorellini JP, Fox CH, and Stich H. (1991). Influence of surface characteristics on bone integration of titanium implants. A histomorphometric study in miniature pigs. *Journal of Biomedical Materials Research, 25*(7), 889-902.

Chiba J, Rubash HE, Kim KJ, and Iwaki Y. (1994). The characterization of cytokines in the interface tissue obtained from failed cementless total hip arthroplasty with and without femoral osteolysis. *Clinical Orthopaedics & Related Research*, *300*, 304-312.

Chou TGR, Petti CA, Szakacs J, & Bloebaum RD. (2010). Evaluating antimicrobials and implant materials for infection prevention around transcutaneous osseointegrated implants in a rabbit model. *Journal of Biomedical Materials Research, Part A,, 92A*(3), 942-952.

Clemow AJT, Weinstein AM, Klawitter JJ, Koeneman J, & Anderson J. (1981). Interface mechanics of porous titanium implants. *Journal of Biomedical Materials Research, 15*(1), 73-82

Cook SD, Thomas KA, Delton JE, Volkman TK, Whitecloud III TS, & Key JF. (1991). Hydroxylapatite coating of porous implants improves bone ingrowth and interface attachment strength. *Journal of Biomedical Materials Research*, *26*(8), 989-1001.

Cooper ML, Hansbrough JF, Spielvogel RL, Cohen R, Bartel RL, & Naughton G. (1991). In vivo optimization of a living dermal substitute employing cultured human fibroblasts on a biodegradable polyglycolic acid or polyglactin mesh, *Biomaterials, 12*(2), 243-248.

Cormier D, Harrysson O, and West H. (2004). Characterization of H13 Steel Produced via Electron Beam Melting. *Rapid Prototyping Journal*, *10*(1), 35-41.

Curodeau A, Sachs E, & Caldarise S. (2000). Design and fabrication of cast orthopedic implants with freeform surface textures from 3-D printed ceramic shell. *The Journal of Biomedical Materials Research, 53*(5)*,* 525–535.

Dalton JE, Cook SD, Thomas KA, Kay JF. (1995). The effects of operative fit and hydroxyapatite coating on the mechanical and biological response to porous implants. *The Journal of Bone and Joint Surgery,* 77(1), 97-110.

Daugaard H, Elmengaard B, Bechtold JE, & Soballe K. (2008). Bone growth enhancement in vivo on press-fit titanium alloy implants with acid etched microtexture. *Journal of Biomedical Materials Research, Part A, 87A*(2), 434–440.

Davis JR. (2004). *Handbook of Materials for Medical Devices*. J. R. Davis, (Ed.). Materials Park, OH: ASM International.

Deligianni DD, Katsala N, Ladas S, Sotiropoulou D, Amedee J, & Missirlis YF. (2001). Effect of surface roughness of the titanium alloy Ti–6Al–4V on human bone marrow cell response and on protein adsorption. *Biomaterials, 22*(11), 1241-1251.

Devine TM & Wulff J. (1975). Cast vs. wrought Cobalt-Chromium surgical implant alloys. *Journal of Biomedical Materials Research, 9*(2), 151-167.

El-Warrak AO, Olmstead M, Schneider R, Meinel L, Bettschart-Wolfisberger R, Akens MK, Auer J, & von Rechenberg B. (2004). An experimental animal model of aseptic loosening of hip prostheses in sheep to study early biochemical changes at the interface membrane. *BMC Musculoskeletal Disorders, 5*,7.

Engh CA, Bobyn JD, & Glassman AH. (1987). Porous-coated hip replacement. The factors governing bone ingrowth, stress shielding, and clinical results. *The Journal of Bone and Joint Surgery British, 69B*(1), 45-55.

Fuchs E & Raghavan S. (2002). Getting under the skin of epidermal morphogenesis. *Nature Reviews Genetics, 3*, 199-209.

Gauthier-fiagnon C, Grise M-C, Potvin D (1998). Predisposing factors related to prosthetic use by people with a transtibial and transfemoral amputation. *Journal of Prosthetics and Orthotics*, *10*(4), 99-109.

Gaytan SM, Murr LE, Medina F, Martinez E, Lopez MI, & Wicker RB. (2009). Advanced metal powder based manufacturing of complex components by electron beam melting. *Materials Technology: Advanced Performance Materials, 24*(3), 180–190.

Geesink RG, de Groot K, & Klein CP. (1987). Chemical implant fixation using hydroxyl-apatite coatings. The development of a human total hip prosthesis for chemical fixation to bone using hydroxyl-apatite coatings on titanium substrates. *Clinical Orthopaedics and related research, 225*, 147-170.

Goldberg VM & Jinno T. (1999). The bone–implant interface: a dynamic surface. *Journal of Long Term Eff Med Implants, 9*(1–2), 11–21.

Gordon D, Sun SN, Pendegrass C, & Blunn G. (2006). The influence of titanium alloy surface topography on keratinocyte growth and expression of adhesion complex molecules. *Journal of Bone and Joint Surgery, British, 88B*(3), 397.

Groessner-Schreiber B, Neubert A, Müller D, Hopp M, Griepentrog M, & Lange K. (2002). Fibroblast growth on surface-modified dental implants: An in vitro study. *Journal of Biomedical Materials Research Part A, (64A)*4, 591 – 599.

Größner-Schreiber B, Herzog M, Hedderich J, Dück A, Hannig M, & Griepentrog M. (2006). Focal adhesion contact formation by fibroblasts cultured on surface modified dental implants: an in vitro study. *Clinical Oral Implants Research, 17*(6), 736–745.

Hacking SA, Bobyn JD, Toh K, Tanzer M, Krygier JJ. (2000). Fibrous tissue ingrowth and attachment to porous tantalum. *Journal of Biomedical Materials Research Part A, 52*(4)*,* 631-8.

Habibovic P, Barrère F, van Blitterswijk CA, de Groot K, and Layrolle P. (2002). Biomimetic Hydroxyapatite Coating on Metal Implants**.** *J. Am. Ceram. Soc., 85* (3), 517–22.

Harrysson OLA, Cansizoglu O, Marcellin-Little DJ, Cormier DR, West HA II. (2008). Direct metal fabrication of titanium implants with tailored materials and mechanical properties using electron beam melting technology. *Materials Science & Engineering*, *28*(3), 366-373.

Hill DLG, Batchelor PG, Holden M, & Hawkes DJ. (2001). Medical image registration. *Physics in Medicine and Biology, 46*(3).

Hodde, J. (2002). Naturally occurring polymers as acellular bioscaffolds. *Tissue Engineering. 8*(2), 295-308.

Hu D & K**ovacevic** R. (2003). Sensing, modeling and control for laser-based additive manufacturing. *International Journal of Machine Tools and Manufacture, 43*(1), 51-60.

Hulbert, S.F., Young, F.A., Mathews, R.S., Klawitter, J.J., Talbert, C.D., and Stelling, F.H. (1970). Potential of ceramic materials as permanently implantable skeletal prostheses, *Journal of Biomedical Materials Research, 4*(3).

Imamura M, Hashino S, Kobayashi H, Kubayashi S, Hirano S, Minagawa T, et al. (1994). Serum cytokine levels in bone marrow transplantation: synergistic interaction of interleukin-6, interferon-gamma, and tumor necrosis factor-alpha in graft-versus-host disease. *Bone Marrow Transplantation, 13(*6), 745–751.

Inadome T, Hayashi K, Nakashima Y, Tsumura H, Sugioka Y. (1995). Comparison of bone-implant interface shear strength of hydroxyapatite-coated and alumina-coated metal implants. *Journal of Biomedical Materials Research, 29*(1), 19-24.

Janeway C. (2005). *Immunobiology: the immune system in health and disease*. (6th ed.). New York: Garland Science.

Karageorgiou V & Kaplan D. (2005). Porosity of 3D biomaterial scaffolds and osteogenesis, *Biomaterials, 26*(27), 5474-5491.

Khaing MW, Fuh JYH, & Lu L. (2001). Direct metal laser sintering for rapid tooling: processing and characterization of EOS parts. *Journal of Material Processing Technology, 113*(1-3), 269-272.

Klokkevold PR, Nishimura RD, Adachi M and CaputoA. (1997). Osseointegration enhanced by chemical etching of the titanium surface. A torque removal study in the rabbit. *Clin Oral Implants Res 8*(6), 442–447.

Kreutz EW, Backes G, Gasser A, & Wissebach K. (1995). Rapid prototyping with CO2 laser radiation. *Applied Surface Science, 86*(1), 310-316.

Krishna BV, Xue W, Bose S, Bandyopadhyay A. (2008). Functionally graded Co–Cr–Mo coating on Ti–6Al–4V alloy structures. *Acta Biomaterialia, 4*(3), 697–706.

Krishna BV, Bose S, Bandyopadhyay A. (2009). Fabrication of porous NiTi shape memory alloy structures using laser engineered net shaping. *Journal of Biomedical Materials Research Part B. Applied Biomaterials, 89B*(2), 481–490.

Kruth JP, Wang X, Laoui T, & Froyen L. (2003). Lasers and materials in selective laser sintering. *Assembly Automation, 23*, 357-371.

Kuboki Y, Takita H, Kobayashi D, Tsuruga E, Inoue M, & Murata M. (1998). BMP-induced osteogenesis on the surface of hydroxyapatite with geometrically feasible and nonfeasible structures: topology of osteogenesis. *Journal of Biomedical Materials Research, 39*(2), 190-199.

Kunzler TP, Drobek T, Schuler M, & Spencer ND. (2007). Systematic study of osteoblast and fibroblast response to roughness by means of surface-morphology gradients. *Biomaterials, 28*(13), 2175-2182.

Kurtz S, Ong K, Lau E, Mowat F, & Halpern M. (2007). Projections of Primary and Revision Hip and Knee Arthroplasty in the United States from 2005 to 2030. *Journal of Bone and Joint Surgery America, 89*, 780-785.

Kusakabe H, Sakamaki T, Nihei K, Oyama Y, Yanagimoto S, Ichimiya M, Kimura J, & Toyama Y. (2004). Osseointegration of a hydroxyapatite-coated multilayered mesh stem, *Biomaterials, 25*(15), 2957–2969.

Könönen M, Hormia M, Kivilahti J, Hautaniemi J, Thesleff I. (1992). Effect of surface processing on the attachment, orientation, and proliferation of human gingival fibroblasts on titanium. *Journal of Biomedical Materials Research, 26*(10), 1325 – 1341.

Levine BR, Sporer S, Poggie RA, Della Valle CJ, Jacobs JJ. (2006). Experimental and clinical performance of porous tantalum in orthopedic surgery. *Biomaterials, 27*(27), 4671–4681.

Lewis G. (1997). Properties of acrylic bone cement: state of the art review. *Journal of Biomedical Materials Research, 38*(2), 155–182.

Li JP, de Wijn JR, Van Blitterswijk CA, & de Groot K. (2006). Porous Ti6Al4V scaffold directly fabricating by rapid prototyping: preparation and in vitro experiment, *Biomaterials, 27*(8), 1223-1235.

Li X, Wang CT, Zhang WG, & Li YC. (2009). Properties of a porous Ti–6Al–4V implant with a low stiffness for biomedical application. *Proceedings of the Institution of Mechanical Engineers, Part H: Journal of Engineering in Medicine, 223*(2), 173–178.

Lopez-Heredia MA, Goyenvalle E, Aguado E, Pilet P, Leroux C, Dorget M, Weiss P, & Layrolle P. (2008). Bone growth in rapid prototyped porous titanium implants. *Journal of Biomedical Materials Research, Part A, 85A*(3), 664–673.

Marcellin-Little DJ, Harrysson OL, Cansizoglu O. (2008). In vitro evaluation of a custom cutting jig and custom plate for canine tibial plateau leveling. *American Journal of Veterinary Research, 69*(7), 961–966.

Martin JY, Schwartz Z, Hummert TW, Schraub DM, Simpson J, Lankford Jr. J, Dean DD, Cochran DL, & Boyan BD. (1995). Effect of titanium surface roughness on proliferation, differentiation, and protein synthesis of human osteoblast-like cells (MG63). *Journal of Biomedical Materials Research, 29*(3), 389-401

McCullen SD, Stevens DR, Roberts WA, Clarke LI, Bernacki SH, Gorga RE, & Loboa EG. (2007). Characterization of electrospun nanocomposite scaffolds and biocompatibility with adipose-derived human mesenchymal stem cells. *International Journal of Nanomedicine, 2*(2), 253–263.

Melican MC, Zimmerman MC, Dhillon MS, Ponnambalam AR, Curodeau A, & Parsons JR. (2001). Three-dimensional printing and porous metallic surfaces: a new orthopedic application. *Journal of Biomedical Materials Research, 55*(2), 194-202.

Meredith DO, Eschbach L, Riehle MO, Curtis ASG, Richards RG. (2007). Microtopography of Metal Surfaces Influence Fibroblast Growth by Modifying Cell Shape, Cytoskeleton, and Adhesion. *Journal of Orthopaedic Research, 25*(11), 1523 – 1533.

Meulenbelt HEJ, Geertzen JHB, Dijkstra P, & Jonkman M. (2006). Skin problems in lower limb amputees: A systematic review. *Disability & Rehabilitation, 28*(10), 603-608.

Min CK, Lee WY, Min DJ, Lee DG, Kim YJ, Park YH, et al. (2001). The kinetics of circulating cytokines including IL-6, TNF-alpha, IL-8 and IL-10 following allogeneic hematopoietic stem cell transplantation. *Bone Marrow Transplantation, 28*(10), 935–40.

Morrison C, Macnair R, MacDonald C, Wykman A, Goldie I, & Grant MH. (1995). In vitro biocompatibility testing of polymers for orthopaedic implants using cultured fibroblasts and osteoblasts, *Biomaterials, 16*(13), 987-992.

Murr LE, Quinones SA, Gaytan SM, Lopez MI, Rodela A, Martinez EY, et al. (2009). Microstructure and mechanical behavior of Ti–6Al–4V produced by rapidlayer manufacturing, for biomedical applications. *Journal of the Mechanical Behaviors of Biomedical Materials, 2*(1), 20–32.

Nakashima Y, Hayashi K, Inadome T, Uenoyama K, Hara T, Kanemaru T, Sugioka Y, & Noda I. (1997). Hydroxyapatite-coating on titanium arc sprayed titanium implants. *Journal of Biomedical Materials Research Part A, 35*(3), 287 – 298.

Nakayama GR, Caton MC, Nova MP, Parandoosh Z. (1997). Assessment of the Alamar Blue assay for cellular growth and viability in vitro. *Journal of Immunological Methods, 204*(2), 205–208.

Nicholson JW. (2002). *The Chemistry of Medical and Dental Materials*. JA Connor (ed.). Cambridge, UK: Royal Society of Chemistry.

Nishiguchi S, Kato H, Neo M, Oka M, Kim HM, Kokubo T, & Nakamura T. (2001). Alkali- and heat-treated porous titanium for orthopedic implants. *Journal of Biomedical Materials Research, 54*(2), 198–208.

Okumura A, Goto M, Goto T, Yoshinari M, Masuko S, Katsuki T, & Tanaka T. (2001). Substrate affects the initial attachment and subsequent behavior of human osteoblastic cells (Saos-2). *Biomaterials, 22*(16), 2263-2271.

Oonishi H, Yamamoto M, Ishimaru H, Tsuji E, Kushitani S, Aono M, & Ukon Y. (1989). The effect of hydroxyapatite coating on bone growth into porous titanium alloy implants. *Journal of Bone and Joint Surgery, British, 71*, 213–216.

Oshida Y. (2007). *Bioscience and Bioengineering of Titanium Materials*. Great Britain: Elsevier.

Pendegrass CJ, Goodship AE, & Blunn GW. (2006). Development of a soft tissue seal around bone-anchored transcutaneous amputation prostheses. *Biomaterials, 27*(23), 4183-4191.

Pendegrass CJ, Goodship AE, Price JS, & Blunn GW. (2006). Nature's answer to breaching the skin barrier: an innovative development for amputees. *Journal of Anatomy, 209*(1), 59-67.

Pendegrass CJ, Gordon D, Middleton CA, Sun SN, & Blunn GW. (2008). Sealing the skin barrier around transcutaneous implants: in vitro study of keratinocyte proliferation and adhesion in response to surface modifications of titanium alloy. *Journal of Bone and Joint Surgery British, 90B*(1), 114 - 121.

Pendegrass CJ, Middleton CA, Gordon D, Jacob J, & Blunn GW. (2008). Measuring the strength of dermal fibroblast attachment to functionalized titanium alloys in vitro. *Journal of Biomedical Materials Research Part A, 92A*(3), 1028-1037.

Pitkin M, Raykhtsaum G, Galibin OV, Protasov MV, Chihovskaya JV, & Belyaeva IG. (2006). Skin and bone integrated prosthetic pylon: a pilot animal study. *Journal of Rehabilitation Research and Development, 43*(4), 573-580.

Ponader S, Vairaktaris E, Heinl P, Wilmowsky CV, Rottmair A, Körner C, et al. (2008). Effects of topographical surface modifications of electron beam melted Ti–6Al–4V titanium on human fetal osteoblasts. *Journal of Biomedical Materials Research, Part A, 84A*(4), 1111–1119.

Ponsonnet L, Reybier K, Jaffrezic N, Comte V, Lagneau C, Lissac M, & Martelet C. (2003). Relationship between surface properties (roughness, wettability) of titanium and titanium alloys and cell behaviour, *Materials Science and Engineering: C, 23*(4), 551-560.

Prasertsung I, Kanokpanont S, Bunaprasert T, Thanakit V, & Damrongsakkul S. (2008). Development of acellular dermis from porcine skin using periodic pressurized technique. *Journal of Biomedical Materials Research Part B: Applied Biomaterials, 85B*(1), 210-219.

Puck TT, Cieciura SJ, & Fisher HW. (1957). Clonal growth in vitro of human cells with fibroblastic morphology: comparison of growth and genetic characteristics of single epithelioid and fibroblast-like cells from a variety of human organs. *Journal of Experimental Medicine, 106*(1), 145-158.

Puleo DA & Nanci A. (1999). Understanding and controlling the bone-implant interface. *Biomaterials, 20*(23-24), 2311-2321.

Richards RG. (1996). The effect of surface roughness on fibroblast adhesion in vitro. *Injury, 27*(3), S.

Rivero DP, Fox J. Skipor AK, Urban RM, & Galante JO. (1988). Calcium phosphate-coated porous titanium implants for enhanced skeletal fixation. *Journal of Biomedical Materials Research, 22*(3), 191-201.

Rompen E, Domken O, Degidi M, Pontes AEF, Piattelli A. (2006). The effect of material characteristics, of surface topography and of implant components and connections on soft tissue integration: a literature review. *Clinical Oral Implants Research, 17*(2), 55–67.

Roy M, Vamsi Krishna B, Bandyopadhyay A, & Bose S. (2008). Laser processing of bioactive tricalcium phosphate coating on titanium for load-bearing implants. *Acta Biomaterialia, 4*(2), 324–333.

Ryan G, Pandit A, & Apatsidis DP. (2006). Fabrication methods of porous metals for use in orthopaedic applications. *Biomaterials, 27*(13), 2651-2670.

Saha S & Pal S. (1984). Mechanical-properties of bone-cement—a review. *Journal of Biomedical Materials Research, 18*(4), 435–462.

Sammons RL, Lumbikanonda N, Gross M, & Cantzler P. (2005). Comparison of osteoblast spreading on microstructured dental implant surfaces and cell behaviour in an explant model of osseointegration. A scanning electron microscopic study. *Clinical Oral Implants Research, 16*(6), 657–666.

Say WC & Tsai YY. (2004). Surface characterization of cast Ti-6Al-4V in hydrofluoric-nitric pickling solutions. *Surface and Coatings Technology, 176*(3), 337-343.

Schneider LA, Dissemond J, Brenneisen P, Hainzl A, Briviba K, Wlaschek M, & Scharffetter-Kochanek K. (2006). Adaptive cellular protection against UVA-1-induced lipid peroxidation in human dermal fibroblasts shows donor-to-donor variability and is glutathione dependent. *Archives of Dermatological Research, 297*(7), 324-328.

Schwaighofer H, Herold M, Schwarz T, Nordberg J, Ceska M, Prior C, et al. (1994). Serum levels of interleukin-6, interleukin-8, and C-reactive protein after human allogeneic bone-marrow transplantation. *Transplantation, 58*(4), 430–436.

Seo YK, Song KY, Kim YJ, & Park JK. (2007). Wound Healing Effect of Acellular Artificial Dermis Containing Extracellular Matrix Secreted by Human Skin Fibroblasts. *Artificial Organs, 31*(7), 509-520.

Shim J, Nakamura H, Ogawa T, & Gupta V. (2009). An understanding of the mechanism that promotes adhesion between roughened titanium implants and mineralized tissue. *Journal of Biomechanical Engineering, 131*(5), 054503.

Shirkhanzadeh M. (1991). Bioactive calcium phosphate coatings prepared by electrodeposition. *Journal of Materials Science Letters, 10*(23), 1415-1417.

Simmons CA, Valiquette N, & Pilliar RM. (1999). Osseointegration of sintered porous-surfaced and plasma spray-coated implants: An animal model study of early postimplantation healing response and mechanical stability. *Journal of Biomedical Materials Research Part A, 47*(2), 127-138.

Søballe K, Hansen ES, Brockstedt-Rasmussen H, Pedersen CM, & Bünger C. (1990). Hydroxyapatite coating enhances fixation of porous coated implants: A comparison in dogs between press fit and noninterference fit. *Acta Orthopaedica, 61*(4), 299-306.

Sotereanos N, Sewecke J, Raukar GJ, DeMeo PJ, Bargiotas K, & Wohlrab D. (2006). Revision total hip arthroplasty with a custom cementless stem with distal cross-locking screws. Early results in femora with large proximal segmental deficiencies. *The Journal of Bone and Joint Surgery American, 88*, 1079–1084.

Stea S, Visentin M, Granchi D, Ciapetti G, Donati ME, Sudanese A, et al. (2000). Cytokines and osteolysis around total hip prostheses. *Cytokine, 12*(10), 1575–1579.

Stephenson PK, Freeman MAR, Recell PA, Germain J, Tuke M, and Pirie CJ. (1991). The effect of hydroxyapatite coating on ingrowth of bone into cavities in an implant. *The Journal of Arthroplasty*, *6*(1), 51-58.

Story BJ, Wagner WR, Gaisser DM, Cook SD, & Rust-Dawicki AM. (1998). In vivo performance of a modified CSTi dental implant coating. *International Journal of Oral Maxillofacial Implants, 13*(6), 749–757.

Sumner DR, Turner TM, & Urban RM. (2001). Animal models relevant to cementless joint replacement. *Journal of Musculoskeletal and Neuronal Interactions, 1*(4), 333–345.

Szmukler-Moncler S & Brunski JB. (1988). *The influence of force, motion and relatedquantities on the response of bone to implants*. In: Fitzgerald AF, editor. Noncemented total hip arthroplasty. New York: Raven.

Taminger KM & Hafley RA. (2006). Electron beam freeform fabrication for cost effective near-net shape manufacturing. *NATO/RTOAVT-139 Specialists' Meeting on Cost Effective Manufacture via Net Shape Processing (Amsterdam,the Netherlands, 2006) (NATO)*, 9–25.

Thelen S, Barthelat F, & Brinson LC. (2004). Mechanics considerations for microporous titanium as an orthopedic implant material. *Journal of Biomedical Materials Research Part A, 69*A(4), 601-610.

Thomas KA, Kay JF, Cook SD, & Jarcho M. (1987). The effect of surface macrotexture and hydroxylapatite coating on the mechanical strengths and histologic profiles of titanium implant materials. *Journal of Biomedical Materials Research, 21*(12), 1395-1414.

Thomsen P, Malmstrom J, Emanuelsson L, & René M. (2009). Electron beam-melted, free-form-fabricated titanium alloy implants: material surface characterization and early bone response in rabbits. *Journal of Biomedical Materials Research, Part B: Applied Biomaterials, 90B*(1), 35–44.

Tillander J, Hagberg K, Hagberg L, & Brånemark R. (2010). Osseointegrated titanium implants for limb prostheses attachments: Infectious complications. *Clinical Orthopaedics and Related Research*, [Epub ahead of print].

Tonello C, Zavan B, Cortivo R, Brun P, Panfilo S, & Abatangelo G. (2003). In vitro reconstruction of human dermal equivalent enriched with endothelial cells, *Biomaterials, 24*(7), 1205-1211.

Turner CH, Wang T, & Burr DB. (2001). Shear strength and fatigue properties of human cortical bone determined from pure shear tests. *Calcified Tissue International, 69*(6), 373–378.

Van Noort R. (1987). Titanium: the implant material of today. *Journal of Materials Science, 22*(11), 3801–3811.

von Recum AF. (1984). Applications and failure modes of percutaneous devices: a review. *Journal of Biomedical Materials Research, 18*(4), 323-336.

Wall ME, Bernacki SH, & Loboa EG. (2007). Effects of serial passaging on the adipogenic and osteogenic differentiation potential of adipose-derived human mesenchymal stem cells. *Tissue Engineering, 13*(6), 1291–1298.

Wall ME, Rachlin A, Otey CA, & Loboa EG. (2007). Human adipose-derived adult stem cells upregulate palladin during osteogenesis and in response to cyclic tensile strain. *American Journal of Physiology: Cell Physiology, 293*, C1532–C1538.

Weast RC, Bronsino JD. (2nd Ed.). (2000). *The Biomedical Engineering Handbook* (Vol 1). Boca Raton, FL: CRC Press.

Williams DL, Bloebaum RD, Beck JP, & Petti CA. (2010). Characterization of Bacterial Isolates Collected from a Sheep Model of Osseointegration. *Current Microbiology*. [Epub ahead of print].

Xiao Y, Riesle J, & Van Blitterswijk CA. (1999). Static and dynamic fibroblast seeding and cultivation in porous PEO/PBT scaffolds. *Journal of Materials Science: Materials in Medicine, 10*(12), 773-777.

Xie C, Reynolds D, Awad H, Rubery PT, Pelled G, Gazit D, Guldberg RE, Schwarz EM, O'Keefe RJ, Zhang X. (2007). Structural Bone Allograft Combined with Genetically Engineered Mesenchymal Stem Cells As a Novel Platform for Bone Tissue Engineering. *Tissue Engineering, 13*(3), 435-445.

Xue W, Krishna BV, Bandyopadhyay A, & Bose S. (2007). Processing and biocompatibility evaluation of laser processed porous titanium. *Acta Biomaterialia, 3*(6), 1007–1018.

Yuan H, Kurashina K, de Bruijn JD, Li Y, de Groot K, & Zhang X. (1999). A preliminary study on osteoinduction of two kinds of calcium phosphate ceramics. *Biomaterials, 20*(19), 1799–1806.

Zhao G, Raines AL, Wieland M, Schwartz Z, & Boyan BD. (2007). Requirement for both micron- and submicron scale structure for synergistic responses of osteoblasts to substrate surface energy and topography. *Biomaterials, 28*(18), 2821–2829.

Ziegler-Graham K, MacKenzie EJ, Ephraim PL, Travison TG, & Brookmeyer R. (2008). Estimating the Prevalence of Limb Loss in the United States: 2005 to 2050. *Archives of Physical Medicine and Rehabilitation, 89*(3), 422-429.